

# Studying X-ray variability of black holes with excess variance spectra

Master's Thesis in Physics

Presented by

Lucia Härer

August 23, 2021

Astronomisches Institut Dr. Karl Remeis-Sternwarte  
Friedrich-Alexander-Universität Erlangen-Nürnberg



Supervisor: Prof. Dr. Jörn Wilms



# Abstract

The strongest X-ray sources in the Universe are powered by accretion onto compact objects. These X-rays can be used to probe outflows in such systems by measuring their X-ray absorption. Outflows regulate the supply of infalling material and impact the evolution of objects through feedback processes. Accreting systems often show variability, due to the complexity of their dynamics and inhomogeneities in the accretion flow. This variability can be used to map outflow geometry and structure, especially when combined with spectroscopic information that allows the measurement of environmental characteristics, such as densities, ionisations, and element abundances. Excess variance spectroscopy is a technique that quantifies variability as a function of energy, incorporating both spectral and timing information. In this thesis, I employ excess variance spectroscopy to study outflows in two very distinct astronomical settings: the ultra-fast outflow of the luminous ( $L_{\text{bol}} \sim 10^{47} \text{erg s}^{-1}$ ) low-redshift ( $z = 0.184$ ) active galactic nucleus (AGN) PDS 456 in Ch. 3 and the strong, clumpy stellar wind in the high-mass X-ray binary (HMXB) Cyg X-1 in Ch. 4.

In Ch. 3, I present improvements to an excess variance model for ultra-fast outflows, which are fast, wide-angle accretion disc winds of AGN. The model is able to account well for the broadening of the spike-like features of these outflows in the excess variance spectrum of PDS 456, by considering two effects: a correlation between the outflow velocity and the logarithmic X-ray flux, and intrinsic Doppler broadening caused by a gas movement with  $v_{\text{int}} = 10^4 \text{ km s}^{-1}$ . The models were generated from simulated spectra by employing a Monte Carlo ansatz. I find evidence that the outflow in PDS 456 has two components, which move at  $0.27\text{--}0.30 c$  and  $0.41\text{--}0.49 c$ , and possibly a third component with  $0.15\text{--}0.20 c$ . These values agree well with the literature. I discuss the prospects of fitting AGN excess variance spectra for detecting ultra-fast outflows and investigating their structure. I provide an estimate for the strength of the correlation between the outflow velocity and the logarithmic X-ray flux and compare it to the literature.

Chapter 4 concerns stellar winds of massive stars. These winds are known to be driven by line absorption of UV photons, a mechanism prone to instabilities, causing these winds to be clumpy. Characterising the wind structure is highly relevant for understanding accretion in HMXB systems and the evolution of massive stars, as it requires accurate mass-loss estimates. In HMXBs, the X-ray source can be used as a backlight to study the variable absorption the wind structure induces. I study the soft ( $2\text{--}14\text{\AA}$ ) X-ray variability of Cyg X-1 in the low/hard spectral state with excess variance spectroscopy, using high-resolution *Chandra* gratings data. I account for various systematic effects and investigate the frequency dependence by adjusting the time binning. A key result is the strong orbital phase dependence of the excess variance, which is consistent with column density variations predicted by a simple model for a clumpy wind. I match spikes of

increased variability to spectral features identified by previous spectroscopic analyses of the same data set, most notably from silicon. In the silicon line region, the variability power is redistributed towards lower frequencies, hinting at increased line variability in large clumps. In prospect of the microcalorimetry missions that are scheduled to launch within the next decade, excess variance spectra present a promising approach to constrain the wind structure, especially if accompanied by models that consider changing ionisation.

# Zusammenfassung

Die stärksten Röntgenquellen im Universum erhalten ihre Energie aus der Akkretion von Materie auf kompakte Objekte. Durch Messung der Röntgenabsorption können Materieströme in Systemen untersucht werden, die kompakte Objekte enthalten. Ausströmende Materie reguliert die Zufuhr von einfallendem Material und beeinflusst die Entwicklung von akkretierenden Systemen durch Rückkopplungsprozesse. Akkretierende Systeme weisen aufgrund ihrer komplexen Dynamik und der Inhomogenität der Akkretionsströme häufig eine variable Leuchtkraft auf. Diese Variabilität kann genutzt werden, um die Geometrie und Struktur der ausströmenden Materie zu charakterisieren, insbesondere in Kombination mit spektroskopischen Messungen. Überschuss-Varianz-Spektroskopie ist eine Methode, die es ermöglicht, die Variabilität als Funktion der Energie quantitativ zu untersuchen, da sie sowohl Spektral- als auch Zeitinformationen enthält. In dieser Arbeit verwende ich Überschuss-Varianz-Spektroskopie, um ausfließende Materieströme in zwei sehr unterschiedlichen Szenarien zu untersuchen: den ultra-schnellen Materieausfluss des leuchtstarken ( $L_{\text{bol}} \sim 10^{47} \text{ erg s}^{-1}$ ), schwach rotverschobenen ( $z = 0.184$ ) aktiven Galaxienkerns (AGN) PDS 456 in Kapitel 3 und den starken, klumpigen Sternwind im massereichen Röntgendoppelstern Cyg X-1 in Kapitel 4.

In Kapitel 3 präsentiere ich Verbesserungen an einem Überschuss-Varianz-Modell für ultra-schnelle Materieausflüsse. Ultra-schnelle Materieausflüsse sind relativistische Winde von AGN Akkretionsscheiben, die sich durch einen großen Öffnungswinkel auszeichnen. Das Modell ist in der Lage, die Verbreiterung der spitzenartigen Merkmale (Spikes) dieser Materieausflüsse im Überschuss-Varianz-Spektrum von PDS 456 gut zu beschreiben, indem es zwei Effekte berücksichtigt: eine Korrelation zwischen der Ausflussgeschwindigkeit und dem logarithmischen Röntgenfluss, und die Dopplerverbreiterung der Spektrallinien, welche durch eine Bewegung des Gases mit  $v_{\text{int}} = 10^4 \text{ km s}^{-1}$  hervorgerufen wird. Die Modelle wurden mit Hilfe eines Monte-Carlo Ansatzes aus simulierten Spektren generiert. Die Ergebnisse legen nahe, dass der Materieausfluss in PDS 456 zwei Komponenten mit Ausflussgeschwindigkeiten von  $0.27\text{--}0.30 c$  und  $0.41\text{--}0.49 c$  aufweist, und möglicherweise eine dritte Komponente mit einer Geschwindigkeit von  $0.15\text{--}0.20 c$  vorhanden ist. Die aus dem Modell bestimmten Geschwindigkeiten stimmen gut mit der Literatur überein. Ich diskutiere die Bedeutung derartiger Modelle für Überschuss-Varianz-Spektren von AGN für die Detektion und Untersuchung ultra-schneller Materieausflüsse. Zudem schätze ich die Stärke der Korrelation zwischen der Ausflussgeschwindigkeit und dem logarithmischen Röntgenfluss ab und diskutiere ihre Übereinstimmung mit der Literatur.

Kapitel 4 betrifft Sternwinde massereicher Sterne. Es ist bekannt, dass diese Winde durch Linienabsorption von UV-Photonen angetrieben werden; ein Mechanismus, der zu Instabilität neigt, was dazu führt, dass diese Winde inhomogen sind und Materieklumpen mit erhöhter Dichte aufweisen. Die Charakterisierung der Windstruktur ist für das

Verständnis der Akkretion in Röntgendoppelsternen und die Entwicklung massereicher Sterne von großer Bedeutung, da dafür genaue Abschätzungen der Massenausflussrate des Windes nötig sind. In massereichen Röntgendoppelsternen kann die Röntgenquelle verwendet werden, um den Wind zu durchleuchten und so die variable Absorption zu untersuchen, die durch die Windstruktur hervorgerufen wird. Ich untersuche die weiche (2–14Å) Röntgen-Variabilität von Cyg X-1 im niedrigen/harten Spektralzustand mit Überschuss-Varianz-Spektroskopie unter Verwendung hochauflösender *Chandra*-Spektren. Ich berücksichtige verschiedene systematische Effekte und untersuche die Frequenzabhängigkeit durch Anpassen des Zeitschritts der Lichtkurve. Ein wichtiges Ergebnis ist die starke Abhängigkeit der Überschuss-Varianz von der orbitalen Phase, die mit Vorhersagen eines einfachen Modells eines strukturierten Windes übereinstimmt. Ich vergleiche die Positionen von Spikes und spektraler Merkmale, die in früheren spektroskopischen Analysen desselben Datensatzes identifiziert wurden. Insbesondere für Silizium kann eine klare Übereinstimmung festgestellt werden. Ein weiteres Ergebnis ist, dass die Variabilität der Siliziumlinien mehr niedrige Frequenzen aufweist als eine linienfreie Vergleichsregion. Dies deutet darauf hin, dass große Materiekumpen stärker zur Variabilität der Spektrallinien beitragen. Ich halte fest, dass Modellierungsansätze stark von einem detaillierten Verständnis der Windionisation profitieren können. Insgesamt ist Überschuss-Varianz-Spektroskopie ein vielversprechender Ansatz, um die Windstruktur zu untersuchen, insbesondere, da im Laufe der nächsten 10 Jahre Mikrokalorimetrie-Missionen starten werden, die die Sensitivität der Messungen weiter erhöhen ohne an spektraler Auflösung zu verlieren.

# Contents

<b>Abstract</b>	<b>iii</b>
<b>Zusammenfassung</b>	<b>v</b>
<b>1 Introduction</b>	<b>1</b>
1.1 Accretion onto black holes . . . . .	2
1.2 Objects powered by accreting black holes . . . . .	3
1.2.1 Active galactic nuclei . . . . .	3
1.2.2 Black hole X-ray binaries . . . . .	7
1.3 Outflows . . . . .	9
<b>2 Methods and Instrumentation</b>	<b>11</b>
2.1 Instrumentation . . . . .	11
2.1.1 Measuring X-ray photon energies . . . . .	11
2.1.2 X-ray satellites . . . . .	12
2.2 X-ray spectroscopy . . . . .	15
2.2.1 Basics and nomenclature . . . . .	15
2.2.2 Relevant concepts . . . . .	16
2.2.3 Spectral fitting . . . . .	17
2.3 X-ray variability . . . . .	18
2.4 Excess variance spectroscopy . . . . .	18
<b>3 Part I: modelling the ultra-fast outflow of the quasar PDS 456</b>	<b>21</b>
3.1 Ultra-fast outflows . . . . .	21
3.2 The high-energy low-redshift quasar PDS 456 . . . . .	22
3.3 Detecting UFOs with excess variance spectroscopy . . . . .	24
3.4 Modelling excess variance spectra . . . . .	25
3.4.1 The Monte Carlo modelling ansatz . . . . .	25
3.4.2 Improving upon the UFO model . . . . .	26
3.5 Fitting the excess variance spectrum of PDS 456 . . . . .	28
3.5.1 Fitting spectra of PDS 456 . . . . .	29
3.5.2 Revisiting IRAS 13224–3809 . . . . .	32
3.6 Discussion . . . . .	34
3.6.1 The multi-layered structure of the UFO . . . . .	34
3.6.2 Determining the cause of the spike broadening . . . . .	37
3.7 Summary . . . . .	37

<b>4</b>	<b>Part II: stellar wind variability in Cyg X-1 at high spectral resolution</b>	<b>39</b>
4.1	Probing stellar winds of supermassive stars . . . . .	39
4.2	The stellar wind in Cygnus X-1 . . . . .	40
4.3	Observations and Methods . . . . .	42
4.3.1	Chandra HETG observations of Cyg X-1 . . . . .	42
4.3.2	Generation of the excess variance spectra . . . . .	42
4.4	Eliminating systematic variability . . . . .	43
4.4.1	Read-out time and effective area differences of the gratings . . . . .	43
4.4.2	Filtering CCD gaps and dead pixel rows . . . . .	45
4.4.3	Estimating binning variability . . . . .	46
4.5	Results . . . . .	48
4.5.1	Overview: $F_{\text{var}}^2$ continuum and spike features . . . . .	48
4.5.2	Silicon and sulphur line regions at superior conjunction . . . . .	52
4.5.3	Frequency dependence at superior conjunction . . . . .	52
4.6	Discussion . . . . .	54
4.6.1	Absorption driven variability . . . . .	54
4.6.2	Modelling the orbital phase dependent variability of a clumpy stellar wind . . . . .	56
4.6.3	Line of sight dependence of the variability continuum . . . . .	58
4.6.4	Suppressed line variability at inferior conjunction . . . . .	59
4.6.5	Clump mass and radius . . . . .	60
4.6.6	Ionisation . . . . .	61
4.7	Summary . . . . .	62
<b>5</b>	<b>Conclusions</b>	<b>65</b>
	<b>Acknowledgments</b>	<b>67</b>
	<b>Bibliography</b>	<b>69</b>
	<b>Eigenständigkeitserklärung</b>	<b>75</b>

# 1 Introduction

Black holes give rise to a plethora of highly energetic phenomena in the universe. The study of these phenomena sheds light on the complex environments black holes reside in and enables tests of general relativity. In this way, black holes provide a multitude of prospects to shift the boundary of known physics. To provide the reader with a foundation for the research conducted in this Master's thesis, I first introduce basic properties of black holes before discussing their associated high energy phenomena in Sect. 1.1 and the following. I mainly follow *High energy astrophysics, Volume 2* by Longair (1994), *Exploring the X-ray Universe* by Seward & Charles (2010), and *Active Galactic Nuclei* by Beckmann & Shrader (2012).

Black holes have long been only a theoretical construct, predicted by general relativity. The notion of a *dark star*, with such a strong gravity that not even light can escape it, existed even earlier, having been first suggested by John Michell and Pierre-Simon Laplace in the late 18th century (see Montgomery et al. 2009). Black holes are characterised by very few basic quantities: mass, charge, and angular momentum (see Longair 1994, Ch. 16). The mass,  $M$ , determines the Schwarzschild radius<sup>1</sup>,

$$r_g = \frac{2GM}{c^2}. \quad (1.1)$$

Below  $r_g$ , a velocity greater than the speed of light,  $c$ , would be required to escape the gravitational potential. As a consequence, no information reaches the observer from inside the black hole. This is the defining property of black holes, which differentiates them from normal objects, such as stars and planets. Due to the strong gravity, a black hole also has an innermost stable circular orbit (Longair 1994, Ch. 16),

$$r_{\text{isco}} = 3r_g = 3M M_{\odot}^{-1} \text{ km}, \quad (1.2)$$

where  $M_{\odot}$  is the mass of the sun. Each particle on an orbit with  $r < r_{\text{isco}}$  inevitably falls into the black hole, as general relativity predicts that such orbits have to be unstable (see Longair 1994, Ch. 16). It is important to note that the Eq. 1.1 and 1.2 apply to the case of a non-rotating black hole (Schwarzschild black hole) and change for rotating, so-called Kerr black holes (Longair 1994, Ch. 16).

By their nature, black holes emit no light themselves and can therefore only be identified indirectly. But even though the properties of black holes are simple, their environments are not. In the strong gravitational field, matter can release enormous amounts of highly energetic radiation while falling (“accreting”) onto the black hole. This radiation, which

---

<sup>1</sup>This definition follows Longair (1994). In recent years, the gravitational radius  $r_{\text{grav}} = 0.5r_g$  has become more and more widely adopted.

reaches X-ray energies, can be used to find black holes and probe the complex flows around them. Objects harbouring black holes and phenomena associated with their complex environments are the topic of the remainder of this introduction.

## 1.1 Accretion onto black holes

Accretion is the process by which matter falls onto an object due to the gravitational force. The energy gained by a mass,  $m$ , falling from an initial radius,  $r$ , down to  $R$  is

$$\Delta E_{\text{pot}} = GMm \left( \frac{1}{r} - \frac{1}{R} \right), \quad (1.3)$$

where  $M$  is the mass of the accreting object.  $\Delta E_{\text{pot}}$  is converted into kinetic energy as the matter flow accelerates in the gravitational potential. The fall from  $r$  down to  $R$  is trivial for a test particle at rest. The case with angular momentum is more complicated, as the particle orbits the black hole and decaying the orbit requires the release of angular momentum. Therefore, the test particle cannot accrete on its own. An interacting matter flow, however, will form an accretion disc. The disc enables accretion by transporting angular momentum outwards and dissipating the kinetic energy gained by the accreting material in the form of heat. Angular momentum transport and heat dissipation are possible because accretions discs are viscous and experience internal shear stress, as the angular velocity is not constant with radius for Keplerian motion. The viscosity arises from highly turbulent flows within the disc, the origin of which is under debate (see Frank et al. 2002, Ch. 5). Note that the accretion geometry can be modified in special cases, e.g., for small angular momenta or in strong magnetic fields.

For continuous infall from infinity ( $r \rightarrow \infty$ ), Eq. 1.3 becomes the power released during the accretion process,

$$L = \frac{GM\dot{m}}{R} = \frac{1}{2}\dot{m}c^2 \left( \frac{r_g}{R} \right). \quad (1.4)$$

The rate of infalling mass,  $\dot{m}$ , is called the accretion rate. The right-hand side expresses  $R$  relative to the Schwarzschild radius,  $r_g$ , from Eq. 1.1, which gives the equation the form  $L = \eta\dot{m}c^2$ , with an efficiency,  $\eta$ . A value of  $\eta = 1$  would mean that the released power is equivalent to the rest-mass energy of the accreting matter. The efficiency in Eq. 1.4 is determined by the so-called compactness of the object,  $Rr_g^{-1}$ . For black holes,  $R$  is given by  $r_{\text{isco}}$ , as an infall into the black hole is inevitable below that radius. Black holes possess  $\eta = 0.06\text{--}0.426$ , depending on their angular momentum (Longair 1994, Ch. 16). For comparison, fusion only reaches  $\eta \lesssim 7 \cdot 10^{-3}$  (Longair 1994, Ch. 16). Accretion onto compact objects is therefore exceptionally efficient at converting energy into radiation. In the light of this result, it is not surprising that radiation from accreting supermassive black holes in active galaxies can outshine their starlight by orders of magnitude.

The radiation that is produced during the accretion exerts a radiative force on the infalling material, by transferring energy onto it through scattering. The radiative force counteracts the gravitational attraction and can therefore self-regulate the accretion process if it is of comparable magnitude. In the simplest case, the accreting material is a

gas of protons and electrons, where the proton mass,  $m_p$ , dominates the gravitational attraction and Compton scattering, i.e., scattering on unbound electrons, dominates the radiative force. The boundary case where the radiative force is large enough to hold off the accreting material is called the Eddington luminosity (Longair 1994, Ch. 16),

$$L_{\text{edd}} = \frac{4\pi GMm_p c}{\sigma}, \quad (1.5)$$

where  $\sigma$  is the Compton scattering cross section. Accreting systems can exceed  $L_{\text{edd}}$ , which is called super-Eddington accretion, due to multiple factors: Eq. 1.5 ignores the disc geometry and assumes spherical accretion. In addition, the gravitational force increases if more massive nuclei are part of the accretion flow. These effects are comparatively small. For brief moments,  $L_{\text{edd}}$  can be exceeded by a far greater factor, for example, during a flare or a nova.

## 1.2 Objects powered by accreting black holes

Accretion onto compact objects powers X-ray sources across size scales, from binary systems with stellar mass black holes to active galactic nuclei. In the following, I introduce the objects relevant to the research presented in Ch. 3 and 4. For an overview of relevant basic concepts of X-ray spectroscopy, see Sect. 2.2.

### 1.2.1 Active galactic nuclei

Active galaxies are characterised by the strong emission from their centres, which can exceed the stellar luminosity of the galaxy by orders of magnitude. The strong central emission can give the most luminous, distant active galaxies the appearance of point sources, coining the name quasi-stellar object (QSO or quasar). Luminosities of  $L \sim 10^{40}$ – $10^{50}$  erg s<sup>-1</sup> and strong, short-term variability cannot be reconciled with stellar emission. However, these characteristics can be explained if accretion onto a super-massive black hole ( $\sim 10^8 M_\odot$ ) is evoked as the source of energy. This picture of the central engine of active galactic nuclei (AGN) is supported by multiple, independent lines of evidence (see Seward & Charles 2010, Ch. 14.4).

The very high masses of these super-massive black holes are believed to have built up about 10 billion years ago, at a redshift of  $z = 2$ – $3$ , by super-Eddington accretion of the ample amounts of gas available in the early universe (see King 2003, and references therein). The activity, i.e., luminosity, has decreased since then. A important factor for this decrease has been self-regulation: the intense radiation that is a by-product of accretion hampers the supply of material and drives winds, which introduce further feedback processes. Note that AGN evolution is impacted by other factors as well and that the interplay between AGN activity and star formation is an important aspect for the evolution of the galaxy as a whole. Section 3.1 discusses this aspect further.

Observations across the electromagnetic spectrum reveal the variety and complexity of structures that make up AGN (see Fig. 1.1). In the following, a selection of important

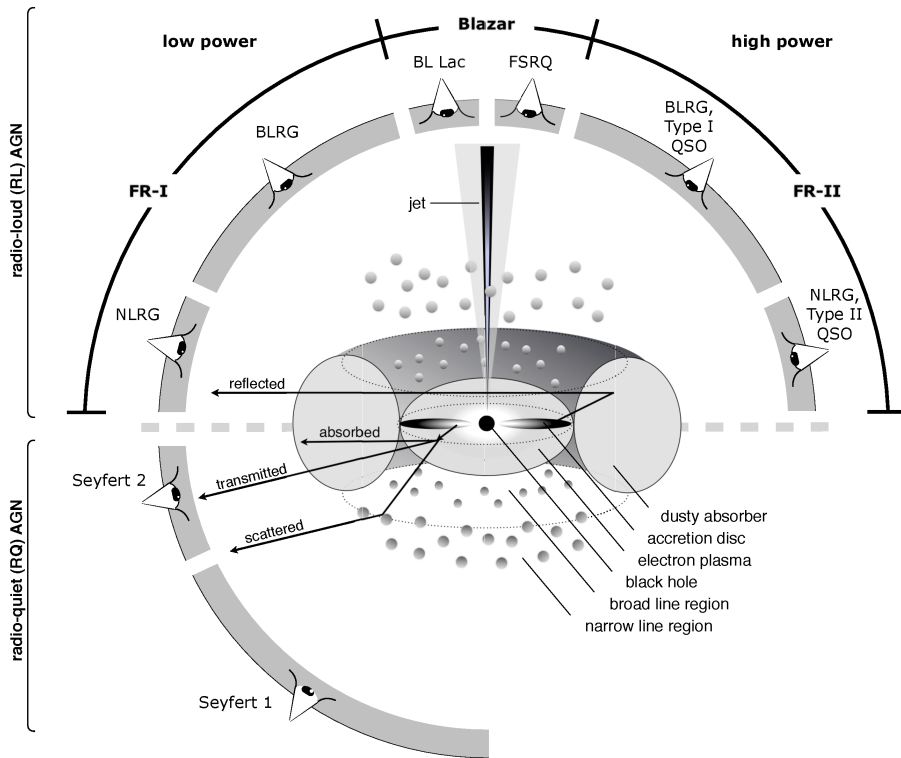


Figure 1.1: Summary diagram of the AGN standard paradigm (Beckmann & Shrader 2012, Fig. 4.16). Different spectral characteristics in the optical are used to classify AGN and are suggested to arise from different viewing angles, as shown. The dashed line splits the figure: the upper half represents a radio-loud, the lower a radio-quiet AGN. Note that the jets in radio-loud AGN are expected to flow out symmetrically north and south of the accretion disc. Refer to the text for further details.

spectral features is highlighted, before the X-ray spectrum is discussed in the next paragraph. The optical/UV spectrum can show a so-called big blue bump from the accretion disc black body emission, as well as resonant line emission from the narrow and broad line regions. The broad line region is located closer to the AGN central region, where the orbital motion of the emitting cold gas clouds causes line broadening ( $10^3$ – $10^4$  km s $^{-1}$ , see Beckmann & Shrader 2012, Ch. 3). Reprocessed emission from a dusty torus can be observed in the infrared. Particle acceleration in relativistic, highly collimated outflows (so-called jets) results in radio and gamma ray emission (see Beckmann & Shrader 2012, Ch. 5). The visibility of the spectral characteristics associated with these structures strongly varies between AGN classes, which are defined according to the optical characteristics. The variety is suggested to arise from the viewing angle as indicated in Fig. 1.1, even though this notion is contested. Only the differentiation between AGN with and without radio emission (radio-loud and radio-quiet AGN, respectively) is relevant in

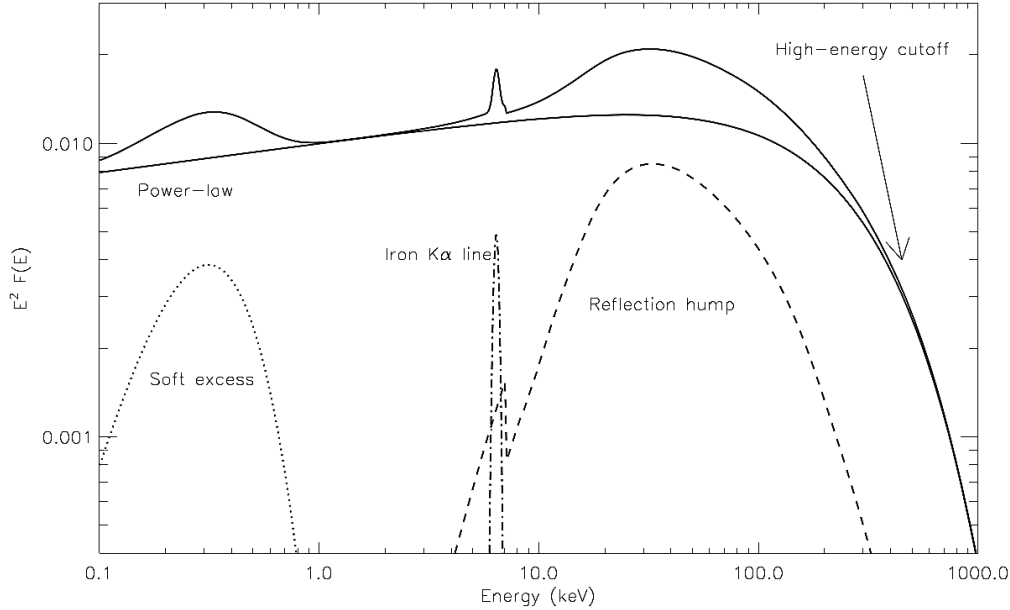


Figure 1.2: Schematic X-ray spectrum of a radio-quiet AGN (Beckmann & Shrader 2012, Fig. 5.14). Note that the displayed spectrum presents an example and that the relative strength of the components strongly depends on the source. The  $y$ -axis is multiplied by an energy term  $E^2$  to highlight the features in the spectrum. A description of the spectral components can be found in the text.

the following. The terms *AGN* and *quasar* will be used interchangeably and not strictly according to the optical classification scheme. The remainder of this section will focus on radio-quiet AGN, as those harbour the outflows investigated in Ch. 3.

X-rays are produced by highly energetic processes that take place in the direct vicinity of the super-massive black hole and therefore open a window to the innermost regions of AGN. The spectra of Seyfert galaxies, a class of radio-quiet AGN (see Fig. 1.1), show multiple features which can be ascribed to structures present in the central region (for a model see, e.g., Haardt & Maraschi 1991). The spectral components are discussed below and sketched in Fig. 1.2.

**Powerlaw** X-ray spectra of AGN are dominated by a powerlaw component, which is believed to come from a corona of hot electrons that Compton up-scatters<sup>2</sup> photons from the accretion disc. The accretion disc spectrum itself is not prominent in X-rays, but

<sup>2</sup>In this case, the scattering transfers energy from the electrons to the photons. This up-scattering is possible because the electrons are highly energetic and is also referred to as inverse Compton scattering. The opposite case applies in the discussion of  $L_{\text{edd}}$  in Sect. 1.1, i.e., the photons are down-scattered, transferring energy onto the accreting electrons.

peaks in the UV<sup>3</sup>. The corona may form due to the high temperatures and luminosities at the inner accretion disc lifting off (“evaporating”) electrons from the disc, or at the base of a relativistic jet. The geometry of the corona is still debated. The powerlaw possesses a high-energy cut-off which is indicative of the temperature of the coronal electrons,  $\sim 10^8$  K (see Seward & Charles 2010, Ch. 14, and Beckmann & Shrader 2012, Ch. 5).

**Reflection** Part of the coronal X-ray emission hits the accretion disc and is scattered towards the observer. The interactions of the hard X-ray photons from the corona with the comparatively cool gas in the accretion disc imprint signatures onto the spectrum: the hard coronal photons get Compton down-scattered in the cooler accretion disc and are redistributed into a so-called reflection hump. Hard photons also ionise the upper layers of the disc, giving rise to X-ray fluorescent emission lines<sup>4</sup>. The most prominent of these emission lines is the Fe K $\alpha$  line, due to the comparatively high abundance of iron and the strength of the K $\alpha$  transition. As reflection takes place very close to the central black hole, the Fe K $\alpha$  line is deformed by multiple relativistic and non-relativistic effects, giving it a great diagnostic potential, e.g., it can be used to measure the black hole spin (see Dauser et al. 2016, as well as Seward & Charles 2010, Ch. 14, and Beckmann & Shrader 2012, Ch. 5). The spectrum resulting from reflection according to the relativistic RELXILL model (García et al. 2014) is shown in Fig. 1.3.

**Soft excess** AGN spectra often contain an excess of X-rays relative to the powerlaw at  $\lesssim 1$  keV, the origin of which is a topic of active research (see Beckmann & Shrader 2012, Ch. 5, and references therein). While a similar feature can result from unresolved emission lines created by reflection, the soft excess is featureless also at higher resolutions and consistent modelling with reflection features is not always possible. However, reprocessed, hard reflection photons could present an explanation. A second plausible origin is a collisionally excited plasma in the vicinity of the black hole.

**Line absorption** In addition to the above mentioned components, AGN spectra can contain absorption lines. The absorption arises in outflowing or revolving clouds of material above the accretion disc plane. Blue-shifted absorption lines are a signature of accretion disc winds (see Sect. 3.1).

---

<sup>3</sup>The spectrum can be described as a sum of black-body components, because the disc temperature,  $T$ , changes with radius,  $r$ , according to  $T(r) \propto r^{-3/4}$  (see Longair 1994, Ch. 16.3). The temperature at the inner edge of the disc,  $T_{\text{in}}$ , determines the energies to which the spectrum extends. From the fact that  $r_{\text{g}}$  scales linearly with the black hole mass,  $M$ , (Eq. 1.1) and the relation for  $T(r)$  given above,  $T_{\text{in}} \propto (\dot{M}M^{-2})^{1/4}$  can be shown (see Longair 1994, Ch. 16.3). In AGN, disc emission therefore peaks at lower energies than in galactic sources, where X-ray energies are reached.

<sup>4</sup>X-ray florescence emission arises if absorption of an energetic photon causes the ejection of an inner shell electron which is then replaced by an electron from a higher shell, resulting in line emission. The emitted photon has a lower energy than the incident, ionising photon (see Arnaud et al. 2011, Ch. A.1.1).

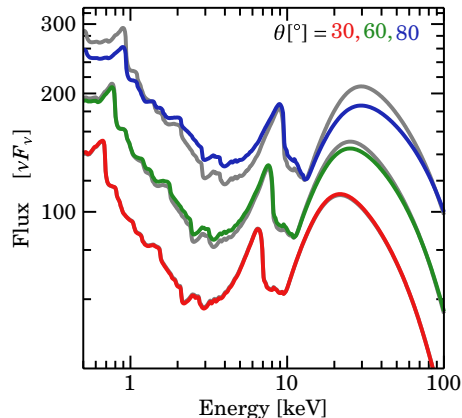


Figure 1.3: An example of a reflection spectrum predicted by the relativistic RELXILL model (García et al. 2014, Fig. 6). The colours represent different polar viewing angles. The typical reflection features described in the text are clearly visible: the broadened Fe K $\alpha$  emission line and the reflection hump above 10 keV.

AGN are variable on timescales ranging from days to years. The intrinsic short-term variability in radio-quiet AGN has a characteristic red-noise frequency distribution,  $\propto f^{-\alpha}$ , where  $f$  is the frequency and  $\alpha = 1-2$  (see Vaughan et al. 2003). The red-noise distribution is suggested to be caused by stochastic fluctuations in the angular momentum transport in the accretion disc (e.g., Hogg & Reynolds 2016, and references therein). Long-term luminosity changes likely arise from the variability in the supply of accreting material or from absorbing clouds. In radio-loud AGN, a considerable amount of variability can be introduced by the jet (see Beckmann & Shrader 2012).

### 1.2.2 Black hole X-ray binaries

In binary a system, a star can fuel accretion onto a black hole or neutron star and turn it into an X-ray source. The strongest X-ray sources in our Galaxy fall into this category of X-ray binaries (XRBs). The study of XRBs can shed light on the physics of compact objects, relativity, and accretion in the highly ionised environment the X-rays create. A wide variety of observational phenomena is associated with XRBs and related to the nature of the compact object, the type of star, and the orbital configuration. For example, neutron star XRBs can show pulsations and flares due to their strong magnetic fields and solid surfaces, while it is much harder to unambiguously identify black hole XRBs (see Seward & Charles 2010, Ch. 11 and 12). In the following, I focus on the case of a black hole and a massive star.

In high mass X-ray binaries (HMXBs), the compact object ploughs through the strong stellar wind of the O or B companion star, creating a shock front and a wake trailing behind it (see Fig. 1.4). Within the shock front, material from the stellar wind collapses onto the compact object without forming an accretion disc. In contrast, XRBs with lower mass stars accrete by Roche lobe overflow. The Roche lobe is the equipotential line that

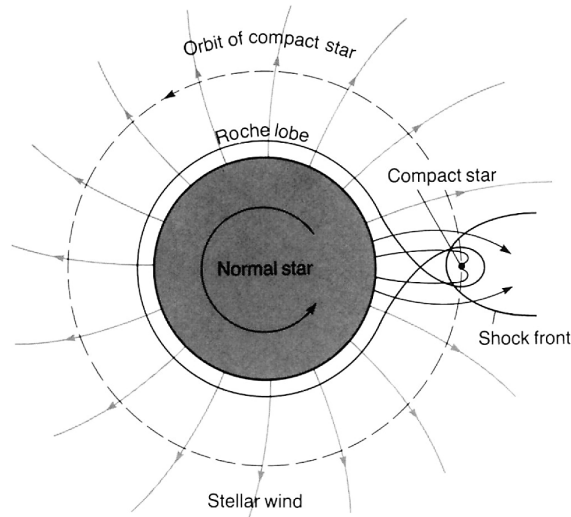


Figure 1.4: Wind accretion in an HMXB (Longair 1994, Fig. 16.10): accretion onto the compact object (indicated as “compact star”) is fuelled by the strong stellar wind of the O or B companion.

includes the inner Lagrangian point,  $L_1$ , at which the gravity of the star and the compact object cancel out, such that their Roche lobes touch (see Fig. 1.4). If the companion fills its Roche lobe, material can be transferred onto the compact object through  $L_1$ , forming an accretion disc (see Longair 1994, Ch. 16). Note that these scenarios are not mutually exclusive, i.e., a massive star with a strong wind can also lose material via  $L_1$  if it is close to filling its Roche lobe, such as in the example of Cygnus X-1 (see Ch. 4).

Similar to AGN, spectra of black hole XRBs can show signatures of a hot electron plasma, an accretion disc, a jet, and absorption in clouds or clumps of material. The similarity can be ascribed to the self-similarity of accretion flows with respect to a scaling of the black hole mass. Two X-ray spectral states are broadly differentiated in XRBs: the hard state is dominated by a powerlaw component from hot electron plasma. In the soft state, emission from the accretion disc dominates, which is observable in X-rays because the inner accretion disc can reach higher temperatures than in AGN (see footnote 3). The nomenclature comes from the fact that the disc spectrum is softer than the powerlaw, i.e., it is falling off faster with energy. XRBs display long-timescale changes between these states, which are believed to arise from a complex dynamics that is changing the geometry (see Seward & Charles 2010, Ch. 12).

Black hole XRBs show a similar pattern of stochastic red-noise variability as AGN. It was suggested that this pattern is a signature unique to accretion onto black holes and that it could be used to identify them. However, some neutron star XRBs have been found to display the same behaviour (see Seward & Charles 2010, Ch. 12).



Figure 1.5: Powerful feedback from massive stars and AGN. *Left*: the Carina nebula, a star-forming region exhibiting a diffuse X-ray glow, likely from massive star winds and supernova explosions (X-rays: NASA/CXC/PSU/L. Townsley et al.). *Right*: the Phoenix galaxy cluster, in which feedback from a supermassive black hole might boost star formation in the cool gas in the cluster’s centre. Reduced X-ray emission (*purple*) and the presence optical filaments (*orange, green, blue*) indicate the cool gas (X-ray: NASA/CXC/MIT/M. McDonald et al.; Radio: NRAO/VLA; Optical: NASA/STScI).

## 1.3 Outflows

Outflows are a common feature of accreting systems, ranging from wide-angled accretion disc winds to highly collimated jets (see Seward & Charles 2010, Ch. 14). They also arise in other astronomical settings, for example in massive stars. Outflows can reach highly relativistic speeds and drive out a significant amount of material, resulting in feedback processes that can heavily regulate accretion flows and the evolution of the object. If the driving force is sufficient to overcome the escape velocity, the outflow leaves the system and can have an impact on a much larger scale, by depositing its momentum and energy in swept up material (see examples in Fig. 1.5). Such large-scale feedback likely plays an important role in shaping galaxies and regulating star formation and presents a major motivation to study outflows (see Seward & Charles 2010, Ch. 7 and 14).

A key question in the study of outflows is by which mechanism they are accelerated (“driven”). A basic example was hinted at in Sect. 1.1: photons can transfer momentum onto the outer layers of a star or accretion disc by Compton scattering, creating an outflow if the luminosity is high enough to overcome gravity, i.e., if  $L_{\text{edd}}$  is exceeded. This so-called continuum driving requires large luminosities (e.g., King & Pounds 2003). At lower luminosities, outflows can be driven if processes with a larger cross-section are available, such as resonant line absorption and scattering in ions in the gas (e.g., Castor et al. 1975). Line scattering results in a net outward force, because the photons

## 1 Introduction

have a preferred direction, away from the source. The absorption transfers the outward momentum of the photons onto the wind, which is only partly counteracted for by re-emission, because the re-emission is isotropic. Typically, the bulk of the driving force is transmitted in a few specific lines. The momentum is then distributed among the whole gas by Coulomb scattering. Line driving strongly depends on parameters like metal abundance and the ionisation, as strong lines of the driving ions have to be present. A second, powerful driver of outflows are magneto-hydrodynamic forces, which arise in the complex, dynamic electromagnetic field structures that are embedded in the plasma. Magneto-hydrodynamic forces are independent of the luminosity, but instead require a highly dynamic plasma flows. For example, jets are believed to be collimated by wound-up magnetic field structures, very close to rotating black holes (see Seward & Charles 2010, Ch. 14).

The X-rays created in accretion processes can be used as probes to study outflows, by measuring their X-ray absorption. I investigate winds in two different contexts in this Master's thesis. Chapter 3 concerns ultra-fast outflows, wide-angled accretion disc winds of AGN that can reach relativistic speeds. Due to their high velocities, ultra-fast outflows possess a huge amount of mechanical power and are thought to be important for understanding AGN feedback and evolution. In Ch. 4, I study the structure of a strong wind of a massive star in an HMXB. Winds of massive stars impact stellar evolution due to the mass-loss they induce and provide mechanical feedback. The method applied in both cases utilises the variability present in many accreting systems and is introduced in the next chapter.

## 2 Methods and Instrumentation

This chapter aims to give an overview about the instrumentation and methods that are used to study accreting systems. Section 2.1 explains the measurement of X-ray photon energies with CCDs and introduces the X-ray instruments that were used to take the data analysed in this thesis. In Sect. 2.2 and Sect. 2.3, X-ray spectroscopy and variability are introduced separately, before discussing excess variance spectroscopy in Sect. 2.4, a method for studying the wavelength-dependent variability, which is the foundation of the research introduced in Ch. 3 and 4.

### 2.1 Instrumentation

The instrumentation introduced in the following focuses on X-ray spectroscopy, which requires the accurate measurements of X-ray photon energies. Chapter 3 of the *Handbook of X-ray astronomy* (Arnaud et al. 2011) and Ch. 3 of *Exploring the X-ray universe* (Seward & Charles 2010) have been used as the main references.

#### 2.1.1 Measuring X-ray photon energies

The introduction of Charged Coupled Devices (CCDs) as X-ray detectors in the early 1990s has greatly improved the energy resolution of X-ray instruments, allowing X-ray spectroscopy to truly take off and surpass the capabilities of proportional counters and scintillators. CCDs are semi-conductor based photo detectors, which were also widely used in common digital cameras<sup>1</sup>. CCDs measure the X-ray photon energy via the number of electron-hole pairs that are created during absorption. This presents an important difference to the use of CCDs in the context of optical astronomy or photography. In optical detectors, one incident photon on average moves one electron from the valence band to the conduction band in the semiconductor, creating one electron-hole pair. The optical detector then measures light intensity by collecting and counting the charge accumulated over time. In contrast, X-rays create  $\sim 1000$  pairs, due to their higher energy, such that individual photons can be measured (see Arnaud et al. 2011, Ch. 3.2). X-ray CCDs literally count photons, with the intensity, or brightness, being measured in counts per second ( $\text{cts s}^{-1}$ ).

When combined with diffraction gratings, the spectral resolution can be increased further by over an order of magnitude up to, e.g.,  $E/\Delta E \sim 1000$  in the case of *Chandra's* High Energy Grating (Canizares et al. 2005). The photon's energy is inferred from its position on the chip to which it has been diffracted by the grating. This spreading-out

---

<sup>1</sup>Nowadays, most camera sensors are CMOS sensors, in which each pixel is read out individually.

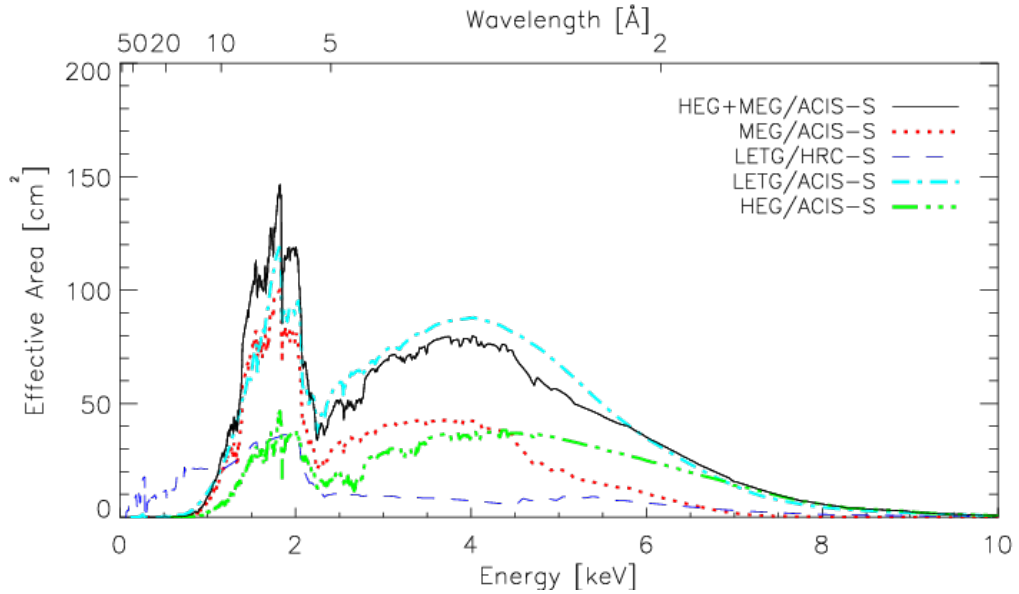


Figure 2.1: The effective area of *Chandra*'s spectrometers, given for the first order of diffraction (The Chandra Proposer's Observatory Guide, Fig. 1.4).

of the signal reduces the sensitivity that a detector of a given size can reach, such that the choice between gratings and CCD based spectroscopy always comes with a trade-off between resolution and signal. Microcalorimetry presents an exciting prospect to tackle this issue, by providing more accurate pixel-based energy measurements, based on the temperature increase a X-ray photon causes when hitting the detector. Within the next decade, the *XRISM* (Tashiro et al. 2018) and *Athena* (with the X-IFU spectrometer, Barret et al. 2018) missions are scheduled to launch, reaching resolutions that are comparable or superior to that of gratings. Until then, existing CCD and gratings technology will provide many more existing results, as it has done over the last 30 years.

### 2.1.2 X-ray satellites

X-rays are absorbed by the Earth's atmosphere. X-ray observatories therefore have to be spaceborne. After a brief overview of instrumental characteristics, I introduce the X-ray satellites *XMM-Newton* (Jansen et al. 2001) and *Chandra* (see Weisskopf et al. 2000), which have provided the data analysed in this thesis. Both instruments have good capabilities in a similar range ( $\sim 0.2$ – $10$  keV).

An important quantity that characterises the sensitivity of an X-ray observatory is the **effective area**, which is analogous to the opening area of an optical telescope multiplied with the detection efficiency. As the efficiency is generally a function of energy, so is the effective area (see an example for *Chandra* in Fig. 2.1). With additional knowledge of the response matrix, which gives the probability that a photon of a given energy is registered in a certain energy channel in the detector, spectral analysis can infer the flux of a

source from the count rate the instrument measures<sup>2</sup>. An other important characteristic, especially in the context of X-ray imaging, is the **field of view**, i.e., the area on the sky that is imaged by the instrument. How well the optics collimate X-ray photons is measured by the width of the **point spread function**, i.e., the image of a point source on the detector. In addition to the **spectral resolution**, an instrument also has a **time resolution**, given by the detector read-out speed. Timing characteristics are important when studying variable objects, but also determine an instrument's ability to observe bright sources: X-ray CCDs are built to register individual photons and the arrival of multiple photons in the same pixel during one read-out window, called pile-up, distorts the measured photon count and energy.

**XMM-Newton** Launched in 1999 by the European Space Agency (ESA), the *XMM-Newton* observatory<sup>3</sup> (Jansen et al. 2001) is still among the most important X-ray missions in operation, thanks to its versatility and high effective area. Figure 2.2 shows an artist's impression. *XMM-Newton* carries three individual telescopes, hence the name *Multi-Mirror Mission (XMM)*, behind which sit CCD detectors, the European Imaging Cameras (EPICs: EPIC-pn, EPIC-MOS 1 and 2). High resolution spectroscopic measurements can be taken with the two Reflection Grating Spectrometers (RGSs), which share telescopes with the two MOS detectors. The Wolter type I mirror in each of the three telescopes consists of 58 nested shells, which focus the X-rays by consecutive total reflection on a parabolic and hyperbolic surface (see Fig. 2.3, left-hand side, for a schematic of the Wolter type I mirror on *Chandra*). Such a grazing-incidence construction is necessary, because X-rays are so energetic that they would pass through the mirror material at greater incidence angles. In addition to the X-ray telescopes *XMM-Newton* also carries an optical monitor (OM).

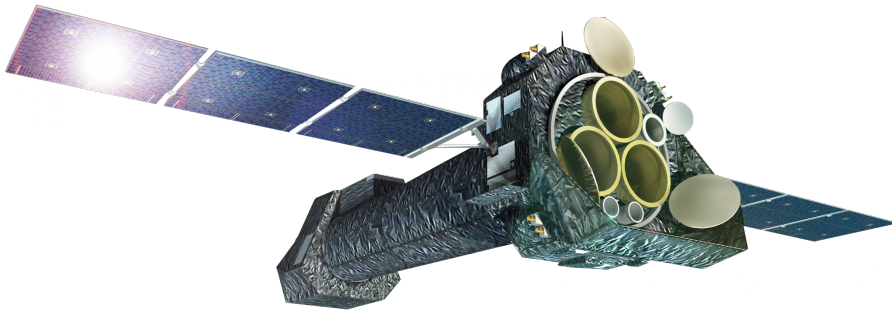


Figure 2.2: Artist's impression of *XMM-Newton* (Illustration: ESA/D. Ducros)

<sup>2</sup>Mathematically, the expression  $n(c) = \int_0^\infty R(c, E) \cdot A(E) \cdot F(E) dE$  has to be inverted to obtain the flux as a function of energy,  $F(E)$ , from the number of counts measured in a certain channel,  $n(c)$ , the effective area,  $A(E)$ , and response,  $R(c, E)$  (see Arnaud et al. 2011, Ch. 4).

<sup>3</sup>see XMM-Newton: A Technical Description

(<https://www.cosmos.esa.int/web/xmm-newton/technical-details>, visited August 18, 2021, 9:12 am)

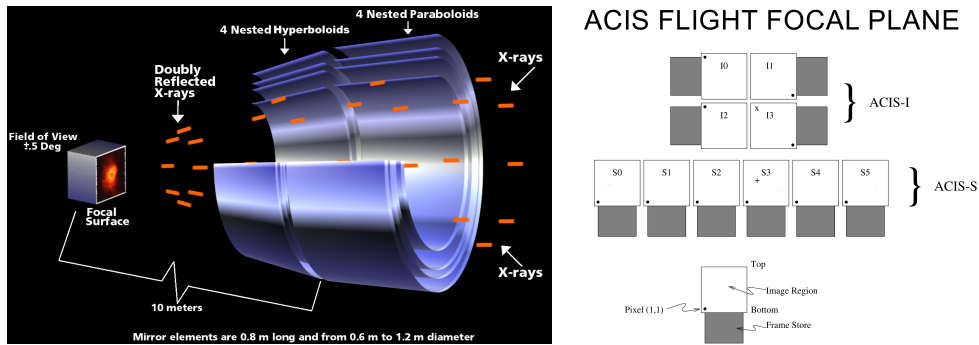


Figure 2.3: *Left*: schematic of the Wolter Type I mirrors in *Chandra* (Illustration: NASA/CXC/D. Berry). The X-rays are focused by consecutive total reflection on a paraboloid and a hyperboloid surface. *Right*: the *Chandra* ACIS detector (Illustration: NASA/CXC), with is subdivided in the quadratic ACIS-I (imaging) and the row of the ACIS-S (spectroscopy).

**Chandra** *Chandra*<sup>4</sup> (Fig. 2.4) is a NASA mission that was also launched in 1999 (see Weisskopf et al. 2000). It has a lower effective area than *XMM-Newton*, but shares the good spectroscopic capabilities, thanks to the Low- and High Energy Transition Gratings (LETG and HETG, respectively), which diffract photons on the Advanced CCD Imaging Spectrometer (ACIS; Garmire et al. 2003). The layout of the detector is shown in Fig. 2.3 on the right-hand side: the ACIS is subdivided into the ACIS-I and the ACIS-S, the latter of which is used to perform the spectroscopic measurements. The HETG, which was used for the work of this thesis, further consists of two arms, which are mounted in a cross-like shape, the High and Medium Energy Gratings (HEG and MEG respectively; Canizares et al. 2005), together covering the 0.4–10 keV range. A full read-out of the ACIS-S takes 3.2s, but the relevant timing characteristics can vary with the operating mode, e.g., the read-out is faster if pixel columns are read out one by one as in the Continuous Clocking mode. In addition to the ACIS, *Chandra* carries the High Resolution Camera (HRC), which can also be operated with the LETG.



Figure 2.4: Artist's impression of *Chandra* (Illustration: NASA/NGST).

<sup>4</sup>see CXC/science instruments ([https://chandra.harvard.edu/about/science\\_instruments.html](https://chandra.harvard.edu/about/science_instruments.html), visited August 18, 2021, 9:11 am)

## 2.2 X-ray spectroscopy

X-ray spectroscopy studies absorption and emission features in gases that arise from electron transitions. These transitions can either go from one bound state to another (resonant line transitions) or be bound-free transitions, in which an electron is ejected (absorption edges). Of special importance to astronomy is the study of photoionised gases, i.e., gases that have been ionised by energetic photons, such as X-rays. Spectroscopy reveals the element abundances and is used for plasma diagnostics, i.e., for characterising a gas by its ionisation, temperature, and density, making it a powerful tool for astronomy.

Nomenclature and basic concepts that are relevant in the following are briefly introduced in Sect. 2.2.1 and 2.2.2. Sect. 2.2.3 explains the analysis of spectra, a step which takes place after the raw data from the instrument have been extracted and pre-processed. The introduction of the PhD Thesis by Hanke (2011) and Ch. 5, 7, and Appendix 1 of Arnaud et al. (2011) have been used as references for this section. See these for more details, especially regarding aspects of atomic physics and the statistical underpinning of spectral analysis, which are only touched upon here.

### 2.2.1 Basics and nomenclature

**Shells** In X-ray astronomy, the innermost atomic shell, associated with the principle quantum number  $n = 1$  is called the K-shell, followed by the L-, and M-shells for  $n = 2$  and 3 etc. Only transitions in the inner shells are relevant to X-ray astronomy, due to the high energies of the X-ray photons and the scaling of the distances of the shells.

**Ions** In astronomy, ionisation states are numbered with Roman numbers, where I refers to the neutral state, II is once ionised and so on. For example, Fe II equals  $\text{Fe}^+$ . Ions are also labelled according to the number of electrons they possess, e.g., a nucleus with one electron is called hydrogen-like (H-like) and helium-like (He-like) with two electrons. This convention is appropriate, because the number of electrons determines which kinds of transitions can take place within the ion. The name of the outermost occupied shell is sometimes also given, e.g., L-shell iron refers to Fe XVII–XIV. Highly ionised, H- and He-like (K-shell) ions are common around sources that emit large amounts of ionising X-ray radiation, such as AGN or XRBs (see Ch. 1).

**Transitions** Inner shell electron transitions are labelled with the name of the lower state shell and a Greek letter, enumerating the distance to the higher shell, e.g.,  $K\alpha$  is a transition between the K-shell and the next higher shell, the L-shell (Siegbahn notation). The nomenclature of the Lyman (Ly) series is adopted for H-like ions, i.e.,

$$\text{Ly } x : 1s(^2S_{1/2}) \longleftrightarrow np(^2P_{3/2} \text{ or } ^2P_{1/2}), \quad (2.1)$$

where  $n = 2, 3, 4$  for  $\text{Ly } x = \alpha, \beta, \gamma$  etc. As an example,  $\text{Fe } K\alpha$  is equivalent to  $\text{Fe } \text{Ly } \alpha$  and refers to a  $1s \longleftrightarrow 2p$  transition. The name of the lower shell can be omitted if it is clear from context, e.g.,  $\text{Ne } \text{He } \alpha$  refers to a K-shell transition. In emission, the  $K\alpha$

line from He-like ions is also abbreviated r (resonance line), as it forms a triplet with the intercombination (i) and forbidden (f) lines. As atomic structure goes far beyond shells, these naming conventions are approximate, but serve well if details are not required.

## 2.2.2 Relevant concepts

**Column density** The column density,  $N$ , measures the amount of material between the X-ray source and the observer, by integrating the particle number density,  $n(r)$ , along the line of sight (LOS), i.e.,

$$N = \int_{\text{LOS}} n(r) dr. \quad (2.2)$$

$N$  is often given for a specific element, e.g.,  $N_{\text{Ne}}$ , or rescaled to the abundance of hydrogen, which is then called the equivalent hydrogen column density,  $N_{\text{H}}$ .

**Optically thin/thick** Optically thick media can be assumed to absorb all incident photons and emit black body radiation. In contrast, an optically thin medium can be considered transparent. Both terms come from the context of the optical depth,  $\tau = N\sigma$ , which is the average path a photon travels in a medium before it is absorbed, for a given column density,  $N$ , and absorption cross section,  $\sigma$ .

**Ionisation** The ionisation parameter characterises the ionisation state of an optically thin medium, by comparing the luminosity that is available to ionise the gas<sup>5</sup>,  $L_{\text{X}}$ , to its density,  $\rho(r)$ , and distance from the ionising source,  $r$ , (Tarter et al. 1969):

$$\xi(r) = \frac{L_{\text{X}}}{\rho(r)r^2}. \quad (2.3)$$

In short,  $\xi(r)$  represents the ratio of ionising photons to ionisable particles. The ionisation is indicative of the abundances of ions in a gas (see, e.g., Fig. 4.11). At  $\log \xi \gtrsim 5$ , a gas can be considered fully ionised, i.e., no resonant line transitions are observed in the spectra of such gases, as the electrons are unbound.

**Soft and hard X-rays** Soft and hard X-rays are relative terms, soft X-rays referring to lower energetic photons than hard X-rays. In the context of X-ray spectroscopy, the line between hard and soft X-rays is typically drawn at  $E \sim 2.5$  keV.

---

<sup>5</sup>Radiation requires at least 13.6 eV to be ionising, the ionisation energy of hydrogen.

### 2.2.3 Spectral fitting

X-ray spectra can be modelled using specialised software like ISIS<sup>6</sup> or XSPEC (Arnaud 1996). Modelling in this context refers to fitting empirical or physical model functions to the data. As an example, non-thermal emission from hot electrons in the X-ray corona of AGN takes the spectral shape of a (cut-off) powerlaw (see Ch. 1). Physical models can fit parameters that characterise the physical conditions in the source, e.g., the absorbing column density and the ionisation (see Sect. 2.2.2). By comparing the fit statistics of different models, or different combinations of models, it is possible to identify how consistent each of these scenarios is with the observed spectrum (see Arnaud et al. 2011, Ch. 5). A commonly used fit statistic is the  $\chi^2$  statistic,

$$\chi^2 = \sum_i \frac{(X_i - M_i)^2}{\sigma_i^2}, \quad (2.4)$$

which is the sum of the squared deviations of the model values,  $M_i$ , from the data,  $X_i$ , relative to the measurement uncertainty,  $\sigma_i^2$  (see Arnaud et al. 2011, Ch. 7). The fit statistic should be selected according to the probability distribution that describes the number of counts. Generally, the counts are expected to follow a Poisson distribution. For  $\gtrsim 100$  counts, the Poisson distribution is well approximated by a Gaussian distribution, for which  $\chi^2$  is appropriate. At lower counts, the so-called Cash statistics should be applied, as it represents Poissonian behaviour (Gehrels 1986). For  $\chi^2$ , a good fit has  $\chi^2/\text{dof}$  close to 1, where dof are the degrees of freedom, i.e., the number of parameters in the fit than can vary freely. A value higher than one indicates the model is not able to account for all features of the data, while a lower value often is a result of overfitting, i.e., the model describes the data better than statistically expected, because dof is too high (see Arnaud et al. 2011, Ch. 7).

Complex models often take the form of a table model, i.e., a grid of pre-calculated values that is interpolated during the fit. The behaviour of photoionised gases specifically can be modelled with photoionisation codes like XSTAR (Kallman & Bautista 2001), which model the ionisation state of the gas from the X-ray illumination and the radiative transfer, i.e., from the interactions of X-ray photons travelling through the gas. Models generated in this way can consistently predict a full spectrum and are therefore more informative than fitting lines individually with Gaussian profiles (see Hanke 2011, Ch. 1).

---

<sup>6</sup>see the ISIS homepage (<https://space.mit.edu/cxc/isis/index.html>, visited August 18, 2021, 10:53 am).

## 2.3 X-ray variability

Variability studies investigate the change in an object’s flux with time, i.e., in its light curve. Generally, variability can either be intrinsic, or be due to obscuration by structures moving across the line of sight (“weather”). Intrinsic variability in AGN or XRBs can be caused, for example, by fluctuations in the accretion rate or angular momentum transport in the accretion disc (see Sect. 1.2.1). The flux can also vary periodically, due to orbital motion or rotation.

Variability analyses are often applied to investigate the size of an astronomical object, or the region within the object that harbours the variable process. In this way, they complement spectral analyses, which provide only static information and are on their own not well suited to constrain geometry. The size estimate is based on the light travel time: the information that the flux has changed due to some underlying process requires time to travel across the variable region. The region cannot vary as a whole on timescales shorter than that. Galactic sources therefore vary at higher frequencies than extragalactic sources, which are orders of magnitude bigger (see Longair 1994, Ch. 16, and Seward & Charles 2010, Ch. 14.7).

A variety of techniques are available to characterise an object’s variability, involving, e.g., Fourier transformation to investigate the frequency behaviour and identify different variability components (van der Klis 1989). For example, due to the size scaling discussed above, the frequency spectrum of accreting black holes flattens at a specific timescale, which can be used to measure the black hole mass (McHardy et al. 2006). Time lags between different spectral components or bands can be used to map out the geometry of variable regions, as, e.g., applied by X-ray reverberation mapping (for a review see Uttley et al. 2014). If enough signal is available, spectral analyses can be performed for different source states of fluxes, allowing for a monitoring of spectral changes (phase/flux resolved spectroscopy), which can help identify physical processes underlying the variability (see Pinto et al. 2018, for an example in the context of AGN accretion disc winds).

## 2.4 Excess variance spectroscopy

The joint analysis of spectral and timing data can provide unique physical insights, as they complement each other in their diagnostic power (see the two previous sections). An approach which excels at this aim is excess variance spectroscopy, which can, given enough resolution, characterise the variability of individual spectral lines. I apply this method in Ch. 3 and Ch. 4 to study AGN ultra-fast outflows and massive star winds, respectively. See these chapters for details and motivation for applying excess variance spectroscopy in these contexts. A conclusion on the capabilities of the method is drawn in Ch. 5. The text below is taken in part from the manuscript of Härer et al. (2021b).

The excess variance quantifies the variability of an object and is defined as (Edelson et al. 2002; Vaughan et al. 2003)

$$\sigma_{\text{XS}}^2 = S^2 - \overline{\sigma_{\text{err}}^2}, \quad (2.5)$$

where  $S^2$  is the time variance of the light curve and  $\overline{\sigma_{\text{err}}^2}$  the arithmetic mean of the squared measurement uncertainty, i.e., the variability introduced by the statistical nature of the measurement process. If the data are Poisson distributed,  $\overline{\sigma_{\text{err}}^2}$  can be estimated to be the mean count number,  $\bar{x}$ . Subtracting the statistical noise makes the excess variance a quantity which is indicative of only the physical variability of the source, i.e, if no variability is present, the excess variance is zero. Note that any systematic background that is expected to be variable should be subtracted before calculating the excess variance, because it would contaminate the signal. Constant background is automatically excluded, because only the variance of the signal is considered. The excess variance depends on source flux, which is corrected for by normalising it to  $\bar{x}^2$ :

$$F_{\text{var}}^2 = \frac{\sigma_{\text{XS}}^2}{\bar{x}^2}. \quad (2.6)$$

In Eq. 2.6, the normalised excess variance is given in terms of the square of the fractional quantity,  $F_{\text{var}}$ , also called root mean square (RMS) variability.  $F_{\text{var}}$  is often used as it is linear in the number of counts. The main advantage of using the excess variance as a measure for variability is the straightforward application to spectral data, i.e., the calculation of an excess variance spectrum. To judge the significance of features in the excess variance spectrum, an estimate of  $F_{\text{var}}$  uncertainty is required. I use the expression derived by Vaughan et al. (2003) based on a Monte Carlo approach, which, as they show, can account for Gaussian and Poissonian uncertainty. The band pass of frequencies contributing to the excess variance is determined by the time resolution chosen for generating the light curve, the so-called time binning, and the length of the observation. By choosing the time binning, it is therefore possible to probe the frequency dependence of  $F_{\text{var}}^2$  and, e.g., investigate if there is a variability timescale intrinsic to the system.



# 3 Part I: modelling the ultra-fast outflow of the quasar PDS 456

In this chapter, I present improvements to a model by Parker et al. (2020) for the variability of ultra-fast outflows, relativistic, wide-angle accretion disc winds of AGN, which are believed to play an important role in AGN evolution. The improved model is applied to the high-luminosity low-redshift quasar PDS 456, successfully accounting for the broadening of the absorption features observed in the excess variance spectrum. The research introduced in this chapter has been published by Härer et al. (2021). From Sect. 3.4 onwards, this chapter is largely taken verbatim from the publication.

## 3.1 Ultra-fast outflows

Over the last two decades, evidence has grown for highly blue-shifted, broad absorption lines in the X-ray spectra of AGN. These properties indicate that these lines trace material moving at relativistic speeds, close to the central black hole. Independent searches with the X-ray satellites *XMM-Newton* and *Suzaku* have helped piecing together a picture in which these lines are signatures of relativistic accretion disc winds, the so-called ultra-fast outflows (UFOs; Tombesi et al. 2010, 2011; Gofford et al. 2013; Igo et al. 2020). Found in  $\sim 40\%$  of all AGN, including radio-loud AGN (Tombesi et al. 2014), UFOs are characterised by outflow velocities of  $\sim 0.03\text{--}0.3c$  and wide opening angles, allowing for a huge mechanical power of  $L_w \sim 10^{43}\text{--}10^{45} \text{ erg s}^{-1}$ , or  $\sim 0.1\text{--}10\%$  of the Eddington luminosity (Tombesi et al. 2012; Gofford et al. 2015). High column densities,  $N_H \sim 10^{23} \text{ cm}^{-2}$ , and ionisations,  $\log \xi \sim 3\text{--}6$ , indicate that UFOs are launched in the innermost regions of AGN, at only  $\sim 100\text{--}1000$  Schwarzschild radii. At these ionisations, the observed lines are expected to be iron K-shell absorption, i.e., from Fe XXV or Fe XXVI Ly  $\alpha$ . The high velocities and ionisations set UFOs apart from warm absorbers, another type of accretion disc wind. Warm absorbers consist of slower, more neutral gas that is thought to be launched at larger radii (see Reeves et al. 2020, and references therein). An alternative interpretation of the highly blue-shifted absorption lines is that a layer of ionised material co-rotates with the inner accretion disc at relativistic speeds, reflecting radiation from the X-ray corona of the AGN and blue-shifting the Fe K line (e.g., Gallo & Fabian 2013). However, the large proportion of reflected radiation required in such a scenario would leave traces in the spectra that are not ubiquitous in UFO sources (e.g., Nardini et al. 2015) and therefore a co-rotating layer cannot serve as a sole explanation.

Due to their large mechanical power and wide opening angles, which allow them to efficiently couple to ambient gas, UFOs can drive feedback on scales that are much larger than the immediate environment of the black hole. In the vast majority of cases, the estimated mechanical power is sufficient to sweep cold gas out of the surrounding galaxy, quenching star formation (Hopkins & Elvis 2010; Di Matteo et al. 2005). Such feedback processes are a likely candidate to explain the  $M_{\text{BH}}\text{-}\sigma$  relation, an empirical scaling law between the mass of the central black hole to the velocity dispersion in the galactic bulge (King 2003; see also Nardini et al. 2015 and references therein).

Independently of the effect on the galaxy, the question arises what drives UFOs, i.e., accelerates them to the high observed speeds. In general, outflows can be driven by radiative and magnetohydrodynamic forces. Especially during the peak of quasar activity, at a redshift of  $z = 2\text{--}3$ , AGN radiated at a substantial fraction of or even above their Eddington luminosity (see Sect. 1.1) and Compton scattering is expected to have driven relativistic outflows (e.g., King & Pounds 2003). This process is referred to as radiative continuum driving, as opposed to the more efficient line driving, in which the outflow is accelerated by UV line absorption (see Sect. 1.3). Simulations have shown that line driving could play an important role for UFO acceleration specifically (e.g., Hagino et al. 2015; Nomura & Ohsuga 2017), despite the extreme ionisations. It has been suggested that the acceleration region is shielded from X-rays by the upper layers of the disc (Proga & Kallman 2004, and references therein). However, the overall observational evidence is also consistent with continuum driving (see Gofford et al. 2015, and references therein), such that the importance of each mechanism likely depends on the specific conditions in a source. Magnetohydrodynamic forces are also a viable mechanism for UFO acceleration (e.g., Fukumura et al. 2018), especially at lower Eddington rates, and are generally believed to be important for wind launching (see Matzeu et al. 2017, and references therein).

## 3.2 The high-energy low-redshift quasar PDS 456

PDS 456 is the most luminous ( $L_{\text{bol}} \sim 10^{47} \text{ erg s}^{-1}$ ; Simpson et al. 1999; Reeves et al. 2000), radio-quiet quasar known in the local universe ( $z = 0.184$ ) and was discovered by Torres et al. (1997) in the Pico del Dias Survey (PDS). Luminosities like these are more common at the peak of quasar activity (see Sect. 1.2.1). The central black hole is estimated to have  $\sim 10^9 M_{\odot}$  (Nardini et al. 2015). PDS 456 does not only show strong variability (e.g., Reeves et al. 2020), but also highly blue-shifted absorption features that are interpreted as signatures of a multi-component relativistic UFO, which makes it an ideal source to study with excess variance spectroscopy.

The first indication of an outflow came from an 2001 *XMM-Newton* campaign. Reeves et al. (2003) reported a deep absorption trough at  $\sim 8 \text{ keV}$ , the most likely origin of which is highly blueshifted iron K-shell absorption, occurring in an outflow with a velocity of  $v_{\text{out}} \gtrsim 0.10 c$ . A second broad feature at  $\sim 1 \text{ keV}$  was found in the RGS spectrum and is explained by blended iron L-shell lines at a blueshift consistent with that of the iron K-shell absorption.

Since this first detection, follow-up studies have placed the outflow velocity for the hard band, Fe K absorption between  $v_{\text{out}} = 0.24\text{--}0.36 c$  (e.g., Reeves et al. 2009; Nardini et al. 2015; Matzeu et al. 2017; Parker et al. 2018; Boissay-Malaquin et al. 2019). Photoionisation modelling revealed variable column densities,  $N_{\text{H}} \gtrsim 10^{23} \text{ cm}^2$ , and ionisations of  $\log \xi \sim 5$ , at which the medium is almost fully ionised and the absorption is expected to be Fe XXVI Ly  $\alpha$ . Nardini et al. (2015) estimate the launching radius to be within a few 100 Schwarzschild radii,  $r_{\text{g}}$ , based on the variability timescale; a result, which is consistent with the extreme ionisation.

By reviewing archival data, Matzeu et al. (2017) discovered a correlation between  $v_{\text{out}}$  and the luminosity of PDS 456, which is interpreted as evidence for a radiatively driven outflow. A higher luminosity means that more radiation is available for the driving, which leads to higher wind speeds. This trend is not per se expected for magnetohydrodynamic driving, but does not exclude such a scenario (Fukumura et al. 2018).

Multiple studies found indications that the outflow, as measured from the iron K absorption, is structured, i.e., good-quality fits require more than one photoionisation model component (Reeves et al. 2009, 2018, 2020). These components can be interpreted as layers or phases within the outflow. Reeves et al. (2018) unveiled a  $v_{\text{out}} \sim 0.46 \pm 0.02 c$  component in a 2017 observation with the X-ray satellite *NuSTAR* launched at only  $\sim 10 r_{\text{g}}$ , which is the fastest velocity UFO known to date. A results, which was confirmed by Boissay-Malaquin et al. (2019), with *Chandra*, *NuSTAR*, and *XMM-Newton* data.

PDS 456 is one of the few sources where evidence of an outflow has been found in both soft X-rays below 2 keV, and in Fe K absorption (see Reeves et al. 2020, and references therein), already in the initial detection by Reeves et al. (2003). With the *XMM-Newton* RGS, Reeves et al. (2016) detected multiple blue-shifted features around  $\sim 1 \text{ keV}$ , which they ascribe to L-shell iron, K-shell neon, and O VIII absorption. As for the Fe K absorption, the data indicate a multi-component wind. Variability on a timescale from weeks to month supports the conclusion, that this structure might correspond to overdense clumps or filaments, embedded a smooth, more highly ionised wind seen in the Fe K absorption. While Reeves et al. (2020) confirm that the soft absorption is more variable, they place it at parsec scales from the black hole, further away than the Fe K absorption, based on the fact that both  $N_{\text{H}}$  and  $\xi$  of the soft absorber are two orders of magnitude lower. The velocities they find are consistent with the Fe K absorber, in contrast to Reeves et al. (2016), who report  $v_{\text{out}} = 0.17\text{--}0.27$  for the fastest component, alongside two slower, less significant components. As the line broadening is different in both cases, it is not clear that the same region is probed in both cases, leaving room for the existence of a wind component moving at a lower velocity than the Fe K absorber. In general, a complete picture including both the hard and soft absorber is still to be determined (see Reeves et al. 2020, and references therein).

The soft absorption seems to be linked to obscuration, at last in part, as the spectrum is more featureless at higher fluxes (Reeves et al. 2016). In Matzeu et al. (2016), partial covering of the X-ray source by absorbing gas clouds is required to model the spectral energy distribution, i.e. the 1 eV–50 keV spectrum, but is not able to fully explain the observed variability. Consequentially, the variability in PDS 456 is likely a combination of intrinsic and absorption variability.

With a mass outflow rate of  $\sim 10 M_{\odot} \text{ yr}^{-1}$  and its wide opening angle, the UFO in PDS 456 possesses a power equivalent to  $\sim 20\%$  of the AGN’s bolometric luminosity, or half the Eddington rate (Nardini et al. 2015), which more than sufficient to drive feedback processes that significantly impact the quasar’s evolution (see Sect. 3.1).

### 3.3 Detecting UFOs with excess variance spectroscopy

Even though many UFO detections have been confirmed by different instruments and independent observations, as for PDS 456, the evidence is not always so clear and several effects can bias it. The 7–10 keV range, in which UFO lines reside, is at the upper end of the energy range covered by *XMM-Newton*, *Suzaku*, and *Chandra* and therefore subject to noise. In *XMM-Newton*’s EPIC-pn, contamination from the Cu K  $\alpha$  line in the instrumental background can lead to spurious detections and, in addition, the significance of detections can greatly depend on the continuum modelling (see Igo et al. 2020, and references therein). Considering that detections are more likely to be published than non-detections, these biases can significantly distort the general picture (Vaughan & Uttley 2008).

Excess variance spectroscopy offers an alternative approach to detect UFOs that was developed by Parker et al. (2017a, 2018). Essentially, the approach takes advantage of the increased variability of UFO lines, which appear as spikes in the excess variance spectrum. Enhanced excess variance in absorption lines can be generated by an anti-correlation between the line strength and the continuum: if the line strength decreases with increasing flux, the total flux change is higher in the line than in the continuum, causing the excess variance to spike. In the contrary case, the change in the line counteracts that in the continuum, resulting in an excess variance dip (Parker et al. 2018). Parker et al. (2017b) were the first to find such an anti-correlation in the highly variable AGN IRAS 13224–3809, before Parker et al. (2018) confirmed a similar behaviour for PDS 456. The anti-correlation can be explained by the absorption lines disappearing with rising X-ray flux, due to rising ionisation in the almost fully ionised environment (Parker et al. 2017b; Pinto et al. 2018; Parker et al. 2018; Igo et al. 2020). However, this picture might be incomplete. Fukumura et al. (2018) showed that such an anti-correlation can arise in a magnetohydrodynamically driven wind as well.

Igo et al. (2020) searched a sample of bright, variable AGN for UFOs with the excess variance approach described above, detecting outflows in  $\sim 30\text{--}60\%$  of sources, depending on whether cases of moderate evidence are counted. Their findings confirm that the anti-correlation discussed above holds in general and highlight the advantages of the approach: excess variance spectra are easy to calculate, show more pronounced features than count spectra, and provide less biased detections, in particular avoiding the issues related to Cu K  $\alpha$  contamination and continuum modelling discussed above. It should be noted, however, that the method can only be applied to variable sources.

## 3.4 Modelling excess variance spectra

Modelling presents a way to quantify UFO detections, by employing the fit statistics to judge how consistent the existence of the outflow is with the data. In addition, UFO parameters, such as the velocity, column density, or ionisation can be constrained by a model fit. The approach described in the following was introduced by Parker et al. (2020) and provides models for the variability of common spectral components of AGN, constructed on the basis of count spectral models. In contrast to previous ansatzes, these models are generally applicable and can be fit directly to variance spectra (see references in Parker et al. 2020).

### 3.4.1 The Monte Carlo modelling ansatz

The models are generated using a Monte Carlo ansatz and take the form of table models, i.e., specific model values are calculated on a parameter grid and interpolated for model evaluation. The models are multiplicative and calculated relative to an underlying variable powerlaw<sup>1</sup>, as AGN generally show a baseline red noise variability (see Sect. 1.2.1). For each grid point, 1000 spectra are simulated using XSPEC 12.11.0m (Arnaud 1996). The procedure is shown in Fig. 3.1. In each spectrum, the flux,  $F$ , is varied by drawing values for  $\log F$  from a normal distribution with a fixed variance of 0.2. To simulate the response of a number of other parameters,  $i$ , to the flux change, they are linearly correlated to the flux via parameters  $C_i$ . Then,  $F_{\text{var}}$  is calculated as described in Sect. 2.4.

In addition to the baseline powerlaw model, FVAR\_POW, Parker et al. (2020) generated the following models. For a brief introduction of the corresponding AGN spectral features see Sect. 1.2.1.

- FVAR\_BBDAMP accounts for the variability dampening due to the soft X-ray excess commonly observed in AGN, by phenomenologically modelling it as a black body.
- FVAR\_REFDAMP and FVAR\_XILDAMP model reflection variability, i.e., variability in the spectrum reflected off of the accretion disc.
- FVAR\_UFO models the outflow variability and is introduced in more detail in the following section.

When applied to the highly variable AGN IRAS 13224–3809, a model constructed from these components provided a good fit result and quantified UFO parameters in agreement with results from conventional spectroscopy. Parker et al. (2020) evaluated the accuracy of the approach with analytical calculations. For a detailed description of the models and their parameters, see Parker et al. (2020).

---

<sup>1</sup>Spectral models require at least one additive component, which returns absolute values that can be modified by multiplicative components. In the evaluation of the  $F_{\text{var}}$  models discussed here, the underlying powerlaw variability serves as the additive component.

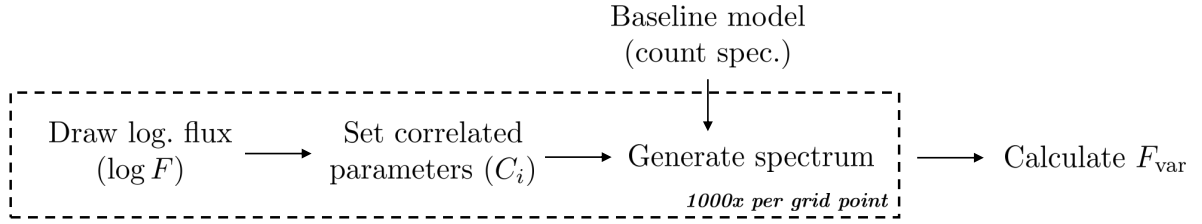


Figure 3.1: An illustration of the  $F_{\text{var}}$  Monte Carlo based table model generation process following Parker et al. (2020). For a detailed description see the text.

### 3.4.2 Improving upon the UFO model

As detailed in Sect. 3.3, the increased variability of UFO lines can be ascribed to the response of the ionisation,  $\xi$ , to the continuum flux,  $F$ . The UFO model accounts for this response by correlating  $\log \xi$  to  $\log F$  via a multiplicative factor  $C_{\text{UFO}}$ . In addition, the model accounts for the column density,  $N_{\text{H}}$ , of the outflowing gas. The model is based on the XABS count spectral model (Steenbrugge et al. 2003) from SPEX (Kaastra et al. 1996).

The Fe XXVI Ly  $\alpha$  UFO line visible in the  $F_{\text{var}}$  spectrum of PDS 456 is much broader than the corresponding feature for IRAS 13224–3809 (Parker et al. 2018; Igo et al. 2020). One potential reason for this broadening is the increase of outflow velocity with X-ray luminosity identified by Matzeu et al. (2017), see Sect. 3.2. The aim of this part I of my thesis is to improve upon the UFO model by accounting for the broadening and to model the  $F_{\text{var}}$  spectrum of PDS 456. To this end, I adapted the implementation and routines to generate the model that were provided by Michael L. Parker, Zsofi Igo, and Amy Jocyce.

To account for the broadening, an additional correlation is introduced between the outflow velocity and  $\log F$  (velocity trend hereafter), with a corresponding parameter  $C_v$ . In practice, the UFO lines shift as the outflow velocity changes, leading to an increase in variability around their mean positions. For practical reasons, I implement the outflow velocity in terms of the redshift parameter,  $z$ . Figure 3.2 shows the model spectrum for three different correlation strengths, given in terms  $C_v$ . An increase in  $C_v$  clearly broadens the absorption spikes. This broadening results from the shift in the UFO line positions caused by the velocity trend, as explained above.

In addition, the shape of the spike changes as well, as Fig. 3.3 shows. The maximum is slightly redshifted compared to the mean absorption line energy in the count spectrum, due to a dip at the high-energy side of the line. This dip appears because the relative change in count rate is lower if the line is maximally blueshifted. For high blueshift, the count rate is above average, due to the velocity trend. In this case, the drop caused by an absorption line brings it closer to average (see blue and black lines in Fig. 3.3), decreasing the variance. Note that the strength of the dip depends on  $C_v$ , because a higher  $C_v$  leads to lines which are broader but not as deep, which counteracts the effect. In addition, the strength of the dip depends on the distribution of line energies and on the variation of line shape with flux. In the example in Fig. 3.3, the line energies are

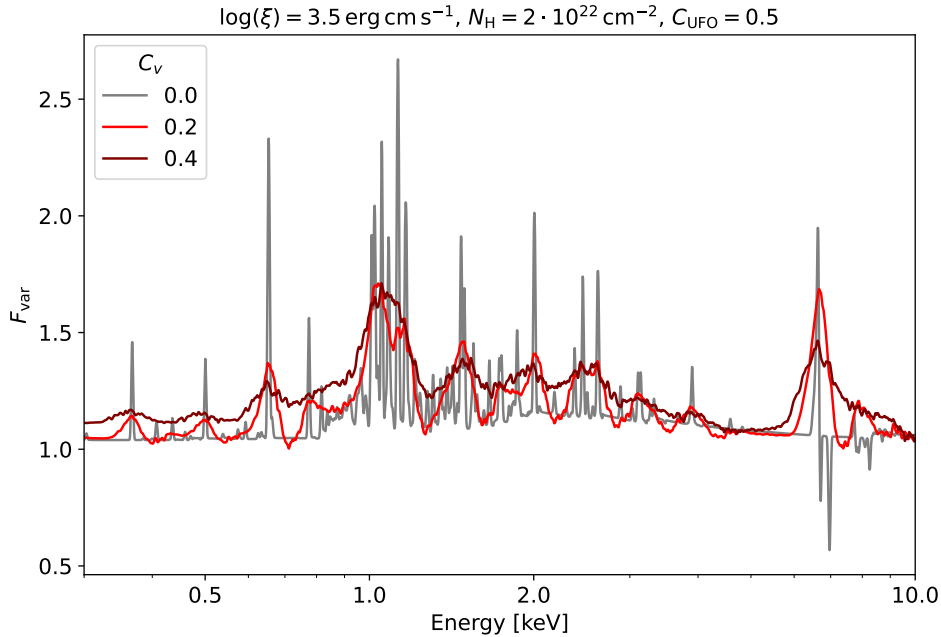


Figure 3.2: The  $F_{\text{var}}$  spectrum as predicted by the improved UFO model, which includes a correlation between the outflow velocity and the logarithm of the flux (Härer et al. 2021, Fig. 1, adapted). Three different values of the correlation parameter,  $C_v$ , are given. The correlation causes a broadening of the UFO absorption spikes.

normally distributed and the line broadness and depth are constant. Also note that in Fig. 3.2, the dips are not always clearly visible because spikes blend into each other. There is also an additional mechanism that can lead to dips in the variance spectrum. As the ionisation increases, more and more of the Fe XXV ions lose an electron, i.e., the abundances are redistributed towards Fe XXVI. The increase in the abundance of Fe XXVI counteracts the overall decrease of line strength and decreases the variability at the high end of the Fe K  $\alpha$  line, because the Ly  $\alpha$  line is at a slightly higher energy in Fe XXVI.

As a second improvement to the  $F_{\text{var}}$  UFO model besides the introduction of a velocity trend, I take into account the intrinsic velocity of the gas surrounding the AGN,  $v_{\text{int}}$ . In count spectra,  $v_{\text{int}}$  results in a Doppler broadening of the absorption lines. Figure 3.4 shows the effect of this broadening on the model. As explained in Sect. 3.3, the  $F_{\text{var}}$  absorption spikes are assumed to be due to the change of line depth with ionisation. Introducing line broadening in the count spectrum increases the energy range around the centre of the line where this effect plays a role and therefore also broadens the spikes.

In summary, both a velocity trend and  $v_{\text{int}}$  cause a broadening of the absorption spikes in  $F_{\text{var}}$  spectra. I have therefore created two versions of the model: `fvar_ufo.fits`, which takes into account only a velocity trend, and `fvar_ufo_vint.fits` with an additional fixed  $v_{\text{int}} = 10^4 \text{ km s}^{-1}$ . This value is motivated by Matzeu et al. (2016) and Reeves et al. (2016), who both find  $v_{\text{int}} \sim 10^4 \text{ km s}^{-1}$ . I use both models in the analysis of PDS 456

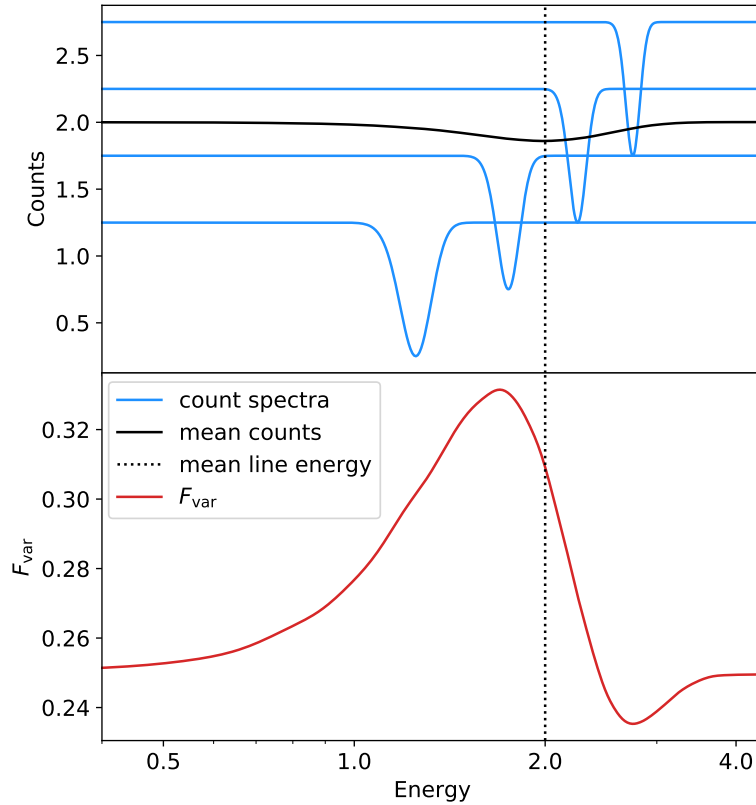


Figure 3.3: The shape of a spike in the  $F_{\text{var}}$  spectrum resulting from a correlation of the absorption line energy and the number of counts, as, e.g., given by the velocity trend in PDS 456 (Härer et al. 2021, Fig. 2). The spike peaks slightly below the mean line energy (*dotted line*) in the count spectrum, because the spectra with high count rate cause a dip in variance at the high-energy side of the line. For this example, 10000 spectra with a single Gaussian absorption line of fixed variance of 0.1 and depth of 1 were generated (*blue*). The number of counts was drawn from a normal distribution with mean 2 and variance 0.5 and correlated to the number of counts with a factor of 1. From these spectra, the mean number of counts (*black*) and  $F_{\text{var}}$  (*red*) were calculated. The dotted line indicates the mean line energy. All units are arbitrary.

and discuss their physical implications and differences in the following sections.

### 3.5 Fitting the excess variance spectrum of PDS 456

All available archival *XMM-Newton* observations of PDS 456 were included in the analysis, i.e., all data listed in Igo et al. (2020) and three additional observations taken in 2018 and 2019 (obsIDs 0830390101, 0830390201, and 0830390401; Reeves et al. 2020), resulting in a total exposure of 890 ks. The data reduction and calculation of the  $F_{\text{var}}$  spectra were done by Zsofi Igo and Michael L. Parker, following the procedure stated in Igo

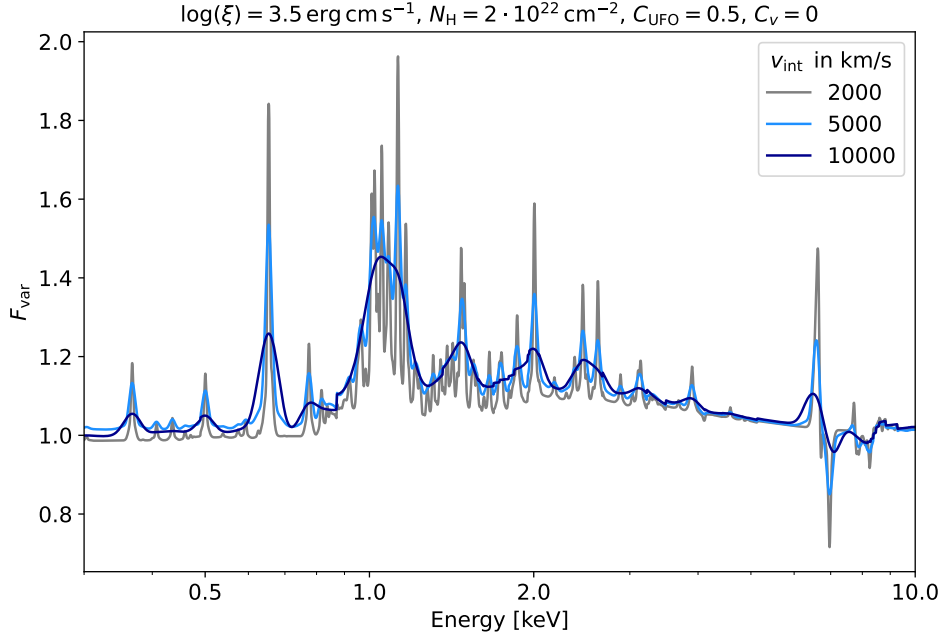


Figure 3.4: The  $F_{\text{var}}$  spectrum for the second version of the improved UFO model, which includes Doppler broadening due to the movement of the gas with a velocity  $v_{\text{int}}$  (Härer et al. 2021, Fig. 3, adapted). A higher  $v_{\text{int}}$  results in a smoothing and broadening of the spikes.

et al. (2020), with specifications detailed in Härer et al. (2021). The  $F_{\text{var}}$  spectrum was calculated using a 10000 s time binning.

Fitting  $F_{\text{var}}$  spectra differs in some respects from fitting count spectra. The general considerations are laid out by Parker et al. (2020). To account for the resolution of *XMM-Newton*'s EPIC-pn, the model is smoothed by an energy-dependent Gaussian (GSMOOTH in XSPEC) with a standard deviation of 0.1 keV at 6 keV and an energy dependence index of 0.165. A 1% systematic error was added to avoid overprecise fitting at low energies at the expense of accuracy at higher energies, which is necessary because the  $F_{\text{var}}$  models are not yet as precise as count spectral models and the uncertainty of  $F_{\text{var}}$  is significantly greater at higher energies.

### 3.5.1 Fitting spectra of PDS 456

The  $F_{\text{var}}$  spectrum of PDS 456 is flat above  $\sim 1$  keV, with some variation around the mean and two clear spikes just below and above 10 keV (see Fig. 3.5). At low energies, the variability is damped. First, a continuum model is constructed for this spectrum out of the components introduced in Sect. 3.4. The continuum model includes two phenomenological components, a powerlaw (FVAR\_POW) and soft excess damping modelled as a blackbody (FVAR\_BBDAMP), and relativistic reflection (FVAR\_REFDAMP). Second, the UFO model is added, which includes the improvements discussed in Sect. 3.4.2. Note that any constant multiplicative components, such as galactic absorption, can be ignored due to

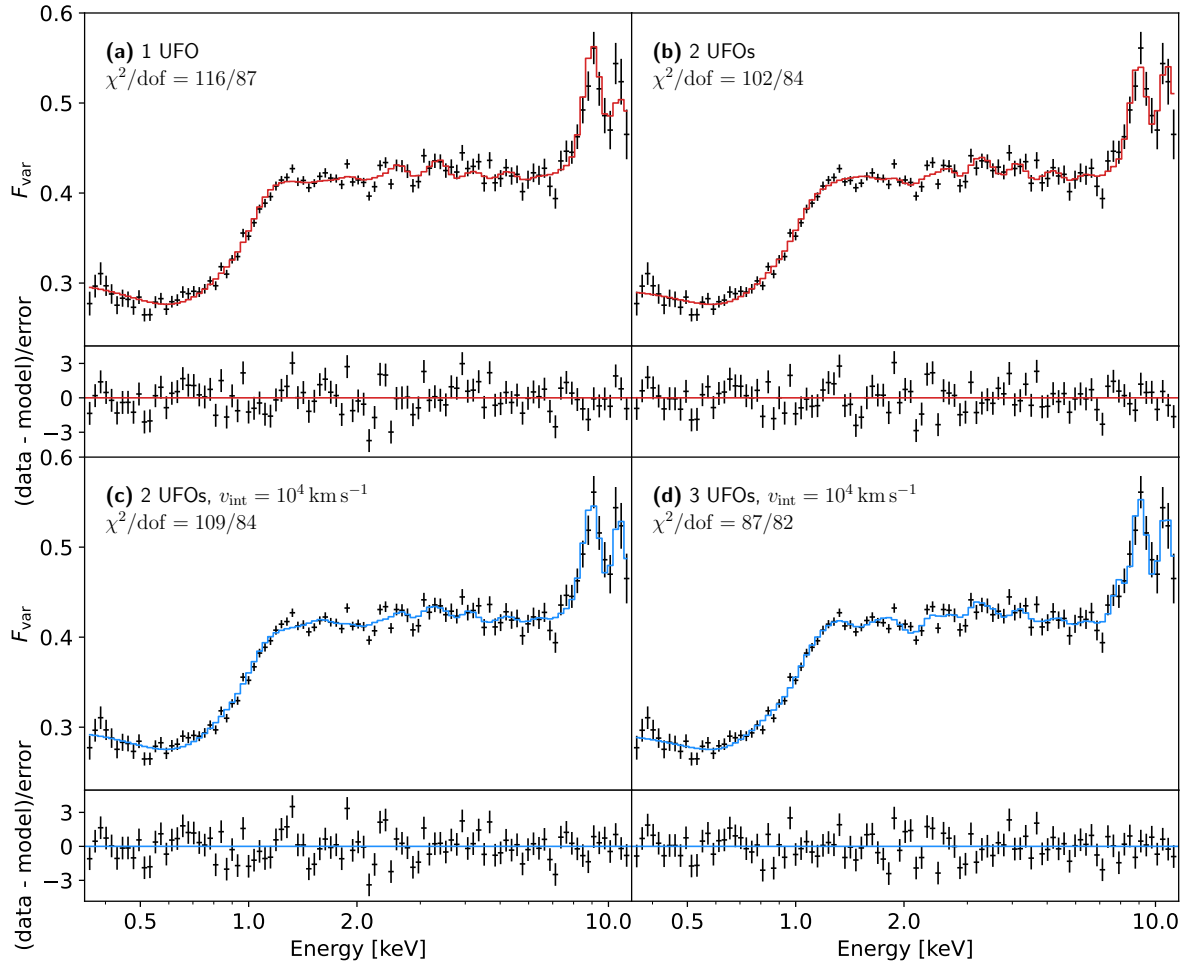


Figure 3.5: The  $F_{\text{var}}$  spectrum of PDS 456, modelled following Parker et al. (2020), with improvements to the UFO component to account for broadening of the UFO absorption spikes (Härer et al. 2021, Fig. 4, adapted). To this end, we introduced a correlation between the outflow velocity and the logarithm of the flux and line broadening due to the intrinsic gas velocity,  $v_{\text{int}}$ . Models (a) and (b) only include the first effect (*red*), while (c) and (d) assume an additional  $v_{\text{int}} = 10^4 \text{ km s}^{-1}$  (*blue*). One, two, and three outflowing layers are considered, in (a), (b) and (c), and (d) respectively. The continuum model includes power law variability, black body soft excess, as well as relativistic reflection. A systematic error of 0.01 was added. The energy is given in the reference frame of the source.

the fractional nature of  $F_{\text{var}}$  spectral models.

I start by considering a single UFO component without intrinsic Doppler broadening (`fvar_ufo.fits`). The result is shown in Fig. 3.5 (a). Overall, the model provides a good description of the data ( $\chi^2/\text{dof} = 116/87$ ), keeping in mind that  $F_{\text{var}}$  spectral models are crude compared to count spectral models. The broadened Fe  $K\alpha$  absorption spike is

well accounted for by the improved UFO model, but the second spike is underestimated and some of the features between 1–3 keV are missed. The parameters of all fits are summarised in Table 3.1.

As discussed in the Sect. 3.2, there is evidence that the UFO in PDS 456 consists of two or more layers with differences in outflow velocity and ionisation. The second spike could therefore result from Fe XXVI Ly  $\alpha$  absorption, as the first one, but from a layer with a higher outflow velocity, i.e., larger blueshift. This interpretation is supported by the fact that both spikes have a similar intensity, which is hard to explain from a single velocity component, because Fe XXVI Ly  $\alpha$  is expected to stand out clearly as the strongest line. I therefore add a second UFO component to the model, tying the  $C_{\text{UFO}}$  and  $C_v$  parameters between components to reduce the number of free parameters. Adding a second UFO component does indeed significantly improve the fit ( $\chi^2/\text{d.o.f.} = 102/84$ ) and better account for the second spike (see Fig. 3.5; b). However, the residuals in the 1–3 keV range remain largely the same.

Adding a further UFO component did neither decrease these residuals, nor improve the fit statistics. Therefore, I follow the second ansatz introduced in Sect. 3.4.2, to take into account line broadening due to the intrinsic velocity of the gas surrounding the AGN. Following estimates by Matzeu et al. (2017) and Reeves et al. (2016), a fixed  $v_{\text{int}} = 10^4 \text{ km s}^{-1}$  was chosen, which causes the broadening to be significant (see Fig. 3.4), i.e., the value is well suited to investigate the influence of  $v_{\text{int}}$  on the UFO model.

The results are shown in Fig. 3.5 (c). The fit is similar in quality to the one without intrinsic velocity broadening and there is no improvement in the 1–3 keV residuals. Most of the fit parameters (see Table 3.1) are equivalent within their error ranges, but the parameter which correlates the outflow velocity to the logarithm of the flux,  $C_v$ , is smaller. The smaller value is expected, as the velocity trend does not need to account for all the broadening which is observed, because  $v_{\text{int}}$  is included in the model.

To investigate the capabilities of the model with  $v_{\text{int}}$  further, a third component is added (Fig. 3.5; d). As before, the correlation parameters  $C_{\text{UFO}}$  and  $C_v$  were tied between components. In contrast to the previous result without intrinsic broadening, the additional third layer yields a very good fit ( $\chi^2/\text{dof} = 87/82$ ), which can be attributed to the fact that more of the features in the 1–3 keV range are now modelled correctly. However, this fit has a  $C_v$  of the order of  $10^{-8}$ , i.e., the velocity trend is formally not required and all the broadening is due to intrinsic velocity broadening. In summary, both a velocity trend and intrinsic velocity broadening are independently able to account for the broadening of the absorption spikes, with a noticeable difference in the fit with three components. A detailed comparison of both effects will follow in Sect. 3.6.2.

In general, it is difficult to constrain physical parameters given the current accuracy of the  $F_{\text{var}}$  spectral models, i.e., errors are large and often only a lower or upper bound can be obtained. Over all fits discussed above, the outflow velocity is 0.27–0.30  $c$  for the first and 0.41–0.49  $c$  for the second component. The third component in the last fit has a velocity of 0.15–0.20  $c$ . These values agree well with previous studies (e.g., Reeves et al. 2018; Matzeu et al. 2017; Boissay-Malaquin et al. 2019; Reeves et al. 2020). All parameter ranges given here and in the following are for a confidence level (CL) of 90%.

In the models without intrinsic velocity broadening,  $C_v$  was found to be in the range

0.25–0.28, which is a stronger correlation than reported by Matzeu et al. (2017), as shown in Fig. 3.7 and discussed in detail in Sect. 3.6.2. If  $v_{\text{int}} = 10^4 \text{ km s}^{-1}$  is included,  $C_v$  goes down to  $0.22_{-0.08}^{+0.07}$ , which means that the lower bound is consistent with Matzeu et al. (2017). For three layers and  $v_{\text{int}} = 10^4 \text{ km s}^{-1}$ , the velocity trend is formally not required because  $C_v$  is very small. The implications of these results will be discussed further in Sect. 3.6.2.

### 3.5.2 Revisiting IRAS 13224–3809

IRAS 13224–3809 is extremely variable on timescales as short as hours and therefore well suited to perform variability studies (e.g., Parker et al. 2017b; Alston et al. 2019). Here, the improved UFO model is included in the model of IRAS 13224–3809 introduced by Parker et al. (2020). All details concerning the data and modelling can be found in Parker et al. (2020).

I exclude all data below 3 keV, as the goal is to investigate the shape of the Fe Ly  $\alpha$  UFO spike. Therefore, it is sufficient to use the FVAR\_POW model for the continuum, i.e., to ignore blackbody damping and relativistic reflection. As for PDS 456, a systematic error of 1% was included in the analysis. Only broadening due to the correlation between outflow velocity and logarithm of the flux is considered, not intrinsic Doppler broadening.

The fit result is shown in Fig. 3.6 and Table 3.2. The spike shape is described well by the model. The parameters are generally consistent with the ones found by Parker et al. (2020). An upper bound of 0.02 on  $C_v$  is found, which suggests that the velocity trend is significantly smaller than for PDS 456, which is  $C_v = 0.25\text{--}0.28$  in the model equivalent to the one used here, i.e., without intrinsic Doppler broadening. The smaller value is to be expected, as the spike in the  $F_{\text{var}}$  spectrum is noticeably narrower than for PDS 456.

There is evidence for a small velocity trend in the literature (Pinto et al. 2018; Chartas & Canas 2018). However, the precise strength is hard to determine, due to the strong variability of IRAS 13224–3809. In addition, the observed broadening does not necessarily originate from a velocity trend, but can also arise from other effects, e.g., intrinsic velocity broadening. Therefore, only upper bounds can be inferred from fitting models that account for a single effect. In the count spectrum, distinguishing line broadening and shift due to a velocity trend is easier. It is therefore promising to perform a joined analysis of  $F_{\text{var}}$  and count spectra in order to disentangle the different contributions.

Table 3.1: Fit parameters for PDS 456 resulting from the four different models shown in Fig. 3.5. Further description of the FVAR\_UFO component and its parameters can be found in the text. The continuum is described by a powerlaw component, FVAR\_POW, blackbody soft excess, FVAR\_BBDAMP, and relativistic reflection, FVAR\_REFDAMP, from Parker et al. (2020), see Sect. 3.4. The powerlaw parameters Var and  $C_\Gamma$  describe the variance of the flux in log space and its correlation to the photon index, respectively. This correlation is very weak throughout the models, which is representative of the flat continuum variance.  $C_{\text{ref}}$  correlates the flux of the reflection component to the powerlaw flux. Where the logarithm of a quantity is given, the unit refers to the quantity itself and not its logarithm.

Component	Parameter	1 UFO	2 UFOs	2 UFOs, $v_{\text{int}} = 10^4 \text{ km s}^{-1}$	3 UFOs, $v_{\text{int}} = 10^4 \text{ km s}^{-1}$	Unit
FVAR_POW	Var	$0.34^{+0.02}_{-0.03}$	$0.34^{+0.04}_{-0.03}$	$0.35^{+0.02}_{-0.03}$	$0.31^{+0.04}_{-0.03}$	
	$C_\Gamma$	$\ll 0.01$	$\ll 0.01$	$\ll 0.01$	$\ll 0.01$	
FVAR_BBDAMP	kT	$0.31^{+0.01}_{-0.02}$	$0.32 \pm 0.02$	$0.32 \pm 0.02$	$0.31 \pm 0.02$	keV
	$f_{\text{BB}}$	$0.20 \pm 0.03$	$0.18^{+0.04}_{-0.03}$	$0.20 \pm 0.03$	$\geq 0.15$	
FVAR_REFDAMP	$\log(n)$	$\geq 18.9$	$\geq 18.8$	$\geq 18.8$	$\geq 18.4$	$\text{cm}^{-3}$
	$\log(\xi)$	$\leq 1.02$	$\leq 1.09$	$\leq 1.08$	$\leq 1.1$	$\text{erg cm s}^{-1}$
	$f_{\text{ref}}$	$\geq 4.4$	$\geq 3$	$\geq 4.4$	$\geq 3$	
	$C_{\text{ref}}$	$0.47^{+0.04}_{-0.03}$	$0.49 \pm 0.05$	$0.47 \pm 0.04$	$0.56^{+0.10}_{-0.07}$	
FVAR_UFO (1)	$\log(\xi)$	$4.5^{+0.1}_{-0.2}$	$4.10^{+0.08}_{-0.12}$	$4.1^{+0.2}_{-0.1}$	$4.19^{+0.3}_{-0.5}$	$\text{erg cm s}^{-1}$
	$N_{\text{H}}$	$8.1^{+0.2}_{-0.3}$	$1.7^{+0.6}_{-0.4}$	$2.00^{+0.13}_{-0.06}$	$\leq 5.5$	$10^{23} \text{ cm}^{-2}$
	$C_{\text{UFO}}$	$\geq 0.7$	$\geq 0.94$	$\geq 0.4$	$0.49^{+0.08}_{-0.28}$	
	$C_v$	$0.27^{+0.09}_{-0.04}$	$0.26^{+0.02}_{-0.05}$	$0.22^{+0.07}_{-0.08}$	$\ll 0.01$	
	$v$	$-0.28 \pm 0.01$	$-0.28 \pm 0.01$	$-0.29 \pm 0.01$	$-0.28 \pm 0.01$	$c$
FVAR_UFO (2)	$\log(\xi)$		$4.1^{+0.3}_{-0.1}$	$4.2^{+0.4}_{-0.1}$	$4.0^{+0.1}_{-0.2}$	$\text{erg cm s}^{-1}$
	$N_{\text{H}}$		$\leq 1.4$	$\leq 4$	$\leq 2.4$	$10^{23} \text{ cm}^{-2}$
	$v$		$-0.45^{+0.04}_{-0.02}$	$-0.43 \pm 0.02$	$-0.43 \pm 0.02$	$c$
FVAR_UFO (3)	$\log(\xi)$				$3.77^{+0.20}_{-0.04}$	$\text{erg cm s}^{-1}$
	$N_{\text{H}}$				$\leq 1.9$	$10^{22} \text{ cm}^{-2}$
	$v$				$-0.17^{+0.03}_{-0.02}$	$c$

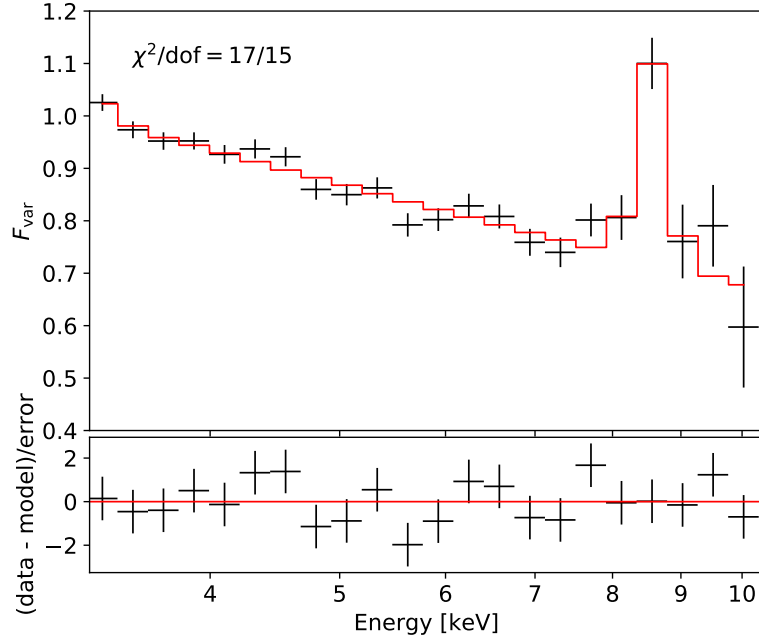


Figure 3.6:  $F_{\text{var}}$  spectrum of IRAS 13224–3809 fitted with the improved UFO model (Härer et al. 2021, Fig. 5), which accounts for broadening of the absorption spike by introducing a correlation between the outflow velocity and the logarithm of the flux (velocity trend). A 1% systematic error was added. The fit has a similar quality as the previous model by Parker et al. (2020) and places an upper limit of 0.02 on the correlation parameter  $C_v$ , which indicates that the velocity trend in IRAS 13224–3809 is weak and not significant for understanding the  $F_{\text{var}}$  spectrum. The energy is given in the reference frame of the source.

## 3.6 Discussion

The results have shown that the  $F_{\text{var}}$  spectrum of the luminous radio-quiet quasar PDS 456 is described well by the  $F_{\text{var}}$  spectral models from Parker et al. (2020), with improvements to the UFO component accounting for the observed broadening of the spikes in the  $F_{\text{var}}$  spectrum. Two effects were implemented to achieve this: a correlation between the outflow velocity and the logarithm of the X-ray flux via a parameter  $C_v$ , motivated by the discovery of such a velocity trend by Matzeu et al. (2017), and intrinsic Doppler broadening with a velocity  $v_{\text{int}}$ .

### 3.6.1 The multi-layered structure of the UFO

A single outflowing layer does not account for the similar height of the two prominent spikes in the  $F_{\text{var}}$  spectrum of PDS 456. Adding a second layer provides a satisfying result and significantly improves the fit quality, which we interpret as clear evidence that a second layer is present. This is the first time that strong evidence for a second

Table 3.2: Fit parameters for IRAS 13224–3809 obtained from modelling the 3–10 keV range of the  $F_{\text{var}}$  spectrum with the version of the improved UFO model, which excludes intrinsic velocity broadening (see Sect. 3.4.2). For this energy range, only the components FVAR\_UFO and FVAR\_POW need to be taken into account, as damping in the soft band is not important above 3 keV. Where the logarithm of a quantity is given, the unit refers to the quantity itself and not its logarithm.

Component	Parameter	Value	Unit
FVAR_POW	Var	$0.44^{+0.02}_{-0.05}$	
	$C_{\Gamma}$	$0.49^{+0.05}_{-0.06}$	
FVAR_UFO	$\log(\xi)$	$4.1^{+0.6}_{-0.5}$	erg cm s <sup>-1</sup>
	$N_{\text{H}}$	$\geq 10^{23}$	cm <sup>-2</sup>
	$C_{\text{UFO}}$	$0.013^{+0.04}_{-0.006}$	
	$C_v$	$\leq 0.02$	
	$v$	$-0.23^{+0.02}_{-0.01}$	$c$

outflowing layer has been found in EPIC-pn data alone, which speaks for the sensitivity of the method. Previous evidence for a second layer in PDS 456 was provided by a joint analysis of *NuSTAR*, *XMM-Newton* (Reeves et al. 2018), and *Chandra* data (Boissay-Malaquin et al. 2019), see Sect. 3.2. Their measured outflow velocities of  $0.46 \pm 0.02 c$  and  $0.48 c$ , respectively, are well within the range of our results (0.41–0.49  $c$ ).

A further significant improvement to the fit can be made by adding a third layer in the case where  $v_{\text{int}} = 10^4 \text{ km s}^{-1}$ . However, the excellent quality of  $\chi^2/\text{dof} = 87/82$  is mostly because the features in the 1–3 keV range are described better, not the spikes, which are crucial to UFO detection in our approach. As this is a very good fit nonetheless, this results can be interpreted as moderate evidence for a third layer. As discussed in Sect. 3.2, Reeves et al. (2016) found a low ionisation component of the wind at  $\sim 0.2 c$  in their analysis of data from RGS taken in 2013–2014, by fitting absorption lines of H- and He-like neon and L-shell iron below 2 keV. These results go well with our proposed third layer, i.e., the improved description in the 1–3 keV band and the slightly lower ionisation ( $3.77^{+0.20}_{-0.04}$ ) as compared to  $4.19^{+0.3}_{-0.5}$  and  $4.0^{+0.1}_{-0.1}$  for the first and second layer. The presence of line broadening in the count spectrum with  $v_{\text{int}} \sim 10^4 \text{ km s}^{-1}$  is well established for the first layer (0.27–0.30  $c$ ) in the Fe K band (e.g., Matzeu et al. 2017; Reeves et al. 2020) and the value is likely a valid approximation for the second (0.41–0.49  $c$ ) and possible third (0.15–0.20  $c$ ) layer for the purposes of our analysis (e.g., Reeves et al. 2016, 2020). Considering the good fit result, it is therefore plausible that intrinsic Doppler broadening in the count spectrum contributes noticeably to spike broadening in the  $F_{\text{var}}$  spectrum in PDS 456. However, an intrinsic velocity is unlikely to be responsible for all broadening, as a velocity trend is known to exist in PDS 456 (Matzeu et al. 2017) and we have shown that such a trend causes broadening as well.

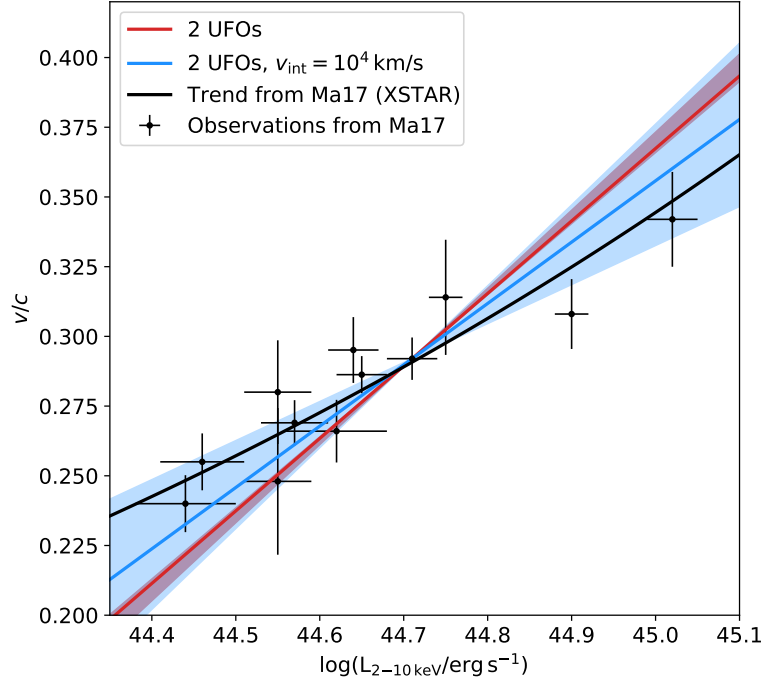


Figure 3.7: Measured relation (*black points and regression line*) between the outflow velocity and the 2–10 keV luminosity of PDS 456 from Matzeu et al. (2017) (Ma17 here), compared to the relations obtained from fitting the improved UFO model (*red and blue*) to the  $F_{\text{var}}$  spectrum (Härer et al. 2021, Fig. 6). The two models considered here assume two outflowing layers. One model includes line broadening due the intrinsic velocity of the gas (*blue*) and one does not (*red*), as in Fig. 3.5 (b) and (c). The slope of the lines is given by the correlation parameters  $C_v$  for these fits, with their 90% CL shaded. The  $y$  offsets were chosen arbitrarily to allow for a by-eye comparison to the trend from Ma17. One sigma error bars are shown for the observations.

In summary, the results are in agreement with the existing multi-layer picture of the UFO in PDS 456. That is, fast, highly ionized winds are launched close to the black hole, and are accompanied by a slower, possibly clumpy layer with low ionisation further out. In addition, the method is able to provide evidence for multiple layers in a single analysis, because additional UFO components can be easily added to the fit, which is an advantage over count spectra analysis and helps piece together a unified picture. Fitting  $F_{\text{var}}$  spectra is therefore a promising approach to study the wind structure in PDS 456 and similar AGN. To allow for a more quantitative analysis, the next step is to improve the accuracy of the model. Accurate  $F_{\text{var}}$  models are of special interest regarding future microcalorimetry missions such as *XRISM* and *Athena*, which will provide X-ray spectroscopy data of unprecedented resolution, that is especially valuable in detecting UFO absorption in the soft band.

### 3.6.2 Determining the cause of the spike broadening

The broadening of the UFO spikes can be modelled equally well by a velocity trend and intrinsic velocity broadening, which begs the question of how their individual contributions can be disentangled. Figure 3.7 compares  $C_v$  to the velocity trend found by Matzeu et al. (2017), for fits with and without velocity broadening. It can be seen that the fit without  $v_{\text{int}}$  most likely overestimates the trend and does not agree well with the data, while the case of  $v_{\text{int}} = 10^4 \text{ km s}^{-1}$  is consistent with the lower limit of the range. In conclusion,  $v_{\text{int}}$  contributes to the spike broadening in PDS 456 and  $C_v$  can only be interpreted as an upper limit on the strength of the velocity trend if  $v_{\text{int}}$  is ignored.

As already mentioned in 3.5.2, separating both effects from  $F_{\text{var}}$  spectra alone is difficult. Performing an additional count spectral analysis is a promising approach to solve this problem, because line broadening and shift due to a velocity trend can be more clearly distinguished in count spectra. However, for more rapidly variable sources like IRAS 13224–3809, a count spectrum with sufficient signal to detect the UFO lines will integrate over a wide range of fluxes and hence broadening will be introduced as a result of the velocity trend, i.e., the line shift with changing flux. In this case, a flux-resolved analysis is likely the most effective way of identifying the strength of the velocity trend (see Pinto et al. 2018).

## 3.7 Summary

UFO absorption manifests itself through spike-like features in the  $F_{\text{var}}$  spectrum. I introduce improvements to a UFO  $F_{\text{var}}$  model by Parker et al. (2020), by accounting for two effects that could cause the UFO spikes in the  $F_{\text{var}}$  spectrum of PDS 456 to broaden: first, a correlation between the outflow velocity and the logarithm of the X-ray flux and second, intrinsic Doppler broadening. Both effects are able to describe the broadened spikes in PDS 456 equally well. I find clear evidence for two outflowing layers and possible indication of a third one. This is the first time a fast layer (0.41–0.49  $c$ ) has been seen in *XMM-Newton* EPIC-pn data alone, which highlights the potential of using  $F_{\text{var}}$  spectral models to detect UFOs and investigate the wind structure. The results agree very well with the existing notion of a multi-layered UFO in PDS 456 and with previous measurements of the outflow velocities. If intrinsic Doppler broadening is excluded, the value for the strength of the correlation between the outflow velocity and the logarithm of the X-ray flux is overestimated, suggesting that Doppler broadening is needed and if excluding it, the correlation strength has to be interpreted as an upper limit. I briefly discuss IRAS 13224–3809 and find that its upper limit on the correlation strength is smaller than for PDS 456, as expected from the narrower spike in its  $F_{\text{var}}$  spectrum.



# 4 Part II: stellar wind variability in Cyg X-1 at high spectral resolution

In this chapter, I present a study of the stellar wind structure in the high-mass X-ray binary Cygnus X-1 (Cyg X-1) with excess variance spectra. Notable is the high resolution of the *Chandra* gratings spectra, which makes it possible to compare variability in absorption lines from different ion species. The analysis is complemented by a comparison to column density variations expected from a clumpy stellar wind model. The research introduced in this chapter is part of a manuscript to be submitted to *Astronomy and Astrophysics* (Härer et al. 2021b). This chapter is largely taken verbatim from the publication.

## 4.1 Probing stellar winds of supermassive stars

O and B stars live a short, but very luminous life. Their high masses lead to high core pressures and temperatures. As stars are optically thick, they emit blackbody radiation according to their temperature: following the Stefan-Boltzmann and Wien's displacement laws<sup>1</sup>, O and B stars reach high luminosities that peak in the UV ( $T_{\text{surface}} \sim 3\text{--}5 \cdot 10^5$  K; see Seward & Charles 2010, Ch. 7). The high UV luminosity gives rise to strong winds, which are driven by resonant line absorption in metal ions, such as C, N, and Si (Lucy & Solomon 1970; Castor et al. 1975). With mass-loss rates of  $\sim 10^{-6} M_{\odot} \text{ yr}^{-1}$  and terminal velocities of  $\sim 2000 \text{ km s}^{-1}$  these winds can strongly impact stellar evolution and sweep up material of the interstellar medium. This mechanical feedback adds to the radiative and chemical feedback from massive stars, which shapes the galaxy today and was likely crucial in the early universe (see Puls et al. 2008; Martínez-Núñez et al. 2017; Seward & Charles 2010, Ch. 7).

It is well established that stellar winds of massive stars are highly inhomogeneous flows (Hamann et al. 2008; Sundqvist et al. 2012; Puls et al. 2015). The inhomogeneities can be understood as overdense clumps, embedded in a tenuous flow. The most likely mechanism behind the formation of these structures is an instability inherent to line driving (Owocki & Rybicki 1984; Owocki et al. 1988; Sundqvist et al. 2018). Due to wind clumping, mass-loss rates are likely to be overestimated by a factor of  $\sim 2\text{--}10$ , with potentially far-reaching consequences for stellar evolution models (Fullerton et al. 2006; Sundqvist & Puls 2018; see also Puls et al. 2008). The uncertainty on the estimate is large, because fundamental clump properties still need to be constrained, such as typical

---

<sup>1</sup>The Stefan-Boltzmann law,  $L = A\sigma T^4$ , gives the luminosity of an object,  $L$ , that radiates blackbody radiation at a temperature  $T$  over surface area  $A$ .  $\sigma$  is the Stefan-Boltzmann constant. Wien's displacement law states that the radiation peaks at  $\lambda_{\text{peak}} = bT^{-1}$ , with Wien's constant,  $b$ .

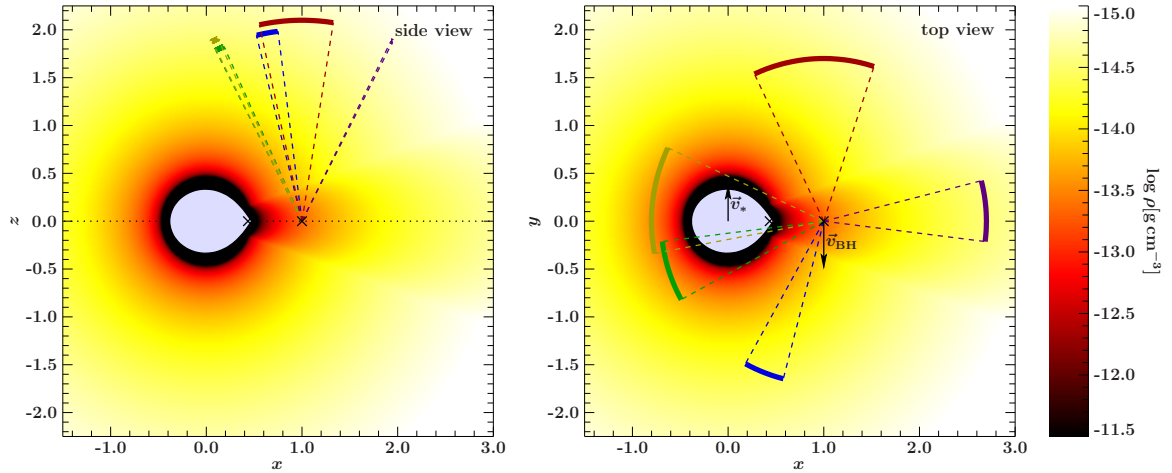


Figure 4.1: Miškovičová et al. (2016), Fig. 7: Stellar wind density in Cyg X-1, according to the focused wind model by Gies & Bolton (1986). Light green and dark purple indicate the orbital phases covered by the superior (Obs. 3814) and inferior (Obs. 11044) conjunctions, respectively. The direction of rotation is indicated with arrows in the right-hand panel.

shapes and masses. It is also unclear how the clumps evolve as they move outwards and how clumping interferes with the efficiency of the driving mechanism (see Puls et al. 2008).

High mass X-ray binaries (HMXBs) present an opportunity to study winds of massive stars by measuring their X-ray absorption (for a review see Martínez-Núñez et al. 2017). Spectroscopy can provide environmental characteristics, such as densities, ionisations, and element abundances. The wind structure can be constrained from the variability of the column density (absorption variability; e.g., Oskinova et al. 2012; Grinberg et al. 2015). In particular, El Mellah et al. (2020), EG20 hereafter, devised a model that uses statistical properties of the variability to infer clump sizes and masses. Colour-colour diagrams can provide access to the absorption variability, but they lack spectral resolution (Nowak et al. 2011; Hirsch et al. 2019; Grinberg et al. 2020). Excess variance spectra have proven to be a valuable in the study of ultra-fast outflows of AGN (see Ch. 3). As their spectral and timing resolution is only limited by the signal and the instrument, bright sources provide an opportunity for a high resolution study. I therefore apply excess variance spectroscopy to study the stellar wind variability in the HMXB Cyg X-1.

## 4.2 The stellar wind in Cygnus X-1

Cyg X-1 is one of the most studied HMXBs. As a bright and persistent source, it was discovered already in 1964 (Bowyer et al. 1965). The compact object is dynamically constrained to be a black hole (Gies & Bolton 1982) and recently, Miller-Jones et al. (2021) refined the mass estimate to  $21.2 \pm 2.2 M_{\odot}$ , making Cyg X-1 the most massive

stellar mass black hole known in an X-ray binary. The companion star HDE 226868 is an O9.7 Iab supergiant (Walborn 1973) with a mass of  $\sim 41 M_{\odot}$  (Miller-Jones et al. 2021). The mass loss rate of its wind is  $\sim 10^{-6} M_{\odot} \text{ yr}^{-1}$  (Herrero et al. 1995; Gies et al. 2003) and it reaches a terminal velocity of  $\sim 2100 \text{ km s}^{-1}$  (Herrero et al. 1995).

Figure 4.1 depicts the system and wind geometry. X-rays measurements, such as the orbital phase dependence of the column density, are consistent with this conclusion (see Miškovičová et al. 2016, and references therein). In general, the orbital phase and the inclination ( $i = 27.1^{\circ}$ , Orosz et al. 2011) determine which parts of the wind are being probed in an observation. At superior conjunction, the line of sight intercepts the wind close to the stellar photosphere and grazes the focused stream. At inferior conjunction, the wind is probed at a greater distance to the companion (see Fig 4.1).

Highly variable absorption is observed from Cyg X-1 especially in the low/hard state of the black hole (e.g., Feng & Cui 2002; Ibragimov et al. 2005; Boroson & Vrtilik 2010; Grinberg et al. 2015). For a discussion of accretion states in Cyg X-1 see, e.g., Wilms et al. (2006) and Grinberg et al. (2013). In particular, dips in the light curve are observed in soft X-rays preferentially at superior conjunction and interpreted as signatures of the clumps in the wind (see Grinberg et al. 2015, and references therein).

A paper series by Hanke et al. (2009), Miškovičová et al. (2016), and Hirsch et al. (2019) used high-resolution *Chandra* spectra to study the wind in the low/hard state in great detail. Hanke et al. (2009) investigated the non-dip spectrum at superior conjunction, identifying absorption lines from several H- and He-like ions and L-shell iron at low velocity shifts. Miškovičová et al. (2016) expanded this study to other orbital phases. They observed P-Cygni line profiles<sup>2</sup> at inferior conjunction, which point to weak absorption and a high projected velocity.

As the last paper in the series, Hirsch et al. (2019) investigated the mentioned absorption dips in the light curve, which are believed to be caused by clumps in the wind. Using time resolved spectra, they studied how absorption from silicon and sulphur ions evolves in the dips, finding that lower ionisation species appear and increase in relative strength with dip depth. From this result, Hirsch et al. (2019) concluded that material in the clumps has a lower ionisation than its surroundings and that deeper dips correspond to larger clumps. In other words, the clumps have a layered ionisation structure, with large clumps reaching lower ionisations in their centres.

An open question that remains from these studies is whether the dips are caused by individual, big clumps passing through the line of sight or by groups of several smaller ones. The geometry (spherical or “pancake”-like) and typical masses also remain to be constrained.

---

<sup>2</sup>A P-Cygni profile is a spectral line profile consisting of a broad emission line and a blue-shifted absorption line, and is a signature of an expanding stellar envelopes or wind. The absorption and emission components stem from the same atomic transition. Absorption only probes the material along the line of sight. In the case of a wind moving towards the observer, the absorption is therefore blueshifted. Emission on the other hand is observed from a much larger region, from material moving in different directions, resulting in a broadened emission component. P-Cygni profiles are named after the massive star P Cygni, where they are observed in the stellar wind.

### 4.3 Observations and Methods

To investigate the wind structure, I take advantage of the excellent spectral resolution of the High-Energy Transmission Grating (HETG) on-board *Chandra* and apply excess variance spectroscopy to the superior and inferior conjunction observations analysed in the paper series mentioned above (Hanke et al. 2009; Miškovičová et al. 2016; Hirsch et al. 2019). The existing studies constitute an excellent test case for constraining the stellar wind structure with excess variance spectroscopy.

#### 4.3.1 Chandra HETG observations of Cyg X-1

Two *Chandra* observations (ObsIDs 3814 and 11044) of Cyg X-1 taken in the low/hard state with the HETG (Canizares et al. 2005) and the Advanced CCD Imaging Spectrometer (ACIS, Garmire et al. 2003) were analysed. The observations cover the superior (3814, orbital phase  $\varphi = 0.93\text{--}0.03$ ) and inferior (11044,  $\varphi = 0.48\text{--}0.54$ ) conjunction passages, during which the line of sight probes different parts of the wind (see Fig. 4.1). Note that the low/hard classification of these observations follows Grinberg et al. (2013) and the orbital phases were assigned according to the ephemeris provided by Gies et al. (2003).

Detailed spectral analysis of both data sets has been performed in the studies mentioned in Sect. 4.2 (Hanke et al. 2009; Miškovičová et al. 2016; Hirsch et al. 2019). The existing results provide an opportunity to assess the capabilities of the approach against those of conventional analysis techniques. The observations were performed in timed exposure mode (TE), i.e., events are accumulated on the CCDs, transferred in the frame store, and read out. A full read-out cycle of the ACIS-S in TE mode usually takes 3.2 s, however, for the observations considered here the time is halved to 1.7 s, because only 512 of the 1024 available pixel rows were in use. I use the extracted event files provided by Miškovičová et al. (2016), but analyse the entirety of Obs. 3814, including dipping and non-dipping stages. The extractions were created using CIAO version 4.2. All four first order spectra from the High and Medium Energy Gratings (HEG and MEG, orders  $\pm 1$ ) of the HETG were included in the analysis. Refer to Miškovičová et al. (2016) and Hirsch et al. (2019) for further details on the data taking, extraction, and processing.

#### 4.3.2 Generation of the excess variance spectra

A spectral and time binning is performed on the extracted events, separately for the four first orders of the HEG and MEG. The spectral binning covers the  $2\text{--}14\text{\AA}$  band with a  $0.05\text{\AA}$  resolution and a 500 s step is used for the time binning. This choice is motivated by Hirsch et al. (2019), who state that the passage of a clump across the line of sight takes 0.5–5 ks, assuming that the observed dips in the spectrum are caused by single clumps and not multiple small clumps. By choosing a 500 s step, all of this clump variability can be captured, as the time step sets the upper bound of the frequency range the excess variance,  $F_{\text{var}}$ , integrates over (see Sect. 2.4). For a closer inspection later on, the spectral resolution is increased threefold and the time step is varied in the 50–2000 s range. While the spectral resolution and smallest time step are constrained by the signal strength, the

maximal time step should be chosen such that the light curve has a sufficient number of bins to obtain an accurate estimate of the variance ( $\gtrsim 20$ , Vaughan et al. 2003).

The  $F_{\text{var}}$  spectrum is calculated as described in Sect. 2.4. In the following, the excess variance is given in terms of its square,  $F_{\text{var}}^2$ , which is preferable if the signal is low:  $F_{\text{var}}$  contains a square root and becomes imaginary if the uncertainty,  $\overline{\sigma_{\text{err}}^2}$ , is larger than the signal variance,  $S^2$  (see Eq. 2.6). This case is relevant here because of the high resolution gratings data provide, dividing the signal over a large number of bins, compared to CCD data, which is usually used in  $F_{\text{var}}$  analyses. The average of  $F_{\text{var}}^2$  is always  $\geq 0$ , because the average of  $S$  has to stay above  $\overline{\sigma_{\text{err}}^2}$ . Negative values of  $F_{\text{var}}^2$  can therefore only be a result of random fluctuations, but are nevertheless useful as a consistency check for the  $F_{\text{var}}^2$  uncertainty. One sigma uncertainties are given unless otherwise noted.

## 4.4 Eliminating systematic variability

As detailed in Sect. 4.3.1, I analyse *Chandra* HETG data taken with the ACIS-S detector. For a variability study such as presented here, a solid understanding of the timing and read-out properties of the detector and associated systematic effects is vital. In the following, I discuss systematic variability due to read-out time and effective area differences of the gratings (Sect. 4.4.1), photon loss in CCD gaps and dead pixel rows (Sect. 4.4.2), and the discreteness of the CCD read-out cycle (Sect. 4.4.3).

### 4.4.1 Read-out time and effective area differences of the gratings

The ACIS-S detector consists of a row of six CCDs (see Fig. 2.3, right), which are read out in sequence. As a consequence, photons arriving simultaneously on different CCDs are registered at slightly different times. This effect becomes relevant if data from multiple gratings or orders, i.e., locations on the detector, are combined. Systematic effects of this kind are avoided by calculating  $F_{\text{var}}^2$  separately for each grating and order,  $i$ , and taking their weighted mean,

$$F_{\text{var}}^2 = \frac{1}{\sum_i \bar{x}_i^2} \sum_i F_{\text{var},i}^2 \cdot \bar{x}_i^2. \quad (4.1)$$

Weighting by the square of the mean number of counts,  $\bar{x}_i^2$ , gives equal weight to each count, regardless of which grating or order it belongs to. As the errors  $\text{err}(F_{\text{var},i}^2)$  are independent, they can be propagated according to

$$\text{err}(F_{\text{var}}^2) = \frac{1}{\sum_i \bar{x}_i^2} \sqrt{\sum_i \bar{x}_i^4 \cdot \text{err}(F_{\text{var},i}^2)^2}. \quad (4.2)$$

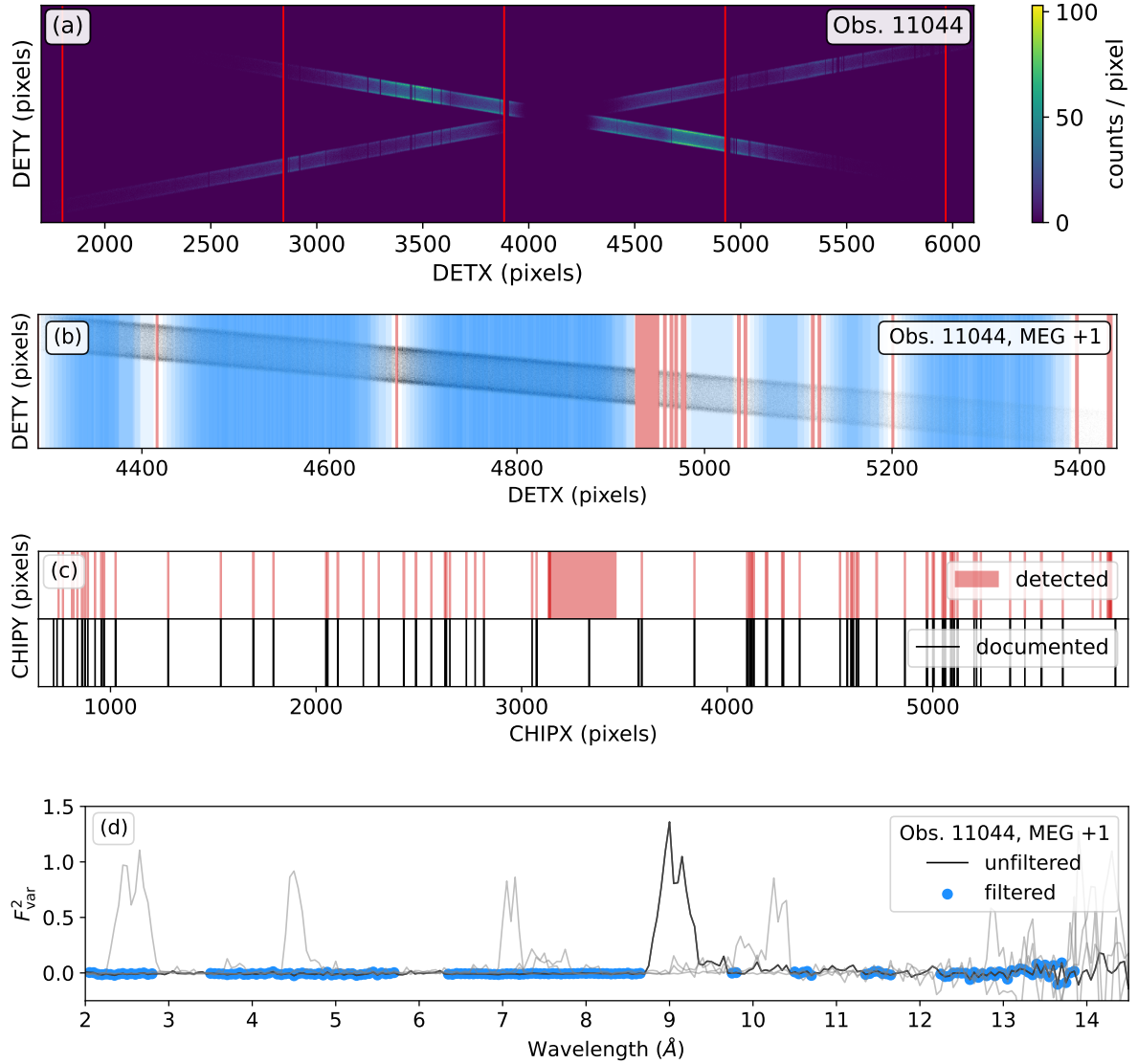


Figure 4.2: CCD gaps and dead pixel rows in *Chandra*'s ACIS-S detector are a major source of systematic variance (Härer et al. 2021b, in prep., Fig. A.1 (a–d), adapted). This figure illustrates the filtering procedure. (a) The distribution of counts on the ACIS-S CCD array, against which CCD gaps (*red*) and dead pixel rows clearly stand out. Panel (b) shows the filtered bins (*blue*) and gaps (*red*) as an overlay on a cut-out of the top panel (1st MEG spectrum). Only bins with a minimum distance of two pixels to the detected gaps pass the filtering. Panel (c) compares the positions of detected gaps to those of dead pixel rows documented in the ACIS `badpix` calibration file. The gap at  $\sim 3300$  pixels is not excluded because of a detector defect, but because it contains zeroth order and  $\lambda < 2\text{\AA}$  events. In panel (d), the resulting  $F_{\text{var}}^2$  is shown, with the filtered bins highlighted in blue and MEG  $-1$  and HEG  $\pm 1$  spectra (*light gray*) for comparison. Details on the filtering procedure can be found in the text. For clarity, data in panel (d) is displayed with lines and no errors are given.

### 4.4.2 Filtering CCD gaps and dead pixel rows

A second systematic effect is the increase in  $F_{\text{var}}^2$  due to photon loss in gaps between CCDs and rows of dead pixels. In the  $F_{\text{var}}^2$  spectrum, this increase manifests itself as spikes at specific wavelengths, which are not per se distinguishable from genuine features. Gap induced  $F_{\text{var}}^2$  spikes constitute the largest systematic effect, exceeding genuine features up to about an order of magnitude. The affected wavebands are detected and filtered out separately for each grating and order, as described below, before calculating and averaging their  $F_{\text{var},i}^2$ . The resulting reductions in sensitivity strongly vary between wavelength bands.

Figure 4.2(a) shows the distribution of counts on *Chandra*'s ACIS-S detector for Obs. 11044. The ACIS-S consists of a row of six quadratic CCDs (see Fig. 2.3, right), on which photons are dispersed by the HEG and MEG, resulting in a cross-like shape. Due to this design, a small amount of photons are lost at the boundaries between CCDs, in the so-called CCD gaps (Garmire et al. 2003). Rows of dead pixels have the same effect. I jointly refer to CCD gaps and dead rows as gaps in the following. To avoid the photon loss exclusively affecting specific wavelengths, the telescope pointing moves in a Lissajous pattern, periodically changing the zeroth order position on the detector, which averages the loss over a small wavelength range (referred to as dither; Garmire et al. 2003). As a secondary effect, the number of detected photons strongly varies with time in range of a gap, which strongly affects variability analyses. The diagonal positioning of the gratings increases the affected range, because it causes one gap to affect a range of wavelengths at any given moment.

To account for the systematic variability introduced by the dither, I exclude all bins within dither range of gaps. The first steps towards identifying these bins is finding the positions of all gaps, by searching for pixel rows with zero counts along the  $x$ -coordinate of the detector, considering all events within 2–14.5Å. In this range, the number of counts per pixel is high enough to conclude that pixel rows with zero counts are likely an instrumental effect and not due to low signal. The detected gaps run across both the HEG and MEG spectrum, also indicating that they are instrumental.

A total of  $\sim 70$  coinciding gaps was detected in Obs. 11044 and 3814, including the CCD gaps, whose positions were correctly reproduced. Eight additional gaps were picked up by the algorithm in Obs. 11044, but not in 3814, despite being visible by eye at coinciding positions. I therefore add these gaps in by hand in Obs. 3814. The detected gaps were verified by comparing them to the positions of dead rows documented in the ACIS `badpix` calibration file. As shown in Fig. 4.4.2 (c), all dead rows in the investigated range were found and have matching width. Note that the coloured region centred at  $\sim 3300$  pixels is excluded from the analysis, because it contains zeroth order and  $\lambda < 2\text{\AA}$  events, not because of a defective chip section.

The second step is to identify all wavelength bins which are in dither range of gaps. For each gratings arm, I calculate the minimal and maximal  $x$  position of all events in a given bin and check if the closest gap is at least a two pixel distance below the minimal or above the maximal value. If not, the bin is discarded. By requiring a distance of at least two pixels, the algorithm is able to discard bins that are only half covered by a gap.

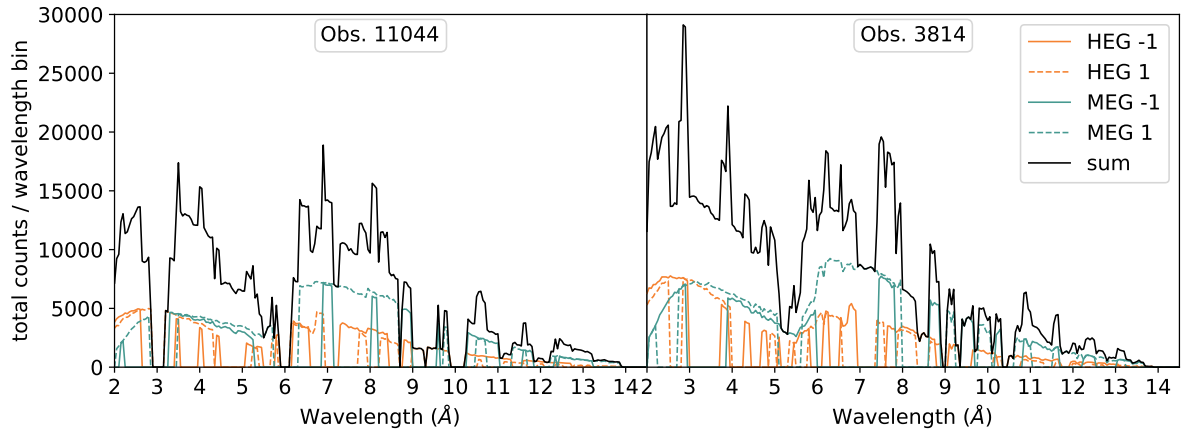


Figure 4.3: Härer et al. 2021b, in prep., Fig. A.1 (e), adapted: Total counts per wavelength bin in Obs. 11044 (*left*) and 3814 (*right*) after filtering, for all gratings arms (*orange and green, straight and dashed lines*) and their sum (*black line*). For clarity, data is displayed with lines and no errors are given.

As an example, a result of this selection is shown in Fig. 4.2 (b) and (d) for the first order MEG spectrum. In panel (b), the spread of all bins that passed the filtering is shown in transparent blue and the gaps are marked in red. As intended, the filtered bins do not overlap with the gaps. Panel (d) compares the filtered and unfiltered  $F_{\text{var}}^2$  spectra. CCD gaps cause huge, often double-peaked spikes. The shape results from the fact that the amount of arriving photons varies more strongly for bins around the gap edge than for bins largely covered by the gap. Dead pixel rows give rise to smaller features because they are narrower. The filtering algorithm succeeds in cutting out the large CCD gap spike, as well as several smaller ones caused by the gaps indicated in the figure above.

Figure 4.3 shows the effect of filtering on the number of counts available for the analysis in each wavelength bin. Depending on how the filtered wavelengths align across the gratings arms, the number of counts fluctuates greatly. In a small number of bins no signal is left, which results in the gaps in the data in Fig. 4.5. Note that the slightly visible two hump structure is a result of *Chandra*'s effective area (see Fig. 2.1) and that the higher number of counts in Obs. 3814 is due to a higher exposure time.

#### 4.4.3 Estimating binning variability

The *Chandra* ACIS-S detector has a read-out time of the order of seconds (Garmire et al. 2003), which not only limits its timing resolution, but also introduces systematic variability if the data are binned. Intuitively, some photons are assigned to time bin  $n + 1$  instead of  $n$ , because of the delay between photon arrival and read-out.

The magnitude of this effect is estimated with Monte Carlo Simulations. A random constant light curve is generated by drawing photon arrival times from a constant distribution, separately for each observation, order, and grating, with their respective count numbers and exposure times. The read-out is simulated by rounding up the

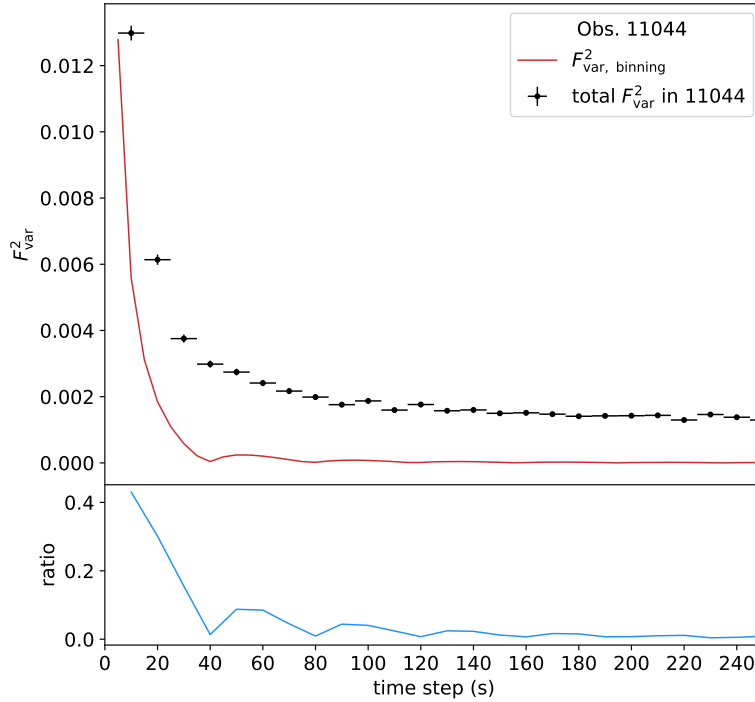


Figure 4.4: Systematic variability,  $F_{\text{var}, \text{binning}}^2$ , introduced by the timing resolution of the ACIS detector (*red line*) compared to total  $F_{\text{var}}^2$  in the broad band (2–14Å, *black data points*) and their ratio, shown in the bottom panel (Härer et al. 2021b, in prep., Fig. B.1). As a time step of 500 s is used for Obs. 11044, the effect is negligible.

arrival times to the next larger time stamp present in the data, imprinting the read-out times from the observation on the simulated data. Note that the average count rates of Cyg X-1 in Obs. 11044 and 3814 are  $\sim 90$  and  $\sim 70$   $\text{cts s}^{-1}$ , respectively, which makes it very unlikely that this approach misses read-out cycles because no photons arrived. I confirm this assumption by checking that there are no significant outliers in the time differences between consecutive events that exceed the read-out time. For each observation, order, and grating, this procedure is repeated 100 times and the resulting  $F_{\text{var}}^2$  values are averaged. Combining all gratings and orders as described in Sect. 4.4 yields the systematic binning variability,  $F_{\text{var}, \text{binning}}^2$ . The one sigma error on  $F_{\text{var}, \text{binning}}^2$  is below  $2 \cdot 10^{-4}$ , for both Obs. 3814 and 11044.

An example of the simulation for Obs. 11044 is shown in Fig. 4.4 as a function of binning time step.  $F_{\text{var}, \text{binning}}^2$  strongly increases as the bin size approaches the read-out time, which is expected, as a smaller binning is more sensitive to a disturbance of a fixed magnitude. The periodicity in the ratio is caused by the binning time step matching an integer multiple of the duration of a read-out cycle. For a time step of 500 s, which was chosen for Fig. 4.5,  $F_{\text{var}, \text{binning}}^2$  is below 0.9% of the total variability over the 2–14Å band in Obs. 11044. The analysis of Obs. 3814 uses time steps as short as 50 s, but due to the higher variability of this observation, the fraction stays below 0.3%. In absolute terms,

$F_{\text{var, binning}}^2$  always stays below  $2.5 \cdot 10^{-5}$  for time steps above 500 s in Obs. 11044 and below  $2.7 \cdot 10^{-4}$  for time steps above 50 s in Obs. 3814 at a one sigma confidence.

It can therefore be concluded that  $F_{\text{var, binning}}^2$  does not significantly impact the analysis, but it is important to note that the effect generally should be considered when investigating the excess variance at a timing resolution approaching the read-out time of the instrument.

## 4.5 Results

In the following, the excess variance spectra resulting from the procedure described above are presented. I investigate variability in the continuum and absorption lines, as well as the frequency dependence.

### 4.5.1 Overview: $F_{\text{var}}^2$ continuum and spike features

Figure 4.5 shows the  $F_{\text{var}}^2$  spectrum for both investigated data sets, Obs. 3814 and 11044, taken during the superior and inferior conjunction passage, respectively, in the 2–14 Å range. A major difference exists between the two: at inferior conjunction, the variability is consistent with zero, while a continuum is present at superior conjunction, which linearly increases with wavelength above  $\sim 3$  Å. The linear fit shown in Fig. 4.5 serves to qualitatively characterise this trend and the significance of the superimposed features, the most prominent of which is a spike-like increase in variability just below 7 Å. In contrast, the observation at inferior conjunction shows no significant  $F_{\text{var}}^2$  spectral features.

Figure 4.6 shows the  $F_{\text{var}}^2$  spectrum at superior conjunction for a higher resolution, relative to the linear fit. Overlaid are the positions of H- and He-like absorption lines detected by Hanke et al. (2009) in their analysis of the non-dipping spectrum of the same observation. Also shown are the lower ionisation silicon and sulfur lines found by Hirsch et al. (2019) in this observation during dipping. Laboratory wavelength are given for all lines.

The previously mentioned most significant spike feature just below 7 Å corresponds to the silicon line region. At the increased resolution, the feature splits in multiple spikes at positions corresponding to those of the lines. A similar group of spikes is seen in the sulphur region, but is less prominent, which is likely due to a reduction in signal caused by gap filtering strongly increasing the uncertainty (see Sect. 4.4.2).

An alignment of detected lines and spike features exists outside the silicon and sulphur regions as well: hints of neon (e.g., Ne x Ly  $\delta$ – $\eta$  at 9.2–9.5 Å), magnesium (e.g., Mg XII Ly  $\alpha$  at 8.42 Å and Mg XI He  $\alpha$  at 9.17 Å), and aluminium (Al XII He  $\alpha$  at 7.76 Å) features can be seen in Fig. 4.6. In general, more spikes seem to be present close to known lines than in line-free regions. However, due to the low signal to noise ratio and strength of the  $F_{\text{var}}^2$  features, such detections are tentative. As previously mentioned, the  $F_{\text{var}}^2$  spectrum of Obs. 11044 shows far less features. A higher resolution  $F_{\text{var}}^2$  spectrum is shown in Fig. 4.7.

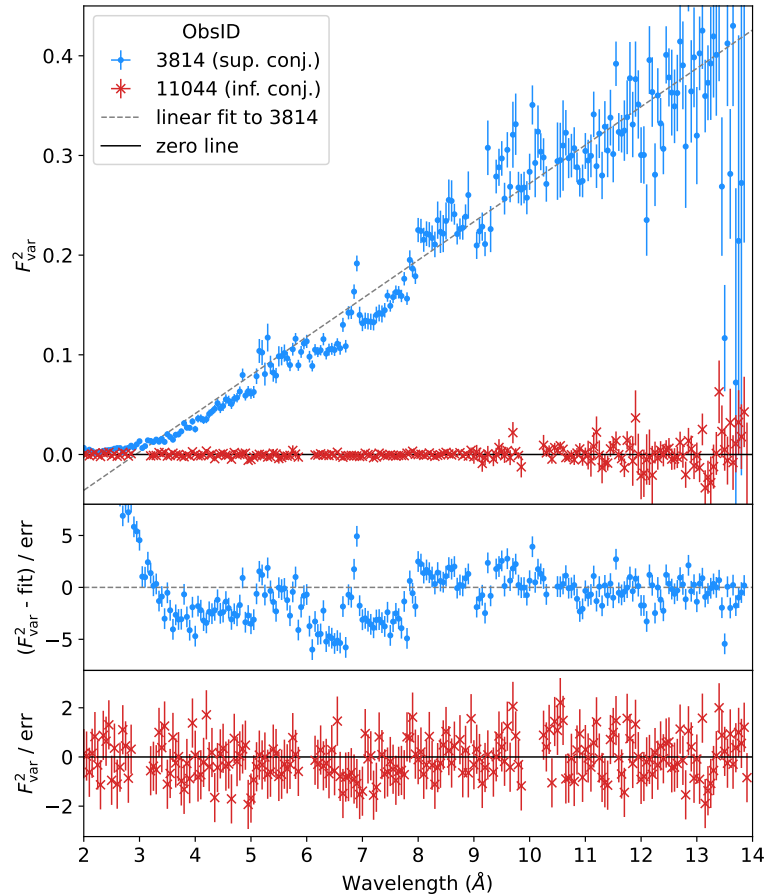


Figure 4.5: The  $F_{\text{var}}^2$  spectrum of Obs. 3814 (*blue*) and 11044 (*red*) during which Cyg X-1 passed through superior and inferior conjunction, respectively (Härer et al. 2021b, in prep., Fig. 2). Residuals to a continuum estimate (a linear fit for 3814, the zero-line for 11044) are shown in the bottom panels. The gaps in the  $F_{\text{var}}^2$  spectrum of Obs. 11044 around  $3\text{\AA}$ ,  $6\text{\AA}$ , and  $10\text{\AA}$  are due to the filtering of systematic variability from CCD gaps in *Chandra*'s HETG detector (see Sect. 4.4.2).

In Sect. 4.5.2, the silicon and sulphur line regions in Obs. 3814 are discussed in more detail, as these contain the most prominent features. Their time dependence will be investigated in Sect. 4.5.3. As this work is among the first studying  $F_{\text{var}}^2$  spectra at gratings resolution (predated only by Mizumoto & Ebisawa 2017, to my knowledge), the aim is to assess the prospects of this approach. A systematic search and identification of the observed features is not performed. In addition, a quantitative analysis is challenging, because it requires an accurate description of the continuum spectrum.

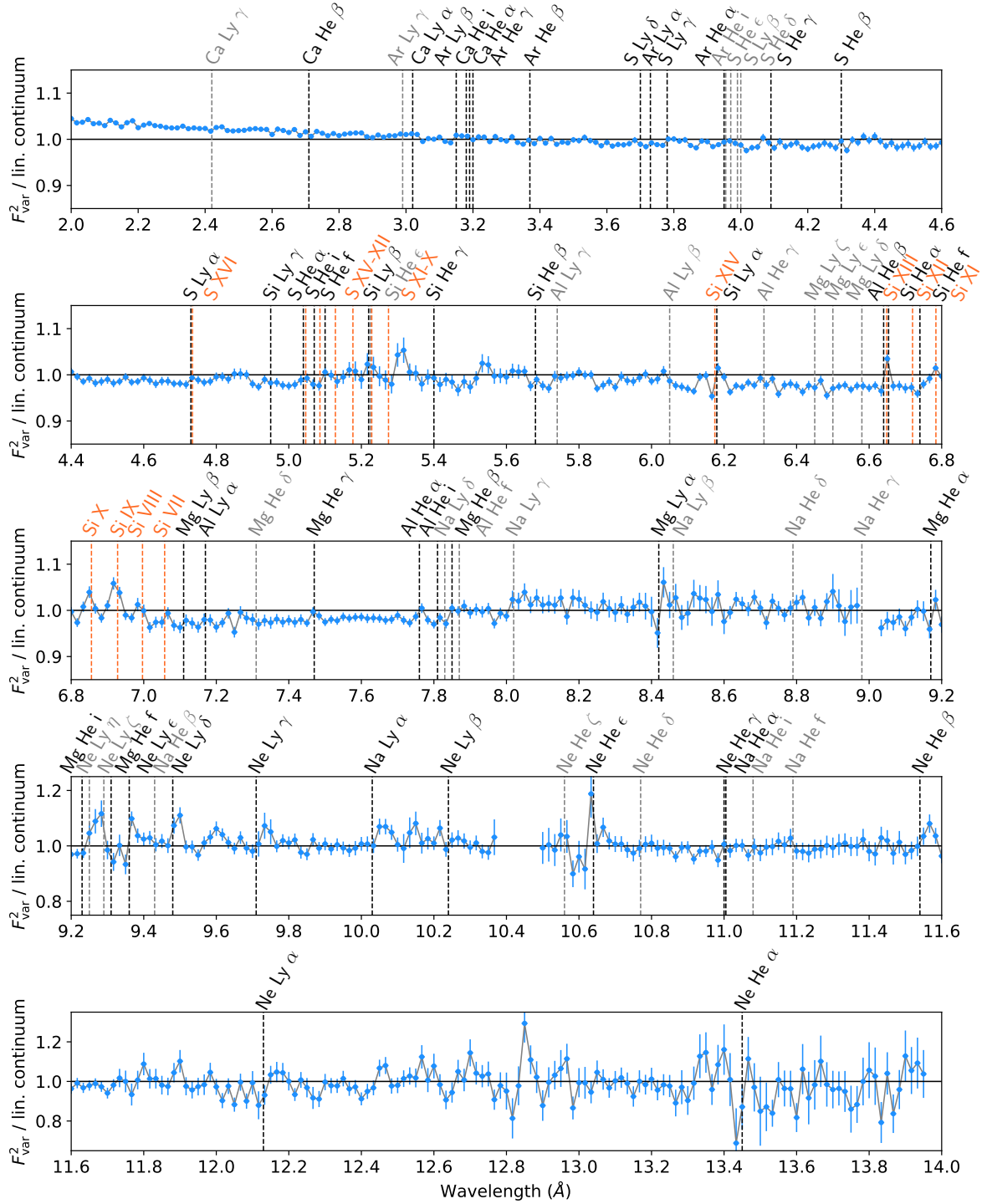


Figure 4.6: The  $F^2_{\text{var}}$  spectrum of Obs. 3814, relative to the continuum fit from Fig. 4.5 (Härer et al. 2021b, in prep., Fig. 3, adapted). The rest wavelength of H and He-like absorption lines identified by Hanke et al. (2009) (*black*, weak lines in *grey*) and S and Si lines from Hirsch et al. (2019) (*orange*) are shown. Positions of lines and spike features tend to align. The data points are connected by a grey line for clarity.

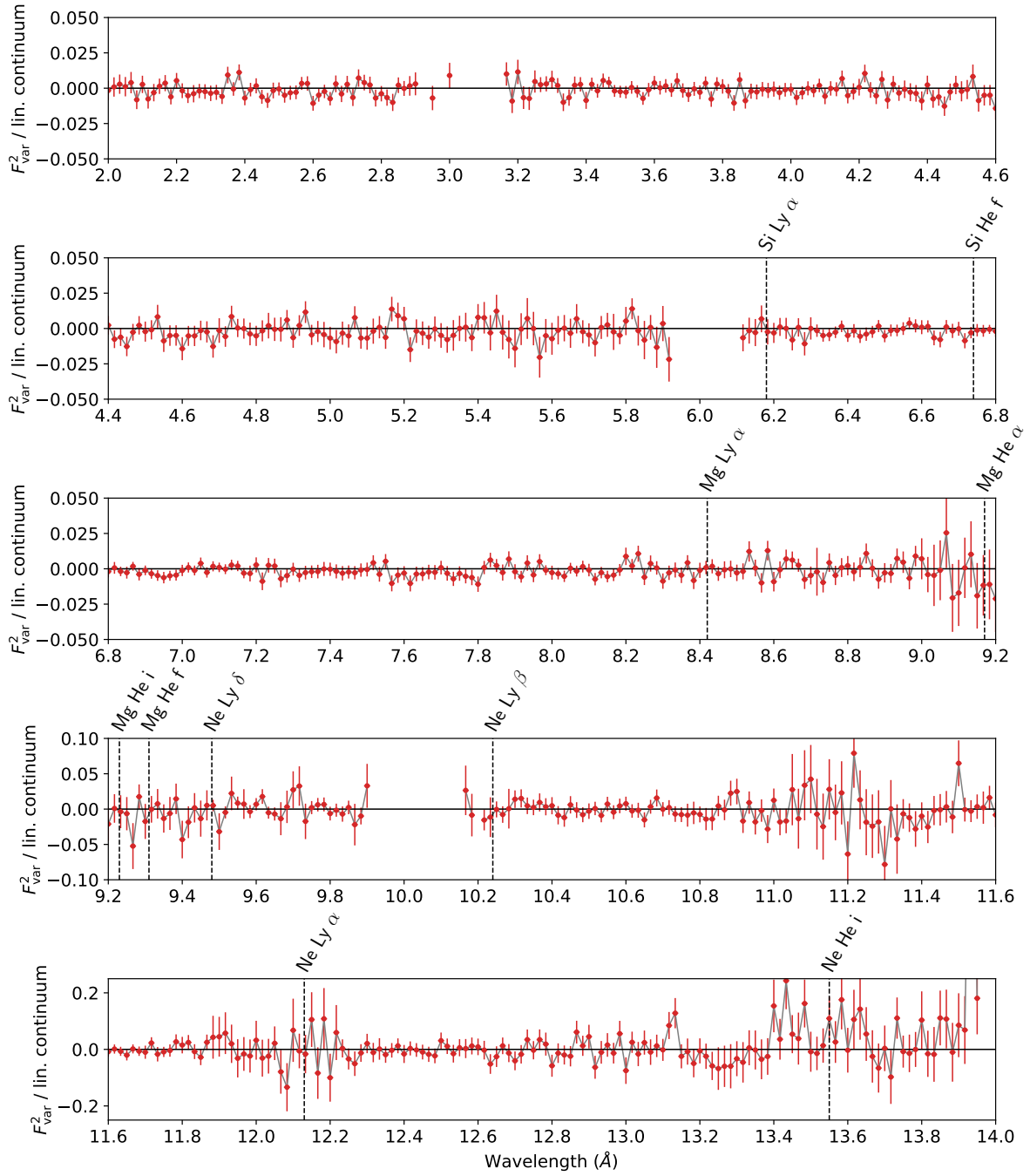


Figure 4.7: Detailed  $F^2_{\text{var}}$  spectrum of Obs. 11044, overplotted with the positions of line features identified by Mišková et al. (2016) (black), selected as described in Sect. 4.5 (Härer et al. 2021b, in prep., Fig. C.1, adapted). In contrast to Obs. 3814, the reported lines are P-Cygni profiles, which makes the absence of spike features plausible (see Sect. 4.6.4).

### 4.5.2 Silicon and sulphur line regions at superior conjunction

Figure 4.8 shows a zoom-in on the silicon and sulphur regions. In addition to the 500 s binning investigated before, a 50 s binning is shown to investigate if there is additional variability at higher frequencies. The bottom panels of Fig. 4.8 show the count spectra from Hirsch et al. (2019), summed for all dip stages, relative to local powerlaw fits in the given bands, to allow for a direct visual comparison to the  $F_{\text{var}}^2$  spectrum.

For silicon, a spike is clearly detected for each corresponding line, except for Si XII, which might be because it cancels out with the neighbouring He-like Si forbidden emission line. Line emission typically decreases variability, because, when looking at an object, the observer sees the sum of emission from all regions, in which variability in individual regions is averaged out (Parker et al. 2017a). Visually, the spike positions and strength directly correspond to those of the lines. The asymmetries present in some of the absorption lines in the analyses of the count spectra by Miškovičová et al. (2016) and Hirsch et al. (2019) are also hinted at in the spikes, albeit with greater uncertainties and lower resolution. The heights and widths of the spikes are slightly larger in the 50 s binning, but this increase is not enough to exceed the uncertainty.

The analysis of the sulphur region is complicated by a greatly reduced signal, as laid out in Sect. 4.5.1. Nevertheless, there is a small but visible increase in overall variability. Spike features are resolved and approximately coincide with line positions, with the best agreement for S XI and S XII. S XIII and S XIV cannot be resolved in the  $F_{\text{var}}^2$  spectrum, resulting in a joined spike. A spike feature with no corresponding line is present at  $\sim 5.33\text{\AA}$ , but does not challenge the general conclusion that spike and line positions coincide, due to the large uncertainties and the clear result for silicon. As for silicon,  $F_{\text{var}}^2$  slightly increases for the shorter, 50 s time step, but remains within the uncertainty.

### 4.5.3 Frequency dependence at superior conjunction

The timescale of the variability can give an insight into its producing mechanism, for example the typical sizes of overdensities in a stellar wind that produces variability by obscuration (e.g., EG20). I investigate the timescale by changing the upper bound of the frequency range  $F_{\text{var}}^2$  integrates over. In practice, the upper bound is set by the binning time step of the light curves from which  $F_{\text{var}}^2$  is calculated (see Sect. 2.4). Figure 4.9 shows the result of this approach, where the upper bound is given on the  $x$ -axis, in terms of the binning time step, and the lower bound of the frequency range is kept fixed at the length of the observation. The figure therefore effectively shows an integrated frequency spectrum, that is to say, its slope indicates the power added to  $F_{\text{var}}^2$  at any given frequency.

In the figure, bands containing the bulk of detected silicon (6.6–7.2 $\text{\AA}$ ) and sulphur (5–5.35 $\text{\AA}$ ) lines are compared to a reference band, spanning the range in between them (5.4–6.6 $\text{\AA}$ ), but excluding a region of  $\pm 0.05\text{\AA}$  around the Si XIV line. The bottom panel shows the ratio of  $F_{\text{var}}^2$  in the line regions to the reference band. The  $F_{\text{var}}^2$  in each band is rescaled to its value at  $t = 500$  s:  $0.137 \pm 0.001$ ,  $0.105 \pm 0.002$ , and  $0.082 \pm 0.004$ , for the silicon, sulphur, and the reference band, respectively. Note that these values are not

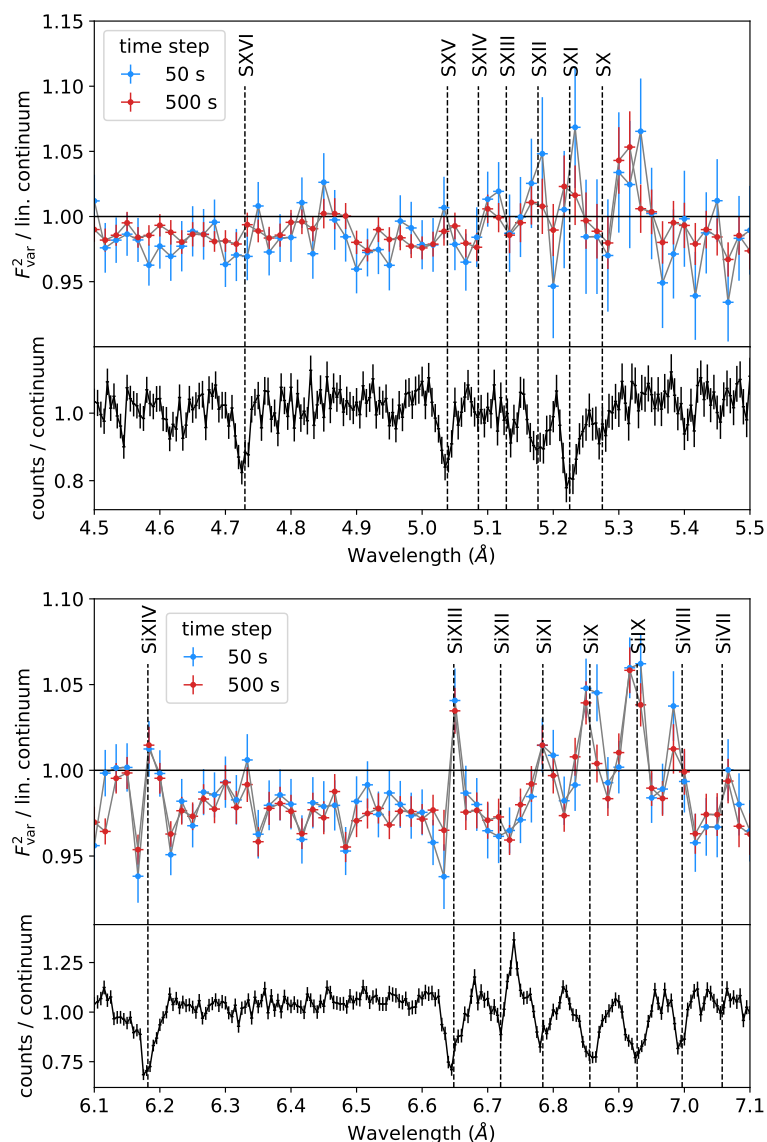


Figure 4.8: Sulphur (*top*) and silicon (*bottom*) line regions (Härer et al. 2021b, in prep., Fig. 4). The  $F_{\text{var}}^2$  spectrum of Obs. 3814 is shown relative to the linear fit from Fig. 4.5 (*black*) and compared to the count spectrum (*lower panels*) from Hirsch et al. (2019) and the rest-wavelength of detected lines. The count spectrum is given relative to a local powerlaw fit, in the wavelength bands indicated in the figure, and is the sum of spectra of all dip stages. Two time binnings are displayed for the  $F_{\text{var}}^2$  spectrum, 50 s (*blue*) and 500 s (*red*), to investigate the effect of the added higher frequencies. Lines connect the data points for clarity. Overall, there is a good correspondence between  $F_{\text{var}}^2$  spike features and known line positions.

normalised to the linear continuum fit, which means that  $F_{\text{var}}^2$  is highest in the silicon region due to the continuum, not the line variability. For the choice of time steps, refer to Sect. 4.3.1.

Overall,  $F_{\text{var}}^2$  declines approximately linearly with binning time step in the logarithmic scaling, which is consistent with an underlying red noise process. The silicon line region shows a flatter trend than the reference band, i.e., the power is distributed more towards lower frequencies in the silicon line region than in the close-by  $F_{\text{var}}$  continuum. For sulphur, the behaviour is consistent with the continuum, but subject to large uncertainties.

A possible systematic effect is the periodicity of the dither in the telescope pointing<sup>3</sup> that is introduced to average photon loss due to defective pixels. The light grey band in Fig. 4.9 indicates the range where such an effect would be expected<sup>4</sup>. As no significant increase in  $F_{\text{var}}^2$  relative to the overall trend is present in this region, it can be concluded that the dither periodicity is not an issue.

## 4.6 Discussion

This section explores the driving mechanism behind the observed variability, models the strong orbital phase dependence based on EG20, and discusses implications for the wind geometry and structure and the role of varying ionisation.

### 4.6.1 Absorption driven variability

Variability can be caused by intrinsic changes in flux, originating close to the compact object, or be a result of obscuration by material passing through the line of sight (see Sect. 2.3). In the latter case, the variability can be greatly sensitive to the line of sight. A notable difference is present in the continuum variability between inferior and superior conjunction. While the continuum variability at superior conjunction increases linearly with wavelength, it is constant and consistent with zero at inferior conjunction. The observations also differ in another respect: while the light curve is constant at inferior conjunction, strong transient dipping events are present at superior conjunction (Miškovičová et al. 2016). As detailed in Sect. 4.2, it is well established that the dipping events are caused by clumps in the stellar wind. During both observations, Cyg X-1 was in the low/hard state at very similar fluxes. Jointly, these results strongly supports the conclusion that the observed variability is driven by clumps crossing the line of sight.

On the continuum, spikes of increased variability are observed. In Sect. 4.5.2, a clear correspondence between properties of  $F_{\text{var}}^2$  spikes and absorption lines was reported, in the silicon line region and, at reduced significance due to lower sensitivity, also in the sulphur line region. This result suggests that the spikes are caused by an increased variability

---

<sup>3</sup>see The *Chandra* Proposer’s Observatory Guide, Sect. 6.12

(<https://cxc.cfa.harvard.edu/proposer/POG/html/ACIS.html>, visited August 19, 2021, 6:18 pm)

<sup>4</sup>see *Chandra* CIAO supplemental information on dither

(<https://cxc.cfa.harvard.edu/ciao/why/dither.html>, visited August 19, 2021, 6:19 pm)

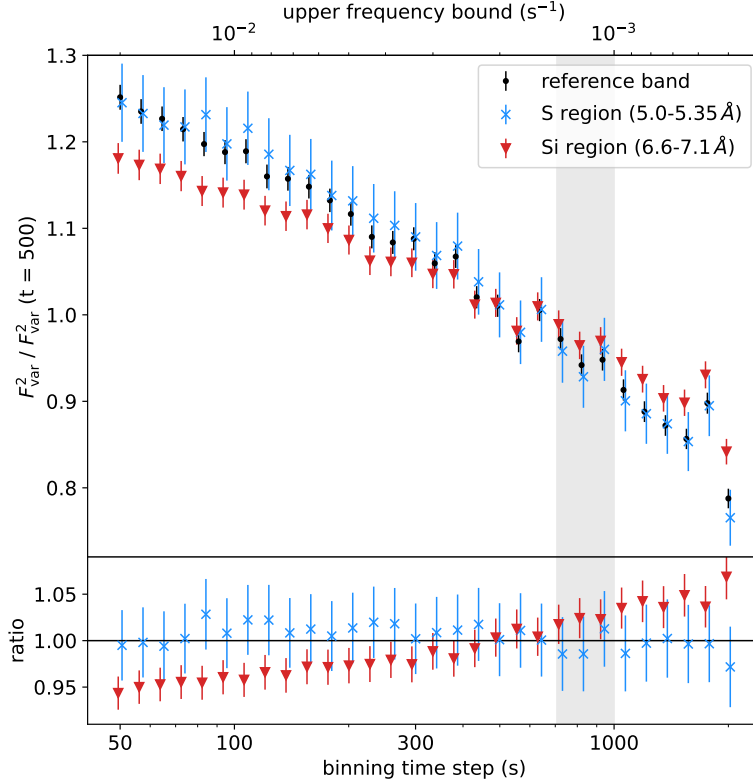


Figure 4.9: Total variability in Obs. 3814 in terms of  $F_{\text{var}}^2$  as a function of the binning time step, i.e., the figure effectively shows integrated frequency power (Härer et al. 2021b, in prep., Fig. 5). The sulphur (*blue*, 5–5.35Å) and silicon (*red*, 6.6–7.2Å) line regions are compared to a reference band (*black*, 5.4–6.6Å, excluding a region of  $\pm 0.05$ Å around the Si XIV line), with the ratio shown in the bottom panel.  $F_{\text{var}}^2$  is normalised to its value at 500 s in each respective band. The light grey band indicates a range where systematic effects due to the dither of the telescope would arise, if they were present.

inherent to the absorption lines, which is also observed in ultra-fast outflows of AGN (see Ch. 3). A general prevalence of spikes near known lines outside the silicon and sulphur regions further supports this conclusion. Both intrinsic and absorption variability can explain this spiking of  $F_{\text{var}}^2$  in the lines. In ultra-fast outflows, the enhanced variability is plausibly consistent with the ionisation responding to intrinsic luminosity changes (see Ch. 3). Considering again that Cyg X-1 has a clumpy wind and that the clumps have a layered ionisation structure (see Sect. 4.2), it seems plausible that the same mechanism is also at work in Cyg X-1. However, in an optically thin medium such as the wind, the line strength also directly responds to a change in the column density, without requiring an associated ionisation change. It is likely that both mechanisms contribute to the observed enhancement of the line variability. The role of ionisation is discussed further in Sect. 4.6.6.

### 4.6.2 Modelling the orbital phase dependent variability of a clumpy stellar wind

In the last section, column density changes due to clumps passing through the line of sight were identified as main driver of the variability. I now compare the results from the  $F_{\text{var}}^2$  analysis to a model based on a clumpy stellar wind model by EG20 and an XSTAR (Kallman & Bautista 2001) table model to accommodate ionisation effects.

EG20 model the neutral X-ray absorption by a clumpy wind in a binary system consisting of a massive star and a compact object, described as an X-ray point source. The mass is assumed to be contained in spherical clumps, which start with a radius,  $R_{\text{cl}}$ , at two stellar radii,  $2R_{\star}$ , from the stellar centre, growing in size and accelerating as they move outwards according to the canonical velocity law for stellar winds,

$$v(r) = v_{\infty}(1 - R_{\star}/r)^{\beta}, \quad (4.3)$$

where  $\beta$  is a factor determining how quickly the terminal wind velocity,  $v_{\infty}$ , is reached. The smooth expansion law is employed for the clump size (Eq. 4 in EG20) but note that the impact of the clump expansion law on the variability is expected to be small (see EG20). The clump mass stays constant during the expansion and acceleration, i.e., clumps do not merge or split. The wind is assumed to be spherically symmetric and fast enough to be unaffected by the gravity of the compact object, which is a valid assumption for Cyg X-1 for two reasons: the terminal wind speed ( $2100 \text{ km s}^{-1}$ ) is high compared to the orbital speed ( $500 \text{ km s}^{-1}$ ) and more importantly, the bulk of material intercepting the line of sight is above the orbital plane and therefore outside of the focused stream.

The model calculates the neutral equivalent hydrogen column density,  $N_{\text{H}}$ , resulting from the clumpy wind for a given line of sight parameterised by the inclination,  $i$ , and orbital phase,  $\varphi$ . The parameters that EG20 give for Cyg X-1 are adopted:  $i = 27.1^{\circ}$ , mass outflow rate,  $\dot{M} = 3 \cdot 10^{-6} M_{\odot} \text{ yr}^{-1}$ ,  $v_{\infty} = 2100 \text{ km s}^{-1}$ , and orbital separation,  $a = 2.5 R_{\star}$ . Orbital phases of  $\pm 0.1$  around superior and inferior conjunction are covered, with a resolution of 20000 points, resulting in a time step of  $\sim 5 \text{ s}$ . The  $N_{\text{H}}$  light curves were provided by Ileyk El Mellah. For further details on the model and its application to Cyg X-1 see EG20.

The  $N_{\text{H}}$  light curve obtained from the clumpy wind model is then used to create absorbed model spectra, from which  $F_{\text{var}}^2$  can be calculated. To this end, an absorbed powerlaw is faked<sup>5</sup> for each value in the  $N_{\text{H}}$  light curve with the ISIS command `fakeit`. The powerlaw index and normalisation were fixed to the values obtained by Hanke et al. (2009) for the *Chandra* and *RXTE*<sup>6</sup> joined continuum of Obs. 3814 ( $\Gamma = 1.60$ , norm = 1.33, see Table 2 in the reference). An XSTAR table model representative of the conditions in Cyg X-1 is used to account for the fact that the wind is ionised. The XSTAR model was provided by Ralf Ballhausen. More information about the XSTAR model can be found in Härer et. al (2021b), in prep.

<sup>5</sup>In this context, a faked spectrum refers to a simulated spectrum which has been populated with random values following the shape of a model function.

<sup>6</sup>The Rossi X-ray Timing Explorer (RXTE) was a NASA X-ray telescope that monitors the X-ray sky and could therefore be used to study the long-term behaviour of bright sources.

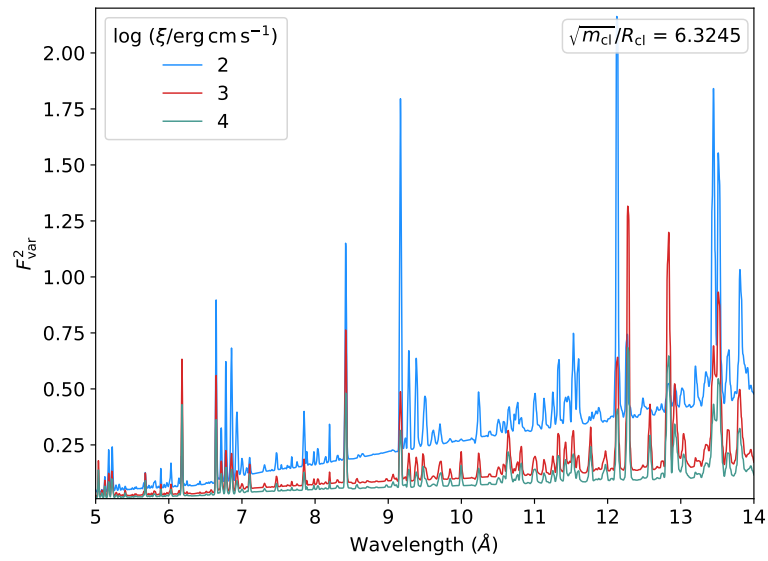
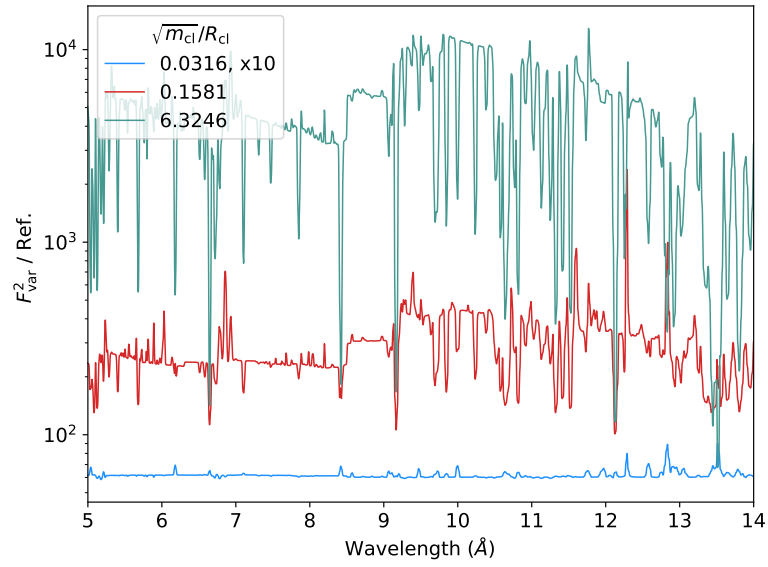
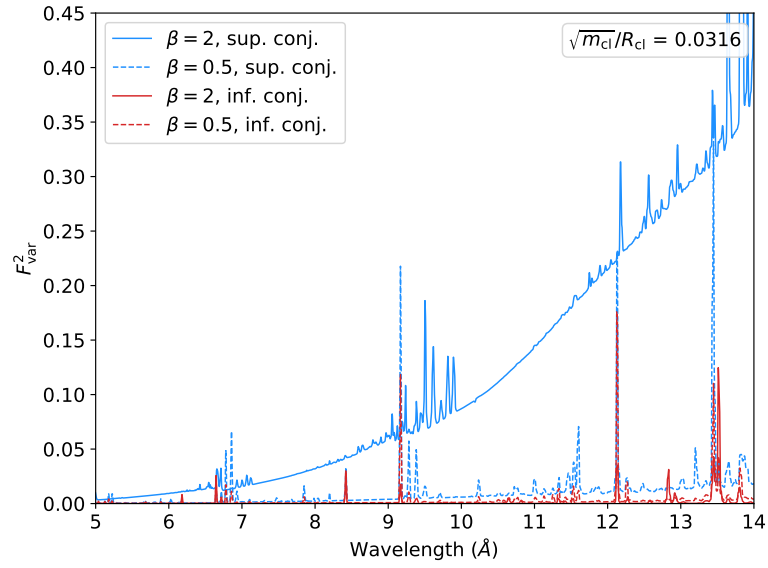


Figure 4.10:  $F_{\text{var}}^2$  expected for absorption in a clumpy wind following EG20 (Härer et al. 2021b, in prep., Fig. 6). Details on the model generation can be found in the text. *Upper panel*: dependence on the line of sight (*blue*: superior conjunction, *red*: inferior conjunction) and the  $\beta$  value of the wind velocity law (Eq. 4.3; *solid*:  $\beta = 2$ , *dashed*:  $\beta = 0.5$ ), highlighting their strong impact on the continuum. *Middle panel*: ratio to a baseline model with  $m_{\text{cl}}^{0.5} R_{\text{cl}}^{-1} = 0.0079$ , showing the increase in continuum variability and with  $m_{\text{cl}}^{0.5} R_{\text{cl}}^{-1}$  and the reduced increase of the line variability (dips in the ratio). The lowest-ratio model (*blue*) has been multiplied by a factor of 10 for better visibility. *Bottom panel*: ionisation dependence. A high  $m_{\text{cl}}^{0.5} R_{\text{cl}}^{-1} = 6.3245$  is shown to highlight the continuum changes. The increase in  $F_{\text{var}}^2$  with ionisation is weaker for higher ionisations. For clarity, the model is only shown above  $5\text{\AA}$ .

The  $F_{\text{var}}^2$  spectra resulting from this approach are shown in Fig. 4.10. I investigate the dependence on  $\beta$ , the line of sight, the ionisation parameter of the XSTAR model,  $\xi$ , and the ratio  $m_{\text{cl}}^{0.5} R_{\text{cl}}^{-1}$ , where  $m_{\text{cl}}$  and  $R_{\text{cl}}$  are given as multiples of  $m_0 = 1.1 \cdot 10^{24}$  g and  $R_{\star} = 17 R_{\odot}$ <sup>7</sup>. The clump mass,  $m_{\text{cl}}$ , takes values of  $4 \cdot 10^{-7}$  and  $10^{-5} m_0$  and  $R_{\text{cl}}$  ranges over  $0.005$ – $0.08 R_{\star}$ . The choice of the combined parameter  $m_{\text{cl}}^{0.5} R_{\text{cl}}^{-1}$  is motivated by EG20, who found that it is proportional to the spread of the column density,  $\delta N_{\text{H}}$  (defined according to EG20, Sect. 3.2). If variability is caused by  $N_{\text{H}}$  changes, as the model assumes, then  $\delta N_{\text{H}}$  directly translates in  $F_{\text{var}}^2$  variability. Two values for  $\beta$  are considered, 0.5 and 2. The former is widely used in the literature and believed to be representative of winds of early O supergiants (Sundqvist et al. 2019), while the latter corresponds to the velocity profiles computed by Sander et al. (2018), showing a more gradual acceleration. Unless otherwise indicated, the ionisation is fixed at  $\log \xi = 3$ ,  $\beta = 0.5$ , and variability at inferior conjunction is shown. The ionisation,  $\xi$ , is always given in units of  $\text{erg cm s}^{-1}$ .

### 4.6.3 Line of sight dependence of the variability continuum

The upper panel of Fig. 4.10 demonstrates that the model is able to qualitatively reproduce the data, by predicting an approximately linear continuum and spikes of increased  $F_{\text{var}}^2$ . The model also shows a strong line of sight effect, with higher variability at superior conjunction. The effect is especially strong for the higher  $\beta$  value,  $\beta = 2$ , and is a direct consequence of how  $\delta N_{\text{H}}$  depends on the orbital phase. The clumps probed at superior conjunction are smaller, because the line of sight runs closer by the star than at inferior conjunction and the clumps expand as they move outwards. As  $\delta N_{\text{H}} \propto m_{\text{cl}}^{0.5} R_{\text{cl}}^{-1}$ , the variability is higher at superior conjunction. A high  $\beta$  increases this effect, because the

<sup>7</sup>Note that the stellar radius given in EG20 is adopted here, instead of the updated value of  $R_{\star} = 22.3 R_{\odot}$  (Miller-Jones et al. 2021). The results are unaffected by this slight inconsistency, because  $R_{\star}$  only functions as a scaling factor for the  $m_{\text{cl}}^{0.5} R_{\text{cl}}^{-1}$  ratio.

slower acceleration requires a higher density and therefore more clumps for fixed  $\dot{M}$ . The variability increases with wavelength, because lower energy photons are more easily absorbed and therefore also more sensitive to changes in absorption.

For  $\beta = 2$  and  $m_{\text{cl}}^{0.5} R_{\text{cl}}^{-1} = 0.0316$ , the model predicts  $F_{\text{var}}^2 \sim 0.37$  at  $14\text{\AA}$  at superior conjunction and an inferior conjunction continuum that is consistent with zero within the measurement accuracy. These values agree very well with the measurement (Fig. 4.5). However, the slope of the superior conjunction continuum is too steep, which causes  $F_{\text{var}}^2$  to be underestimated below  $14\text{\AA}$ . A larger  $m_{\text{cl}}^{0.5} R_{\text{cl}}^{-1}$  ratio reduces this discrepancy, but requires a non-zero inferior conjunction continuum, which is not observed.

It is important to note that the model is in a very early state. Discrepancies, such as mentioned above, are therefore not surprising. The fact that the model is able to reproduce the qualitative behaviour of the data consistently at both conjunctions shows that varying absorption in an ionised clumpy wind is a viable explanation for the observed variability. I now discuss two noteworthy caveats of the model and how they could affect the variability continuum and line of sight dependence. First is the spherical wind assumption, which disregards the focused stream between star and black hole. The higher density in the focused stream could lead to an increase in variability at superior conjunction. At inferior conjunction, the line of sight passes through the bow shock trailing the black hole, which could disrupt the wind structure and smooth out the absorption variability. A similar effect is expected from interaction with the jet, through which the wind inevitably passes before crossing the inferior conjunction line of sight. Perucho & Bosch-Ramon (2012) showed that wind structures are usually destroyed in interactions with a jet. Second is the use of the canonical velocity law (Eq. 4.3), especially considering that the wind is ionised. The X-ray emission from the black hole changes the ion balance of the wind, and hence the populations of the driving lines. The X-ray luminosity in Cyg X-1 ( $L_x \gtrsim 10^{37} \text{ erg s}^{-1}$ , Miškovičová et al. 2016; Hirsch et al. 2019) is in a regime where it could significantly inhibit the wind acceleration (Krtićka et al. 2018), although the net effect of X-ray photoionising feedback is still uncertain (see Sander et al. 2018, for the insightful example of Vela X-1, another HMXB). The inhibiting effect would be largest towards to black hole where the X-ray irradiation is strongest. It could therefore increase  $F_{\text{var}}^2$  at superior conjunction, as a slower wind must have a higher density if  $\dot{M}$  is fixed. Even without an ionising source, Sander et al. (2017) predict a slower onset of the acceleration, from a model that calculates a self-consistent hydrodynamic stratification of the wind.

#### 4.6.4 Suppressed line variability at inferior conjunction

The line variability predicted by the model is of a similar strength at superior and inferior conjunction (Fig. 4.10, upper panel), yet the observations show line variability only at superior conjunction. This discrepancy is due to the wind moving and becomes apparent from the discussion of the count spectra in Miškovičová et al. (2016). While the superior conjunction spectrum shows absorption, mainly P-Cygni profiles are observed at inferior conjunction. Miškovičová et al. (2016) ascribe this difference to the fact that the absorption at inferior conjunction is highly blue-shifted, because of the line of sight

projection of the wind velocity, separating it from the ubiquitous emission component. Emission lines are suggested to reduce  $F_{\text{var}}^2$  instead of increasing it (Parker et al. 2017b). It is likely that the variability of the absorption and emission components cancels out, given that the absorption component is weak at inferior conjunction and that the resolution of the  $F_{\text{var}}^2$  spectra is lower than that of the count spectra. In addition, narrow spikes appear smaller at lower resolution, because of the averaging effect. The resolution effect also applies at superior conjunction, and plausibly explains why the reported variability is slightly lower than in the model (compare the  $F_{\text{var}}^2$  spikes in Fig. 4.5 and Fig. 4.10, upper panel).

### 4.6.5 Clump mass and radius

The middle panel of Fig. 4.10 shows the behaviour of the model with  $m_{\text{cl}}^{0.5} R_{\text{cl}}^{-1}$ , by taking a low value as a baseline (0.0079; big, light clumps) and showing the ratio of models with higher values to it. As mentioned in Sect. 4.6.2,  $m_{\text{cl}}^{0.5} R_{\text{cl}}^{-1}$  is proportional to  $\delta N_{\text{H}}$  and therefore also to  $F_{\text{var}}$ . For the investigated ratios, the variability spans several orders of magnitude, making  $m_{\text{cl}}^{0.5} R_{\text{cl}}^{-1}$  an influential parameter. For low ratios, the increase in the lines is stronger than in the continuum (light blue curve), but as higher ratios are approached, the increase is reduced (dips in the red and green curves). This relative reduction in line variability is an averaging effect. As  $m_{\text{cl}}^{0.5} R_{\text{cl}}^{-1} \propto \delta N_{\text{H}}$ , the absorption varies over a larger range for higher values of the ratio. Less absorbed spectra are brighter and therefore have a higher weight in the average that is contained in the definition of  $F_{\text{var}}^2$  (see Eq. 2.5 and 2.6). They also show weaker lines, because the line strength responds to the absorbing column. As a consequence, the line variability relative to the continuum is weaker for higher  $\delta N_{\text{H}}$ , resulting in the dips in the model ratio. In addition to this effect, the continuum variability gets more linear, as seen by comparing the upper to the bottom panel in Fig. 4.10, where a high  $m_{\text{cl}}^{0.5} R_{\text{cl}}^{-1}$  ratio was chosen.

An independent approach to obtain information on  $R_{\text{cl}}$  is measuring the timescale of the variability, as small structures cross the line of sight more quickly than large ones, causing the timescale to depend on  $R_{\text{cl}}$ . The analysis of the time binning dependence in Sect. 4.5.3 revealed that the distribution of variability power is shifted towards lower frequencies in the silicon line region compared to the continuum. Such a result is plausibly explained by the response of the line region to the column density changes driving the variability: the line depths vary across a wider range in bigger clumps, which enhances their variability and therefore flattens the frequency trend. This mechanism is likely complemented by the layered ionisation structure of the clumps. Bigger clumps allow for a lower ionisation in their centre (see Sect. 4.2), which also increases the range across which line depth vary. In addition, the larger ionisation range gives rise to more lines. This interpretation is in line with the conclusion from Sect. 4.6.1 that column density changes might drive ionisation variability. As a general conclusion, timescale measurements can, jointly with knowledge about  $m_{\text{cl}}^{0.5} R_{\text{cl}}^{-1}$ , which future versions of the model will likely be able to fit, independently reveal  $m_{\text{cl}}$  and  $R_{\text{cl}}$ .

### 4.6.6 Ionisation

The bottom panel of Fig. 4.10 shows  $F_{\text{var}}^2$  model spectra for  $\log \xi = 2-4$ . Ionisation acts mainly as a scaling factor for both the continuum and line variability. The effect is stronger at lower ionisations (compare the light blue and red, and red and green curves). The to an extent arbitrary choice of  $\log \xi = 3$  is therefore not expected to impact the conclusions reached so far. Note that the  $m_{\text{cl}}^{0.5} R_{\text{cl}}^{-1}$  ratio was chosen to be high in this plot to explicitly show the continuum changes.

The ionisation of the absorber as a function of the distance,  $d$ , from the ionising source is estimated from the definition of the ionisation parameter (Eq. 2.3), by inserting the average density from the stellar wind model by EG20, for  $\beta = 2$ , a mean molecular weight of  $\mu = 1$  u, and the orbital separation from Miller-Jones et al. (2021),  $a = 2.35 R_*$ . The calculation was provided by Ileyk El Mellah. Miškovičová et al. (2016) estimate the distance between absorber and black hole to be  $d \lesssim 0.25 a$ . Figure. 4.11 indicates that the ionisation drops to  $\log \xi \sim 1.8$  at  $0.25 a$  at this distance (dashed line). The ionisation of the absorber can therefore not be constrained to a single value, but is expected to vary over a wide range. Consequentially, observations probe a complex plasma structure, where different ion species dominate in different regions. To illustrate this complexity, Fig. 4.11 shows the abundances of Fe ions from the XSTAR model (see Sect. 4.6.2). Nevertheless, fixing the ionisation to a single value has proven to be a very successful first step, considering the good qualitative agreement of data and model. However, this simple approach inevitably results in an incomplete picture, because varying ionisation is known to contribute to the variability (see Sect. 4.6.1). The layered ionisation structure of the clumps presents further motivation to account for ionisation variability. Examples for the behaviour that might arise from this structure were given in Sect. 4.6.1 and 4.6.5.

How ionisation influences the variability is non-trivial and does depend on multiple factors. For example, variability in absorption lines is not necessarily enhanced. The decisive question is how it correlates with the continuum variability. If line and continuum are anti-correlated, that is to say, the line strength decreases with increasing flux, the total flux change is higher in the line than in the continuum, causing  $F_{\text{var}}^2$  to spike. In the contrary case, the change in the line counteracts that in the continuum, resulting in an  $F_{\text{var}}^2$  dip. For ionisation-driven variability, both cases are possible, even within the same observation. The reason is that a change in ionisation shifts the ion balance, i.e., abundances rise for some ions while they decrease for others, causing opposite responses. Only in specific regimen, the situation can be simpler: for example, in an almost fully ionised environment, the responses of the lines to ionisation changes are more uniform. This special case is thought to apply to ultra-fast outflows of AGN and result in the observed anti-correlation between line strength and flux (see Sect. 3.3). In Cyg X-1, the situation is likely to be more complex, because of the wide range of ionisations the emitting region spans. Adding to that, lines can show different responses in different regions in the source from which the sum is observed, as argued in Sect. 4.6.4 for P-Cygni profiles. This complex behaviour makes the effect of ionisation hard to predict intuitively. A comprehensive model therefore requires radiative transfer modelling, which is out of scope of this thesis. Even though this task is non-trivial, it is worthwhile, because with

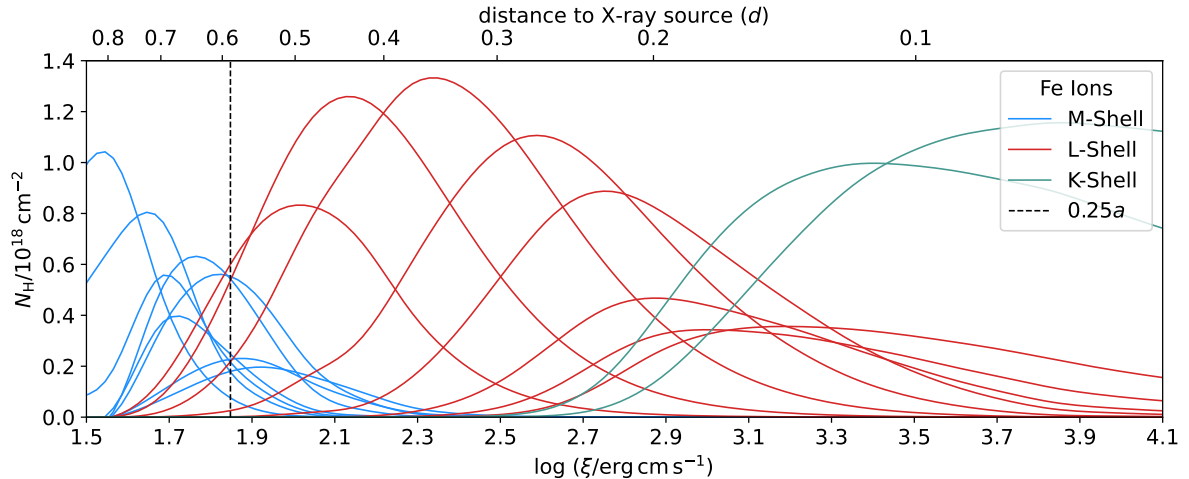


Figure 4.11: Abundances of iron K- (*green*), L- (*red*), and M-shell (*blue*) ions as a function of the ionisation parameter,  $\xi$ , calculated from the XSTAR photoionisation code applied in Sect. 4.6.2 (Härer et al. 2021b, in prep., Fig. 1, adapted). The ionisation is converted to the distance from the X-ray source,  $d$ , as described in Sect. 4.6.6. The dashed line marks the maximal distance of the absorber according to Miškovičová et al. (2016), given in terms of the semi-major axis of the binary system,  $a$ , according to Miller-Jones et al. (2021). The ionisation of the absorber is therefore estimated to be  $\log \xi \gtrsim 1.8$ .

the complexity inherent to the variability behaviour of the lines comes a chance to gain a large amount of information, in particular, on the distribution of material along the line of sight and its size distribution.

## 4.7 Summary

I analyse high resolution excess variance spectra of Cyg X-1 calculated from *Chandra* observations. The analysis takes advantage of the excellent spectral resolution of the *Chandra* HETG. The observations were taken during the low/hard state and cover the superior and inferior conjunction passages (ObsID 3814 and 11044, respectively), which allows for a discussion of the impact of the accretion geometry and wind structure on the excess variance. I match features in the excess variance to their counterparts in the count spectra, by comparing to Hanke et al. (2009), Miškovičová et al. (2016), and Hirsch et al. (2019), who performed detailed spectral analysis on the same data set. I also compare to a selection of significant iron lines in the 2–14Å range. The variability timescale of the most important line regions (silicon and sulphur) is compared to that of the continuum. I demonstrate that systematic variability introduced by the use of *Chandra* gratings data can be dealt with. Specifically, I account for photon loss in detector gaps, effective area differences of the gratings arms, the discreteness of the CCD read-out cycle, and the telescope dither. The fact that the inferior conjunction variability is consistent with zero

and shows no features rules out the existence of further systematic effects that would increase the variability at a measurable level, highlighting the reliability of the results. To complement the data analysis, I compare with a clumpy wind model based on EG20 and an XSTAR table model, incorporating ionisation effects. The main conclusions are summarised in the following.

1. The excess variance is strongly dependent on the orbital phase. While a linearly increasing continuum and spike features are seen at superior conjunction, the inferior conjunction spectrum is consistent with zero and does not show features.
2. The variability is driven by the changing column density of the inhomogeneous stellar wind, which is concluded from the strong orbital phase dependence and the good qualitative agreement of model and data. The model slightly underpredicts the orbital phase dependence and requires a slowly accelerating wind (high  $\beta$ ). The jet or the bow shock of the black hole in the focused wind might disrupt the wind structure, suppressing inferior conjunction variability. It is also possible that superior conjunction variability is underestimated by the model.
3. Variability in absorption lines is enhanced, which gives rise to the spike features in the superior conjunction spectrum, as it can be argued from matching spike and line positions and strengths. This result is especially clear for the silicon line region, as well as for the sulphur line region. In addition, several tentative detections outside these regions are reported. Significant spikes might be absent at inferior conjunction, because the projected wind velocity is higher, causing the count spectrum to be dominated by P-Cygni profiles, whose absorption and emission components cancel out in variability.
4. The variability power in the silicon region is redistributed towards lower frequencies, compared to the nearby continuum. I argue that the line variability might be increased in big clumps, which have higher column densities and reach lower ionisations in their centre.
5. Even though the variability is driven by changes in the column density, the role of ionisation should not be neglected, given the fact that the clumps have a layered ionisation structure. Understanding the impact of ionisation is highly non-trivial. Radiative transfer simulations are required to assess the net effect the counteracting mechanisms have on the observed excess variance spectra.



## 5 Conclusions

This thesis studied winds in two very distinct astronomical settings: the ultra-fast outflow of the high-luminosity low-redshift quasar PDS 456 (Ch. 3) and the strong, clumpy stellar wind in the high-mass X-ray binary Cyg X-1 (Ch. 4). In both cases, excess variance spectroscopy was applied, which allowed for a quantitative analysis of the energy dependence of the variability of these objects.

Ultra-fast outflows are detected via highly blue-shifted absorption lines. In excess variance spectra, these lines appear as spikes of increased variability and tend to be more pronounced than their corresponding count spectral lines. One reason for this advantage is that non-variable components do not contribute to the excess variance, which in addition reduces biases that plague outflow detections. A fit of the excess variance spectrum with a general outflow model is able to reliably gauge the significance of a detection. Chapter 3 was concerned with improving such a model, by extending its applicability to sources which show broadened excess variance spikes. In PDS 456, modelling the broadening as changing outflow velocity and Doppler broadening from the gas dynamics yielded results consistent with the literature. However, disentangling these effects from excess variance spectra alone is difficult, because both show the same behaviour in the excess variance spectrum, i.e., spike broadening, which is not the case in the count spectrum: the changing outflow velocity shifts the line, while the Doppler effect broadens it. Analyses of excess variance and count spectra should therefore go hand in hand. Future work could expand the set of existing models and further improve them, providing better fit quality and parameter constraints.

In the study of the clumpy stellar wind in Cyg X-1 in Ch. 4, the high resolution of the *Chandra* gratings data enabled me to separately study the variability in individual lines of silicon and sulphur ion species. In addition, the variability frequency distribution in the silicon region and the continuum could be compared. These two results demonstrate that excess variance spectroscopy can be used to measure quantities that are key to characterising the wind structure with the modelling ansatz that was presented. With an improved treatment of ionisation, a fit with such a model could in future specifically constrain the mass-size ratio of clumps in the stellar wind,  $m^{0.5}R_{cl}^{-1}$ . Time scale measurements such as those demonstrated could then allow to measure these two parameters independently.

The conclusions from these two projects highlight that excess variance spectroscopy is a versatile tool, which achieves to combine spectral and timing information, making it easy to handle and model. Nevertheless, the amount of signal required to perform an energy and time binning simultaneously presents a major challenge, especially at high resolutions. Microcalorimetry missions like *XRISM* (Tashiro et al. 2018) and *Athena* (with the X-IFU spectrometer, Barret et al. 2018) will provide excellent spectral resolution and sensitivity

## 5 *Conclusions*

at the same time. In addition, the technical difficulties I faced in the Cyg X-1 study come almost exclusively from the use of gratings and will naturally disappear when switching to microcalorimetry. With such instruments available, the many tentative detections of spike features in the Cyg X-1 study can be verified, which makes it possible to use them for wind structure diagnostics as described above. A timescale analysis of individual lines will likely also be possible. The sensitivity will be sufficient to study ultra-fast outflows at resolutions comparable to those archived in the Cyg X-1 study, from which especially soft band detections will profit greatly. In conclusion, excess variance spectroscopy presents a prospect to map out the geometry and structure of winds in unprecedented detail, both in galactic and extragalactic sources.

# Acknowledgments

I would like to thank Jörn Wilms for the opportunity to write this thesis as a continuation of my ESAC project. I really enjoyed being part of the X-ray gang and the Remeis family. Thank you for always quickly setting up a Zoom when there was something to discuss, for the countless things I always learn when talking to you, and for your help with ISIS and so many other small things.

A big “thank you” goes to Michael L. Parker, for the chance to become a part of ESAC for a summer. Even though it was remote, it was a great new experience for me, which included writing my first paper. Thank you for providing the initial impulses for both of the projects, helping me through the XSPEC jungle in the beginning, and creating an incredibly open atmosphere in which I could ask any question without feeling stupid.

I would like to thank Ileyk El Mellah for his contribution to the second project and patience in explaining all the model details to me. A thank you to Victoria Grinberg for all her helpful insights and for watching over the scope of the project.

In addition, I would like to thank Jörn, Michael, Ileyk, and Vici for the insights I gained in our project meetings over the past year. Being part of these discussions really helped me to understand the science involved in the project and, generally, I feel like I learned more in these meetings than I could have in any lecture. I also very much appreciate your support in publishing the results and your detailed feedback.

A thanks also goes to Zsofi Igo, Amy Joyce, and lately Fatima Zaidouni, for your openness, feedback, for making our meetings something fun I looked forward to, and for occasionally taking my mind off things with cat pictures and online Catan. You have been wonderful virtual office mates.

I thank Ralf Ballhausen for providing the XSTAR grid and Gabriele Matzeu and Natalie Hell for digging up old files for the first and second project. I would also like to thank Gabi and everyone else involved from ESAC for the welcoming atmosphere and for your support and suggestions for the first paper.

Another big “thank you” goes to my family and to Stefan Richter, for their feedback, emotional support, and for making sure we never run out of chocolate. Thank you Stefan for being my home office mate for much of the pandemic.

And, last but not least, I thank the Remeis admins for quickly fixing the problems I encountered and generally saving me the pain of installing ISIS and XSPEC on my computer.



# Bibliography

- Alston, W. N., Fabian, A. C., Buisson, D. J. K., et al. 2019, *MNRAS*, 482, 2088
- Arnaud, K., Smith, R., & Siemiginowska, A. 2011, *Handbook of X-ray Astronomy* (Cambridge University Press)
- Arnaud, K. A. 1996, in *Astronomical Society of the Pacific Conference Series*, Vol. 101, *Astronomical Data Analysis Software and Systems V*, ed. G. H. Jacoby & J. Barnes, 17
- Barret, D., Lam Trong, T., den Herder, J.-W., et al. 2018, in *Society of Photo-Optical Instrumentation Engineers (SPIE) Conference Series*, Vol. 10699, *Space Telescopes and Instrumentation 2018: Ultraviolet to Gamma Ray*, ed. J.-W. A. den Herder, S. Nikzad, & K. Nakazawa, 106991G
- Beckmann, V. & Shrader, C. R. 2012, *Active Galactic Nuclei* (WILEY-VCH)
- Boissay-Malaquin, R., Danehkar, A., Marshall, H. L., & Nowak, M. A. 2019, *APJ*, 873, 29
- Boroson, B. & Vrtilik, S. D. 2010, *APJ*, 710, 197
- Bowyer, S., Byram, E. T., Chubb, T. A., & Friedman, H. 1965, *Annales d'Astrophysique*, 28, 791
- Canizares, C. R., Davis, J. E., Dewey, D., et al. 2005, *Publications of the Astronomical Society of the Pacific*, 117, 1144
- Castor, J. I., Abbott, D. C., & Klein, R. I. 1975, *APJ*, 195, 157
- Chartas, G. & Canas, M. H. 2018, *APJ*, 867, 103
- Dauser, T., García, J., & Wilms, J. 2016, *Astronomische Nachrichten*, 337, 362
- Di Matteo, T., Springel, V., & Hernquist, L. 2005, *Nature*, 433, 604
- Edelson, R., Turner, T. J., Pounds, K., et al. 2002, *APJ*, 568, 610
- El Mellah, I., Grinberg, V., Sundqvist, J. O., Driessen, F. A., & Leutenegger, M. A. 2020, *A&A*, 643, A9
- Feng, Y. X. & Cui, W. 2002, *APJ*, 564, 953

## *Bibliography*

- Frank, J., King, A., & Raine, D. J. 2002, *Accretion Power in Astrophysics: Third Edition*, 3rd edn. (Cambridge University Press)
- Fukumura, K., Kazanas, D., Shrader, C., et al. 2018, *APJ Letters*, 864, L27
- Fullerton, A. W., Massa, D. L., & Prinja, R. K. 2006, *APJ*, 637, 1025
- Gallo, L. C. & Fabian, A. C. 2013, *MNRAS*, 434, L66
- García, J., Dauser, T., Lohfink, A., et al. 2014, *APJ*, 782, 76
- Garmire, G. P., Bautz, M. W., Ford, P. G., Nousek, J. A., & Ricker, George R., J. 2003, in *Society of Photo-Optical Instrumentation Engineers (SPIE) Conference Series*, Vol. 4851, *X-Ray and Gamma-Ray Telescopes and Instruments for Astronomy.*, ed. J. E. Truemper & H. D. Tananbaum, 28–44
- Gehrels, N. 1986, *APJ*, 303, 336
- Gies, D. R. & Bolton, C. T. 1982, *APJ*, 260, 240
- Gies, D. R. & Bolton, C. T. 1986, *APJ*, 304, 389
- Gies, D. R., Bolton, C. T., Thomson, J. R., et al. 2003, *APJ*, 583, 424
- Gofford, J., Reeves, J. N., McLaughlin, D. E., et al. 2015, *MNRAS*, 451, 4169
- Gofford, J., Reeves, J. N., Tombesi, F., et al. 2013, *MNRAS*, 430, 60
- Grinberg, V., Hell, N., Pottschmidt, K., et al. 2013, *A&A*, 554, A88
- Grinberg, V., Leutenegger, M. A., Hell, N., et al. 2015, *A&A*, 576, A117
- Grinberg, V., Nowak, M. A., & Hell, N. 2020, *A&A*, 643, A109
- Haardt, F. & Maraschi, L. 1991, *APJ Letters*, 380, L51
- Hagino, K., Odaka, H., Done, C., et al. 2015, *MNRAS*, 446, 663
- Hamann, W.-R., Feldmeier, A., & Oskinova, L. M. 2008, in *Clumping in Hot-Star Winds*
- Hanke, M. 2011, PhD thesis, Dr. Karl Remeis-Sternwarte, Astronomisches Institut der Universität Erlangen-Nürnberg, Sternwartstr. 7, 96049 Bamberg, Germany
- Hanke, M., Wilms, J., Nowak, M. A., et al. 2009, *APJ*, 690, 330
- Härer, L., Parker, M. L., Joyce, A., et al. 2021, *MNRAS*, 500, 4506
- Herrero, A., Kudritzki, R. P., Gabler, R., Vilchez, J. M., & Gabler, A. 1995, *A&A*, 297, 556
- Hirsch, M., Hell, N., Grinberg, V., et al. 2019, *A&A*, 626, A64

- Hogg, J. D. & Reynolds, C. S. 2016, *APJ*, 826, 40
- Hopkins, P. F. & Elvis, M. 2010, *MNRAS*, 401, 7
- Ibragimov, A., Poutanen, J., Gilfanov, M., Zdziarski, A. A., & Shrader, C. R. 2005, *MNRAS*, 362, 1435
- Igo, Z., Parker, M. L., Matzeu, G. A., et al. 2020, *MNRAS*, 493, 1088
- Jansen, F., Lumb, D., Altieri, B., et al. 2001, *A&A*, 365, L1
- Kaastra, J. S., Mewe, R., & Nieuwenhuijzen, H. 1996, in *UV and X-ray Spectroscopy of Astrophysical and Laboratory Plasmas*, ed. K. Yamashita & T. Watanabe, 411–414
- Kallman, T. & Bautista, M. 2001, *APJ Supplement Series*, 133, 221
- King, A. 2003, *APJ Letters*, 596, L27
- King, A. R. & Pounds, K. A. 2003, *MNRAS*, 345, 657
- Krtićka, J., Kubát, J., & Krtićková, I. 2018, *A&A*, 620, A150
- Longair, M. S. 1994, *High energy astrophysics. Vol.2: Stars, the Galaxy and the interstellar medium*, 2nd edn. (Cambridge University Press)
- Lucy, L. B. & Solomon, P. M. 1970, *APJ*, 159, 879
- Martínez-Núñez, S., Kretschmar, P., Bozzo, E., et al. 2017, *Space Science Reviews*, 212, 59
- Matzeu, G. A., Reeves, J. N., Braitto, V., et al. 2017, *MNRAS*, 472, L15
- Matzeu, G. A., Reeves, J. N., Nardini, E., et al. 2016, *MNRAS*, 458, 1311
- McHardy, I. M., Koerding, E., Knigge, C., Uttley, P., & Fender, R. P. 2006, *Nature*, 444, 730
- Miller-Jones, J. C. A., Bahramian, A., Orosz, J. A., et al. 2021, *Science*, 371, 1046
- Miškovičová, I., Hell, N., Hanke, M., et al. 2016, *A&A*, 590, A114
- Mizumoto, M. & Ebisawa, K. 2017, *MNRAS*, 466, 3259
- Montgomery, C., Orchiston, W., & Whittingham, I. 2009, *Journal of Astronomical History and Heritage*, 12, 90
- Nardini, E., Reeves, J. N., Gofford, J., et al. 2015, *Science*, 347, 860
- Nomura, M. & Ohsuga, K. 2017, *MNRAS*, 465, 2873
- Nowak, M. A., Hanke, M., Trowbridge, S. N., et al. 2011, *APJ*, 728, 13

## *Bibliography*

- Orosz, J. A., McClintock, J. E., Aufdenberg, J. P., et al. 2011, *APJ*, 742, 84
- Oskinova, L. M., Feldmeier, A., & Kretschmar, P. 2012, *MNRAS*, 421, 2820
- Owocki, S. P., Castor, J. I., & Rybicki, G. B. 1988, *APJ*, 335, 914
- Owocki, S. P. & Rybicki, G. B. 1984, *APJ*, 284, 337
- Parker, M. L., Alston, W. N., Buisson, D. J. K., et al. 2017a, *MNRAS*, 469, 1553
- Parker, M. L., Alston, W. N., Igo, Z., & Fabian, A. C. 2020, *MNRAS*, 492, 1363
- Parker, M. L., Pinto, C., Fabian, A. C., et al. 2017b, *Nature*, 543, 83
- Parker, M. L., Reeves, J. N., Matzeu, G. A., Buisson, D. J. K., & Fabian, A. C. 2018, *MNRAS*, 474, 108
- Perucho, M. & Bosch-Ramon, V. 2012, *A&A*, 539, A57
- Pinto, C., Alston, W., Parker, M. L., et al. 2018, *MNRAS*, 476, 1021
- Proga, D. & Kallman, T. R. 2004, *APJ*, 616, 688
- Puls, J., Sundqvist, J. O., & Markova, N. 2015, in *New Windows on Massive Stars*, ed. G. Meynet, C. Georgy, J. Groh, & P. Stee, Vol. 307, 25–36
- Puls, J., Vink, J. S., & Najarro, F. 2008, *A&A Review*, 16, 209
- Reeves, J. N., Braitto, V., Chartas, G., et al. 2020, *APJ*, 895, 37
- Reeves, J. N., Braitto, V., Nardini, E., et al. 2016, *APJ*, 824, 20
- Reeves, J. N., Braitto, V., Nardini, E., et al. 2018, *APJ Letters*, 854, L8
- Reeves, J. N., O’Brien, P. T., Braitto, V., et al. 2009, *APJ*, 701, 493
- Reeves, J. N., O’Brien, P. T., Vaughan, S., et al. 2000, *MNRAS*, 312, L17
- Reeves, J. N., O’Brien, P. T., & Ward, M. J. 2003, *The Astrophysical Journal*, 593, L65
- Sander, A. A. C., Fürst, F., Kretschmar, P., et al. 2018, *A&A*, 610, A60
- Sander, A. A. C., Hamann, W. R., Todt, H., Hainich, R., & Shenar, T. 2017, *A&A*, 603, A86
- Seward, F. D. & Charles, P. A. 2010, *Exploring the X-ray Universe*, 2nd edn. (Cambridge University Press)
- Simpson, C., Ward, M., O’Brien, P., & Reeves, J. 1999, *MNRAS*, 303, L23
- Steenbrugge, K. C., Kaastra, J. S., Blustin, A. J., et al. 2003, *A&A*, 408, 921

- Sundqvist, J. O., Björklund, R., Puls, J., & Najarro, F. 2019, *A&A*, 632, A126
- Sundqvist, J. O., Owocki, S. P., & Puls, J. 2012, in *Astronomical Society of the Pacific Conference Series*, Vol. 465, *Proceedings of a Scientific Meeting in Honor of Anthony F. J. Moffat*, ed. L. Drissen, C. Robert, N. St-Louis, & A. F. J. Moffat, 119
- Sundqvist, J. O., Owocki, S. P., & Puls, J. 2018, *A&A*, 611, A17
- Sundqvist, J. O. & Puls, J. 2018, *A&A*, 619, A59
- Tarter, C. B., Tucker, W. H., & Salpeter, E. E. 1969, *APJ*, 156, 943
- Tashiro, M., Maejima, H., Toda, K., et al. 2018, in *Society of Photo-Optical Instrumentation Engineers (SPIE) Conference Series*, Vol. 10699, *Space Telescopes and Instrumentation 2018: Ultraviolet to Gamma Ray*, ed. J.-W. A. den Herder, S. Nikzad, & K. Nakazawa, 1069922
- Tombesi, F., Cappi, M., Reeves, J. N., & Braitto, V. 2012, *MNRAS*, 422, L1
- Tombesi, F., Cappi, M., Reeves, J. N., et al. 2011, *APJ*, 742, 44
- Tombesi, F., Cappi, M., Reeves, J. N., et al. 2010, *A&A*, 521, A57
- Tombesi, F., Tazaki, F., Mushotzky, R. F., et al. 2014, *MNRAS*, 443, 2154
- Torres, C. A. O., Quast, G. R., Coziol, R., et al. 1997, *APJ Letters*, 488, L19
- Uttley, P., Cackett, E. M., Fabian, A. C., Kara, E., & Wilkins, D. R. 2014, *A&A Review*, 22, 72
- van der Klis, M. 1989, in *NATO Advanced Study Institute (ASI) Series C*, Vol. 262, *Timing Neutron Stars*, ed. H. Ögelman & E. P. J. van den Heuvel, 27
- Vaughan, S., Edelson, R., Warwick, R. S., & Uttley, P. 2003, *MNRAS*, 345, 1271
- Vaughan, S. & Uttley, P. 2008, *MNRAS*, 390, 421
- Walborn, N. R. 1973, *APJ Letters*, 179, L123
- Weisskopf, M. C., Tananbaum, H. D., Van Speybroeck, L. P., & O'Dell, S. L. 2000, in *Society of Photo-Optical Instrumentation Engineers (SPIE) Conference Series*, Vol. 4012, *X-Ray Optics, Instruments, and Missions III*, ed. J. E. Truemper & B. Aschenbach, 2–16
- Wilms, J., Nowak, M. A., Pottschmidt, K., Pooley, G. G., & Fritz, S. 2006, *A&A*, 447, 245

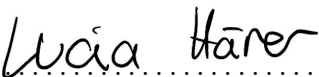


# Eigenständigkeitserklärung

Ich versichere hiermit, die von mir vorgelegte Arbeit selbstständig verfasst zu haben. Alle Stellen, die dem Wortlaut oder dem Sinn nach aus veröffentlichten oder unveröffentlichten Werken anderer entnommen sind, wurden als solche gekennzeichnet. Sämtliche für die Anfertigung der Arbeit genutzten Quellen und Hilfsmittel sind angegeben. Diese Arbeit hat mit gleichem Inhalt bzw. in wesentlichen Teilen noch keiner anderen Prüfungsbehörde vorgelegen.

Teile dieser Arbeit sind aus Härer et al. (2021) und dem Manuskript für Härer et al. (2021b) entnommen. Ich versichere hiermit, dass die übernommenen Textstellen mein eigenes Werk sind. Wo eine Beteiligung der Koautoren an der Forschungsarbeit statt fand, ist diese explizit angegeben. Die Koautoren sind mit der Einreichung der Ergebnisse in Form dieser Masterarbeit einverstanden.

Erlangen, 23. August 2021,

  
.....  
(Lucia Härer)